Mixing Regimes in the Amundsen Basin of the Arctic Ocean

John D. Guthrie

A dissertation

submitted in partial fulfillment of the

requirements for the degree of

Doctor of Philosophy

University of Washington

2016

Reading Committee:

James Morison, Chair

Eric D'Asaro

Susan Hautala

Program Authorized to Offer Degree:

School of Oceanography

University of Washington

Abstract

Mixing Regimes in the Amundsen Basin of the Arctic Ocean

John D. Guthrie

Chair of the Supervisory Committee:
Dr. James Morison
Oceanography

We investigate the role of background mixing in the Arctic Ocean and how it has changed with changing forcing and ice cover. We have examined shear measurements made over more than 30 years to determine the variation in internal wave energy and mixing in different regions of the Arctic Ocean. To improve estimates of thermal diffusivity and heat fluxes in the deep basins of the Arctic Ocean from the base of the mixed layer down to the Atlantic Water layer, we have presented results from three different data sets collected in the central Arctic Ocean as well as leveraging earlier microstructure observations.

Using expendable current profilers in addition to moorings in the Canada Basin, we use shear variance to estimate diapycnal diffusivity in the central Arctic Ocean. We find little change in time despite drastic changes in sea ice extent during the same time period. However, some

spatial variability is present with stronger mixing at depth in the Eurasian Basin and weaker mixing at depth in the Canada Basin. This is attributed to stronger under-ice dissipation in the Canada Basin removing energy from the internal wave field due to the stronger near-surface stratification resulting in that region.

Using temperature microstructure profiles, the regimes of turbulent mixing and double diffusion in the Amundsen Basin during spring have been explored, with double diffusion dominating in 2013 and weak turbulence dominating in 2014. We have provided an updated version of a well-known heat flux parameterization for double diffusion that agrees to within 10% of the observed values. We have also shown that a convecting scaling exponent necessary in relating the Nusselt number and the Rayleigh number needs downward revision. In the absence of a thermohaline staircase, we calculate turbulent diffusivity. Heat fluxes for each mixing regime have been compared and contrasted, and we have proposed an upper bound on the level of turbulent diffusivity necessary to prevent thermohaline staircase formation. The decreased turbulence in 2013 is related to large-scale circulation changes and a shift in the location of the Transpolar Drift.

TABLE OF CONTENTS

LIST OF FIGURES

LIST OF TABLES

ACKNOWLEDGEMENTS

Mere words cannot do justice to the countless hours of academic help and guidance received from the following colleagues: James Morison, Ilker Fer, Eric D'Asaro, Susan Hautala, Allan Devol, James Riley, Roger Andersen, Cecilia Peralta-Ferriz, Jacob Wenegrat, Brian Chinn, Sarah Dewey, Melinda Webster, Hayley Dosser and Andrew Shao.

Going to the Arctic numerous times with James Morison, Andreas Heiberg and Dean Stewart is something I'll always treasure for the following reasons. James: For always choosing the path of most resistance when searching for the perfect floe. Andreas: For knowing every single person North of the Arctic Circle and teaching me the benefit of "going horizontal." Dean: For remaining so cool and collected anytime we had to put the fourth drill string on the 10" auger and teaching me everything there is to know about drilling a hole in sea ice.

Finally, thanks especially to my wife, Margaret and my mother, Linda for putting up with me all these years.

DEDICATION

To Doug, Michael and Stan

Chapter 1. INTRODUCTION

1.1 OVERVIEW

The Arctic Ocean is strikingly different from the other oceans, primarily due to the presence of a perennial sea ice cover blanketing it. Compared to the rest, its deep quiescence has been noted for some time [*Levine et al.*, 1987]. Away from boundaries, the winds and tides are responsible for most of the energy input into the world's ocean, each responsible for around 1 TW of input [*Munk and Wunsch*, 1998]. Dissipation of that energy results in small-scale vertical mixing that has a major effect on stratification and circulation. Below the mixed layer, breaking propagating internal waves, often forced by the winds and tides, are believed to be the primary cause of small-scale mixing in the stratified parts of the water column.

In the Arctic Ocean, the internal wave field is 1-2 orders of magnitude less energetic than canonical mid-latitude open ocean Garrett-Munk levels [*Garrett and Munk,* 1972; *Levine et al.,* 1987]. Weak tidal forcing coupled with the fact that the basin is mostly north of the critical latitude for the M2 semidiurnal tide limits the effectiveness of internal tides well. The presence of an ice cover has long been suspected of limiting internal waves and mixing in the Arctic Ocean. Forces internal to the ice can limit the input of mechanical energy from the atmosphere, although the rough underice surface has also been shown to generate small-scale internal waves [*McPhee and Kantha*, 1989]. Considering the fate of internal waves once they are generated, dissipation in the under-ice boundary layer removes energy from the internal wave field [*Morison et al.*, 1985; *Pinkel,* 2005; *Guthrie et al.,* 2013]. A number of field experiments performed in the 1980s attempted to assess the strength of the internal wave field and vertical mixing in the Arctic Ocean. Results indicated that the Arctic Ocean was quiescent in the deep

basins and energetic over topography [*Levine et al.*, 1987; *Padman and Dillon*, 1993; *D'Asaro and Morison*, 1992]. Since that time, studies of mixing and internal wave energetics in the Arctic have been limited until very recently.

Recent dramatic losses in sea ice extent have reignited interest in the input of mechanical energy into the Arctic Ocean [*Stroeve et al.*, 2007] and possible associated increases in internal wave energy and mixing [*Rainville and Woodgate*, 2009]. While most of the recent sea ice decline can be attributed to increasing solar radiation, recent research efforts have suggested a possible positive feedback loop: increased solar radiation resulting in larger open water areas that increase the availability of wind energy input into the Arctic Ocean [*Martin et al.*, 2015; *Perovich et al.*, 2015]. This could further hasten sea ice loss because of the presence of multiple subsurface temperature maxima that exist throughout the Arctic Ocean, the near-surface temperature maximum, the Pacific Summer Water and the Atlantic Water [*Steele et al.*, 2004; *Jackson et al.*, 2010; Atlantic Water citation]. In fact, the heat contained in the AW layer is enough to melt the entirety of sea ice in the Arctic Ocean within four years if it were able to reach the surface [*Turner*, 2010].

1.2 MIXING IN THE ARCTIC

The "weakly turbulent" environment in the Arctic Ocean has presented complications in the calculation of mixing or diapycnal diffusivity from oceanographic observations. At the same time, modeling studies have shown dramatic changes in circulation and scalar quantities if a typical mid-latitude open ocean value of diffusivity is used [*Zhang and Steele*, 2007]. Also, in the absence of turbulence, non-mechanical mixing regimes like double diffusion are often prevalent. Double diffusion results from the differing molecular diffusivities of heat and salt, e.g. $k_t = 1.4 \times 10^{-7}$ m^{2}s^{-1} and $k_s = 1 \times 10^{-9}$ m^{2}s^{-1}. The stratification of the Arctic makes it susceptible to

the diffusive convective regime of double diffusion, in which T and S both increase with depth. The energy for mixing is provided by the potential energy in the destabilizing T gradient. Double diffusion is considered active in the ocean in areas where thermohaline staircases, sections of the water column consisting of thin, high-gradient interfaces and thick, convecting homogeneous layers, are present. The diffusive convective regime of double diffusion has been observed in the Arctic Ocean for at least 50 years [*Neshyba et al.*, 1971]. In the absence of turbulence, double diffusion is the primary driver of upward vertical heat flux from the heat contained in the Atlantic Water layer. Double diffusive heat fluxes are best computed through the temperature microstructure measurements discussed below but a heat flux parameterization, commonly referred to as the 4/3rd flux law parameterization allows for the calculation of staircase fluxes using coarser CTD data. In this approach fluxes can be inferred through interfacial ΔT and ΔS [*Turner*, 1965; *Kelley*, 1990].

Typically, oceanic mixing is calculated in one of two ways. The more common method is to measure small-scale shear fluctuations, e.g. tiny eddies and overturns, through the use of airfoil probes. This allows for the estimation of ε, the dissipation rate of turbulent kinetic energy. Best current practices can resolve this value down to roughly O(10^{-11}) Wkg^{-1} through the use of loosely tethered free-fall profilers that remove the effect of ship heave, surface waves and cable vibration. Alternatively, fast response thermistors, FP07s, can be used to calculate χ, the dissipation rate of temperature variance, from small-scale temperature gradient fluctuations. Both methods rely on mixing models to estimate diffusivity from the dissipation quantities. Measuring both ε and χ from a single instrument is challenging as shear probes require fast profiling speed, O(1) ms^{-1}, while χ is only resolvable down to dissipative scales through slow profiling. Curve

fitting the temperature gradient spectra based on theoretical Batchelor or Kraichnan spectra is often required to estimate all of the variance in χ [*Kraichnan*, 1965].

Previous Arctic microstructure studies have given priority to the calculation of ε and profiled at higher speeds. This has led to mixed results. In addition to ε being low in the Arctic Ocean compared to mid-latitude open oceans almost everywhere in the water column, it often reaches or falls below the noise level of the instrument at depths greater than 200 m. The earliest measurements were reported in a collection of papers by Padman and Dillon during the Arctic Internal Wave Experiment (AIWEX) in the Canada Basin during the 1980s [*Padman and Dillon*, 1987; *Padman and Dillon* 1988]. They primarily reported on FP07 data and the thermohaline staircase present starting at 200 m depth. However, their shear probe measurements were at or near the noise level of their instrument throughout the period of the experiment with the exception of when the camp drifted over a cyclonic eddy and elevated dissipation values were encountered [*Padman et al.*, 1990]. The same authors recorded energetic dissipation values during the Coordinated Eastern Arctic Experiment (CEAREX) located near the Yermak Plateau, a region of steep topography [*Padman and Dillon*, 1993]. Diffusivities reached energetic values of $O(10^{-4})$ m^2s^{-1}. *D'Asaro and Morison* [1992] attributed the elevated mixing to an evanescent internal diurnal tide trapped in the region of the plateau. These results showed that mixing hot spots are present in the Arctic but most likely located in regions of abrupt topography. *Rippeth et al.* [2015] report similar results along the Siberian continental slope. Given the mixed results of shear microstructure, *Sirevaag and Fer* [2012] and *Rainville and Winsor* [2008] used temperature microstructure to obtain deeper estimates of thermal diffusivity. However, a fast profiling speed was used, which prevented the authors from resolving all of the temperature

gradient variance, and the use of curve fitting to the theoretical Batchelor spectrum was necessary to estimate χ [*Batchelor*, 1959].

Temperature microstructure data have also been used to explore double diffusion in the Arctic as well. *Padman and Dillon* [1987] found that the 4/3rd diffusive convective flux law agreed to within a factor of four with measured interfacial heat fluxes from temperature microstructure. Similarly, *Timmermans et al.* [2008] looked at a single microstructure cast and found "rough" agreement between molecular heat fluxes and the 4/3rd flux law. But these measurements still suffer from fast profiling speeds, as a recent study shows significant underestimation of the magnitude of *dT/dz* across an interface for fast profiling speeds, indicating that the previously reported Arctic double diffusive heat fluxes could be too low [*Sommer et al.,* 2013b].

More work is required in this area to quantify the validity of applying commonly used laboratory flux law parameterizations for heat flux through a thermohaline staircase, especially considering that previous experiments have favored calculating ε over χ which degrades the quality of the FP07 data by profiling faster. The studies by *Padman and Dillon* [1987] and *Timmermans et al.* [2008] also assume the 4/3rd exponent is correct, even though results from standard thermal convection indicate this might not be true [*Kerr, 1996*; *Niemela et al.,* 2001]. *Kelley* [2003] estimates that heat fluxes could be underestimated by 30 to 40% if the correct exponent is closer to 9/7th as predicted by a simple scaling argument in *Kelley* [1990] than the 4/3rd that is commonly used.

The primary goal of this dissertation is to assess and understand Arctic Ocean internal waves and mixing in the context of a changing sea ice cover. We aim to improve on previously derived estimates of heat flux and thermal diffusivity over the Atlantic Water layer in the deep

basins of the Arctic Ocean and extend them to the present. This will be approached in two ways: the first will use a collection of shear profiles collected from the 1980s until the present. Diffusivity can be parameterized through a comparison of observed shear relative to GM levels. Spatial and temporal trends will be examined. The second way will use measurements made in the same geographic region and focus solely on the use of slowly profiled temperature microstructure to estimate thermal diffusivity in the Arctic Ocean through and below the pycnocline without having to rely on curve fits to a theoretical spectrum. Heat fluxes will be calculated for both double diffusion and mechanical mixing depending on which mechanism is dominant and the outside factors controlling which mixing mechanism is dominant will be explored. The validity of different formulations of the 4/3rd laboratory flux law and the scaling exponent will be determined by comparing them to microstructure observations. We will explore the interplay between background mixing and thermohaline staircase formation through a synthesis of four microstructure data sets augmented by XCP profiles. The concentration on χ, rather than ε, will both enhance community knowledge of Arctic mixing and provide a framework for future turbulence studies from a sea ice platform.

1.3 CHAPTER SUMMARIES

1.3.1 *Chapter 2*

Chapter 2 focuses on analysis of recent and historical shear profiles made from eXpendable Current Profilers (XCP) deployed primarily in the Amundsen, Canada and Makarov Basins of the Arctic Ocean. Results from the 1980s from the following field programs: The Arctic Internal

Wave Experiment (AIWEX), The Marginal Ice Zone Experiment (MIZ) and ARKTIS IV/3, will be compared to recent measurements made as part of the North Pole Environmental Observatory (NPEO) and Switchyard airborne hydrography programs from 2007-2012. To augment the XCP data set, we examine velocity data from the Beaufort Gyre Exploration Project moorings in the Canada Basin from 2003-2011. The data will be utilized to compare horizontal velocity spectra to Garrett-Munk internal wave horizontal velocity spectra typical of the mid-latitude oceans. Turbulent diffusivity will be calculated using the finescale parameterization first outlined in *Gregg* [1989], updated by *Polzin* [199?] and concisely summarized in *Kunze et al.* [2006]. Spatial and temporal trends will be examined to qualitatively relate changes in internal wave energy and parameterized diffusivity to reduction in sea ice extent and different stratification.

1.3.2 *Chapter 3*

This chapter focuses on examining the validity of the 4/3rd diffusive convective laboratory flux law in calculating vertical heat fluxes through a thermohaline staircase. During NPEO 2013, vertical profiles of temperature microstructure were made from a drifting ice camp in the Amundsen Basin to focus on characteristics of the thermohaline staircase sometimes present in the region. The instrument package was profiled extremely slowly to quantify the actual temperature gradients across the thin, double diffusive interfaces. The measured interfacial heat fluxes are directly compared to values parameterized through the laboratory flux law, as well as fluxes through the homogeneous, convecting layers through the use of the Osborn-Cox relation [*Osborn and Cox*, 1972]. The applicability of the 4/3rd exponent in the flux law is also examined by using observed heat fluxes in the Nu ~ Ra scaling relationship that the 4/3rd exponent is

derived from. General staircase parameters were compared to previous results from the Arctic Ocean [*Padman and Dillon*, 1987; *Timmermans et al.*, 2008; *Sirevaag and Fer*, 2012].

1.3.3 *Chapter 4*

The work on Chapter 4 focuses on a synthesis of the temperature microstructure measurements made during NPEO 2013 and 2014 as well as previous measurements made by Ilker Fer during NPEO 2007 and 2008. Particular emphasis is placed on the thermohaline staircase present between 120 – 200 m depths during NPEO 2013 since that is the only survey with a thermohaline staircase visible at that depth range. Possible reasons for the existence of that staircase are explored, including density ratio, location, hydrography and background diffusivity. These results are compared to the measurements made during NPEO 2007 and 2008 to search for commonalities between the surveys.

Chapter 2. REVISITING INTERNAL WAVES AND MIXING IN THE ARCTIC OCEAN

 Guthrie, J. D., J. H. Morison, and I. Fer (2013), Revisiting internal waves and mixing in the Arctic Ocean, *J. Geophys. Res. Oceans*, **118**, 3966–3977.

2.1 INTRODUCTION

Internal waves and their associated mixing are critical to the circulation and thermodynamics of the Arctic Ocean. Warm, saline water from the Atlantic enters the Arctic Ocean through Fram Strait where it circulates cyclonically and topographically steered around the basin. In the Nansen and Amundsen basins, this Atlantic Water (AW) is overlain by the cold halocline (CHL), a region of strong stratification, e.g. the buoyancy frequency $N^2 = 10^{-4}$ s^{-1}, which prevents interaction of the ice cover with AW heat by direct surface generated mixing. Only dissipation of internal wave energy or double diffusive phenomena can mix fresh water down and AW heat up toward the mixed layer and the ice. The AW further deepens as it circulates into the Canada Basin, where it is overlain by Pacific-derived water with its own temperature maximum. Here again, the haline stratification dictates that vertical mixing is dependent on internal wave dissipation. Some studies have shown the cold halocline weakening in recent years [*Steele and Boyd*, 1998]. Other studies have shown that even modest heat fluxes, 2 – 7 W m^{-2}, can have significant and irreversible effects on the sea ice concentration [*Maykut and Untersteiner*, 1971; *Polyakov et al.*, 2011]**.**

A modeling study [*Zhang and Steele*, 2007] has shown the sensitivity of the Arctic Ocean to background diapycnal diffusivity. Using the K-profile parameterization (KPP) [*Large et al.*, 1994], *Zhang and Steele* [2007] found the background diffusivity that produced water properties and circulation that agreed best with the Polar Science Center Hydrographic Climatology (PHC) [*Steele et al.*, 2001] of the Arctic Ocean was 10^{-6} m^2 s^{-1}. This is much less than the 10^{-4} m^2 s^{-1} abyssal mixing rate suggested by Walter Munk [*Munk*, 1966; *Munk and Wunsch*, 1998] and the 10^{-5} m^2 s^{-1} value found in most open ocean models [e.g., *Large et al.,* 1994]. *Zhang and Steele* [2007] found that such large values excessively weakened modeled stratification in the Canada

Basin, leading to an erosion of the cold halocline and reversing the cyclonic circulation of the Atlantic Water.

In the deep ocean, stratification limits the penetration of turbulence generated at the surface and mixing comes from the dissipation of internal waves, which propagate freely in the stratified region. This, and in some cases double diffusion, are responsible for the vertical fluxes of heat, salt and momentum in the deep ocean. Consequently, methods have been developed to estimate turbulent dissipation and mixing at micro-scales from measurements of internal wave energy at fine scale with assumptions about the energy cascade through the internal wave spectrum [*Gregg*, 1989]. The *Zhang and Steele* [2007] result is consistent with observations in the 1980s of low internal wave energies made with eXpendable current profilers (XCP) and background mixing (as low as 10^{-6} m^2s^{-1} in the abyssal Arctic Ocean) derived using the *Gregg* [1989] parameterization [*D'Asaro and Morison*, 1992]. A section of temperature microstructure measurements across the Arctic Ocean in 2005 [*Rainville and Winsor*, 2008] also found low levels of mixing consistent with *D'Asaro and Morison* [1992].

A number of explanations have been offered for these low energy levels and mixing rates in the Arctic Ocean. One includes weak tidal forcing and the fact that most of the basin is North of the critical latitude of the M_2 tide, limiting the spread of internal wave energy generated by the interaction of barotropic tides with bathymetry [*Simmons et al.*, 2004; *St. Laurent et al.*, 2002,]. With the exception of the Yermak Plateau, the results of *Simmons et al.* [2004] indicate that, although locally important, internal tide energies in the Arctic Ocean are low compared to typical low-latitude levels. The low internal tide energy levels highlight the importance of atmospheric forcing as the major energy input into the internal wave field of the deep Arctic Ocean. However, the sea ice cover also reduces internal wave energy production [*Levine et al.*, 1985; 1987]. Near-

inertial internal waves, those slightly above the inertial frequency, dominate the energetics of the internal wave field [*Garrett and Munk*, 1972; 1975]. They are forced by wind-generated near-inertial motion at the surface. Wind-driven near-inertial motion of the ice tends to be limited in solid winter ice conditions, but is more common in summer when the ice pack is relatively loose [*McPhee*, 2008; *Plueddemann et al.*, 1998; *Rainville and Woodgate*, 2009]. However, there have been indications of enhanced near inertial motion in winter [*Merrifield and Pinkel*, 1996] and in early winter after freeze up [*Halle and Pinkel*, 2003]

Internal wave energy in the Arctic Ocean is reduced by energy dissipation in the under-ice, surface boundary layer[*Morison et al.*, 1985]. Acoustic Doppler Current Profiler (ADCP) velocity measurements during the 1997-98 SHEBA (Surface Heat Balance of the Arctic Ocean) drift [*Pinkel*, 2005], show that under-ice dissipation is likely a dominant mechanism of internal wave energy loss. Pinkel [2005] postulates that with a reduced ice cover, the near-inertial waves would propagate farther and energy, especially that delivered to the basin boundaries, might be greatly increased [*Rainville and Woodgate*, 2009].

Annual minimum sea ice extent [*Stroeve et al.*, 2007] and thickness [*Kwok et al.*, 2009; *Rothrock et al.*, 2008] have decreased about 40% since the early 1980s when the *D'Asaro and Morison* [1992] observations were made. The declines have continued with ice extent reaching a new minimum in 2012. Given that we think sea ice reduces internal wave energy, we ask whether internal wave energy and mixing in the Arctic basin have increased with the areal reduction and thinning of the ice cover? We address this question by comparing the observations of the 1980s with the same types of measurements made in the last few years.

2.2 METHODS

We compare recent observations of internal waves and mixing with the observations analyzed by *D'Asaro and Morison* [1992] using the *Gregg* [1989] formulation. However, since that time the derivation of mixing from internal wave measurements has been improved to account for the influence of latitude on the internal wave environment [*Gregg et al.*, 2003] and departures of internal wave spectra from the Garrett-Munk [*Garrett and Munk*, 1975] (GM) form [*Polzin et al.*, 1995]. Consequently, we have analyzed both the recent and historical velocity and density profile data following a method [*Kunze et al.*, 2006] that incorporates these improvements to estimate internal wave energy, dissipation, and the deep background mixing coefficient, K. To account for the low energy environment of the Arctic Ocean and the limited depth range of our CTD data, our results are confined to the portion of the water column, 150 to 400 m, containing the cold halocline and extending down past the temperature maximum in the AW. This also allows us to examine the heat flux from the AW to the CHL while avoiding contamination from XCP surface noise and erroneously high diffusivities due to surface mixing and noise-dominated low stratification.

Velocity profiles were WKB stretched by buoyancy frequency [*Leaman and Sanford*, 1975] and tapered using a 10% Tukey window before spectral analysis was performed. Different window choices provided consistent results in terms of power spectral density for the wavenumber ranges analyzed. Individual spectra were then averaged to create one spectrum per survey. No averaging among frequency bands was done. All horizontal velocity spectra were calculated from U and V velocity as $\Phi_U + \Phi_V \cong \Phi_{CW} + \Phi_{CCW}$, where the Φ_U and Φ_V represent U and V velocity spectra, and Φ_{CW} and Φ_{CCW} are the clockwise and counterclockwise rotary spectra [*Gonella*, 1972].

GM fits to the horizontal kinetic energy spectra are calculated as in [*D'Asaro and Morehead*, 1991]. Horizontal velocity spectra were divided by two to turn them into horizontal kinetic energy (HKE) spectra. Fits were then made with the GM "dropped" HKE spectra, retaining cut-off mode number, j_*, and energy, E_o, as free parameters. These are then fit to the data and compared with typical mid-latitude values. In Garrett and Munk [1975], the horizontal kinetic energy spectrum, $E(\boldsymbol{\beta})$ is calculated as

$$E(\beta) = [N_0^2 b^3][\frac{3E_0}{2 j_* \pi}]\frac{(t-1)}{(1+\lambda)^t} \qquad (2.1)$$

where

$$\lambda = \frac{\beta}{j_* \pi f} \qquad (2.2)$$

Standard values used include b = 1300 m, the scale depth of the thermocline, t = -2.5, the spectral slope, N_0 is the reference buoyancy frequency, 3 cycles per hour and $\boldsymbol{\beta}$ is the vertical wavenumber (units are m^{-1})**.** Typical mid-latitude values for the model are j_* = 6 and E_0 = 6.3 x 10^{-5}.

Based on theories of nonlinear wave-wave interactions and downscale energy transfer in the Garrett-Munk model, the fine-scale shear parameterization used to estimate K and ε is based on the most recent iteration from *Kunze et al.* [2006].

$$K = K_0 \frac{\left\langle V_z^2 \right\rangle^2}{\left\langle V_z^2 \right\rangle_{GM}^2} h_1(R_\omega) L(f,N) \quad (2.3)$$

$$h_1(R_\omega) = \frac{3}{2\sqrt{2}} \frac{R_\omega + 1}{R_\omega \sqrt{R_\omega - 1}} \qquad (2.4)$$

$$L(f,N) = \frac{f \cosh^{-1}\left(\frac{N}{f}\right)}{f_{30} \cosh^{-1}\left(\frac{N_0}{f_{30}}\right)} \qquad (2.5)$$

Here, K_0 is 5x10^{-6} m^{2}s^{-1}, the diffusivity calculated from GM internal wave shear. R_ω represents the shear to strain variance ratio, an estimate of the ratio between horizontal kinetic energy to available potential energy, which accounts for departures from GM. $L(f,N)$ represents the latitudinal variation in ε [*Gregg et al.*, 2003], where f_{30} is the Coriolis frequency at 30° latitude, the reference latitude in GM.

Shear and strain for XCP data were calculated using spectral analysis of 64-m overlapping profile segments of 1-m data centered every 10 m. Fine-scale shear variance, $<V_z^2>$, was calculated by multiplying $\Phi_U + \Phi_V$ by $(2\pi k_z)^2$. Shear variance was then integrated out to k_c such that $<V_z^2> = 0.7N^2$ and then taking, $\frac{\langle V_z^2 \rangle^2}{\langle V_z^2 \rangle_{GM}^2} = \left(\frac{0.1}{k_c}\right)^2$ where k_c is the cutoff wavenumber and $0.7N^2$ is the value of $<V_z^2>_{GM}$ integrated out to 0.1 cpm. Experiments with different segment lengths produced consistent results. Strain was calculated as $\xi_z = \frac{N^2 - \overline{N^2}}{\overline{N^2}}$ where $\overline{N^2}$ is estimated by a second-order polynomial fit to the observed N^2 segment. N^2 profiles were calculated from sorted potential density, σ_θ, profiles using the adiabatic leveling method [*Fofonoff*, 1985]. Although sometimes present, thermohaline staircases were not commonly apparent in our profiles. The 2-m resolution of the MMP data and the roughly 1-m resolution of the NPEO CTD data smooth the majority of the staircase features. At depths and locations where they do occur, the staircases can introduce noise in the strain and strain calculation, but at scales smaller than the 10-m scale of the strain calculation. In the XCP data, R_ω was calculated as a

survey average and a single value was applied to the diffusivity profile, while in the MMP data, it was applied to individual profiles due to the longer time record available. Turbulent heat flux is calculated as $F_H = -\rho C_p K \left\langle \frac{dT}{dz} \right\rangle$. Temperature gradient is calculated from survey averaged temperature profiles for each survey. All recent observations are compared with reanalysis of the 1980s data used in *D'Asaro and Morison* [1992] reprocessed identically to the contemporary data.

2.3 DATA

We use XCP and CTD data from the three programs in the 1980s utilized by *D'Asaro and Morison* [1992]: the 1985 Arctic Internal Wave Experiment (AIWEX), the 1983 Marginal Ice Zone Experiment (MIZEX 83) on the *RV Polarbjorn*, the 1987 ARKTIS IV/3 cruise of the *RV Polarstern* (Fig. 2.1). These are compared to data from four modern XCP/CTD surveys since 2007 made as part of the annual North Pole Environmental Observatory (NPEO) airborne hydrographic surveys (http://psc.apl.washington.edu/northpole/CTDs.html).

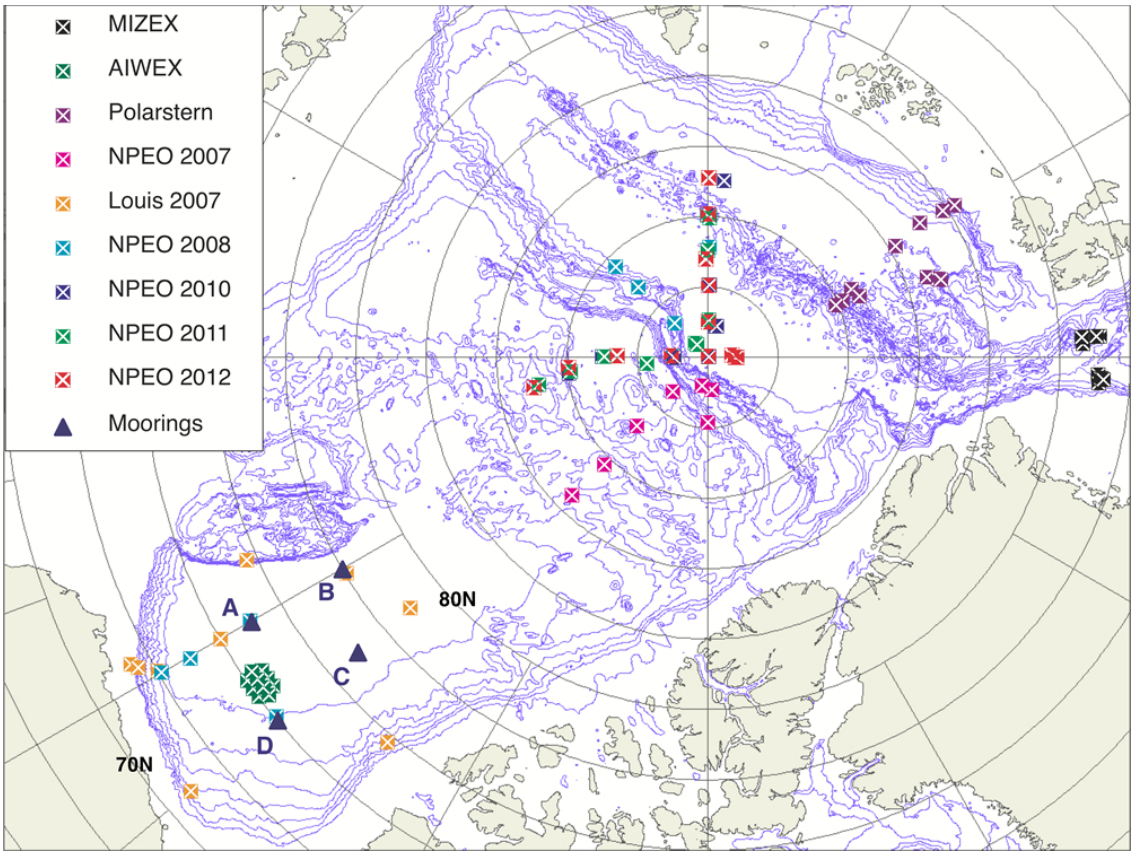

Figure 2.1. Bathymetric chart of the Arctic Ocean detailing the location of all XCP drops and the BGEP moorings.

Over 40 AIWEX profiles are from the Canada Basin (73-74 N, 150 W) between March and April 1985. XCP and CTD data from MIZEX 83 and ARKTIS IV/3 were made mainly between June and July in the Eastern Arctic (North of the Yermak Plateau) but some data from ARKTIS IV/3 are from farther north in the Nansen Basin.

NPEO data are from airborne hydrographic surveys mainly in the central Arctic (85° – 90° N) during April, but several stations were made in the Beaufort Sea in March 2008. Water temperature and salinity profiles at these stations are measured to a depth of 900 m with a Sea-Bird 19 or 19+ CTD. In 2007, NPEO XCP drops were also made from the *CGCC Louis St.*

Laurent during a Beaufort Gyre Exploration Project (BGEP) cruise in the Canada Basin. CTD data from that cruise is provided by the BGEP (http://www.whoi.edu/page.do?pid=66296).

The XCP (http://www.sippican.com/contentmgr/showdetails.php/id/312) measures currents by measuring the voltage induced by the motion of the conducting seawater through the earth's magnetic field. The probe rotates as it falls, and a flux gate compass is used to resolve probe orientation and U and V are determined from the induced voltage signal in phase and in quadrature with the direction signal. As the profiler falls, it transmits analog signals through a fine wire to a radio transmitter and recording system at the surface. Depth is given through the known fall rate of the instrument (~3 m/s). The instrument can record velocity down to a depth of 1800 m. Velocity error is calculated during processing based on the variance about a running harmonic fit to the oscillating voltage and heading signals. Velocity error is determined in processing and varies based on goodness-of-fit but is typically less than 1 cm s^{-1}.

To provide an enhanced view of contemporary conditions in the Beaufort Sea, XCP data are supplemented with time series hydrographic and velocity data from McLane Moored Profilers (MMP) comprising the BGEP moorings. The MMP are each equipped with a Sea-Bird CTD and a 2-D Acoustic Current Meter made by Falmouth Scientific. The MMP data are available at 2-m resolution on the BGEP website (http://www.whoi.edu/page.do?pid=66559). Estimated velocity errors are 1 cm s^{-1} in magnitude and ± 3° in direction.

The MMP data were analyzed similarly to the XCP data, except that the spectral analysis was performed over 128-m (64 data point) windows. $\overline{N^2}$ profiles for the MMP data are calculated as monthly averages. MMP diffusivities are split up into spring and summer averages for each year. Spring averages consist of all profiles made during March and April, while summer averages consist of all profiles made during July and August as these are the months that

most closely coincide with the XCP data. The monthly average MMP diffusivities show minimal seasonal variability and indicate that these periods are representative. All MMP averages cover the same depth range as XCP data (150-400m).

For the internal wave analysis, profiles with spikes or large velocity errors throughout the depth range were discarded. As did *D'Asaro and Morison* [1992], we have not included profiles in eddies in our comparisons because the internal wave induced shear is overshadowed by geostrophic shear due to the eddies, the validity of the internal wave – to – mixing formalism is uncertain within the eddy, and fluxes due to background mixing are possibly overshadowed by the ventilation produced by the larger-scale interaction of eddies with their surroundings. However, microstructure measurements made in a cyclonic eddy during AIWEX do show enhanced dissipation [*Laurie Padman et al.*, 1990]. To check the criticality of excluding eddies in our averages, we have computed the average mixing coefficients for the Beaufort Sea MMP data with and without eddies and find that their inclusion increases average mixing by 10%, well within the confidence limits of the averages. This increase is primarily due to the presence of numerous eddies at mooring A which appears to be a hot spot of eddy activity compared to the other moorings [*Lique et al.,* 2014]. The presence of heightened mixing over shallow bathymetry is well documented [*D'Asaro and Morison*, 1992; *L. Padman and Dillon*, 1991]. However, our focus is the mixing in the deep ocean, and our NPEO XCP data and the MMP data are all in the deep basin, so we do not consider comparisons for example with the Yermak Plateau profiles of MIZEX 83 and *Polarstern* 87. Considering deep-water only, we are left with ~80 profiles. The number of profiles per survey ranges between 5 from the *Louis St. Laurent* 2007 cruise and 40 from AIWEX, with most recent surveys consisting of around 7-10 profiles.

2.4 VALIDATION

The Gregg-Polzin technique approximates the rate of energy dissipation due to wave breaking from the net energy transfer toward smaller scales associated with non-linear interactions in a slowly varying wave field. This is then related to eddy diffusivity using the Osborn model [*Osborn*, 1980]. The relationship (Eq. 2.3), which depends on the finescale shear variance squared and the shear-strain ratio (R_ω), has been validated by several field programs in mid-latitudes [*Lee et al.*, 2006; *Nash et al.*, 2007; *Polzin et al.*, 1995]. Application of the scaling in low stratification regions may be dominated by noise resulting in spuriously large diffusivities [*Kunze et al.*, 2006]. This is not a concern for our results, which are obtained between 150-400 m in the stratified part of the water column.

Our method of estimating mixing is tested with a comparison among K parameterized using the original *Gregg* [1989] (G89) and the *Kunze et al.* [2006] (K06) approaches applied to XCP and CTD profiles and calculated from microstructure measurements using an MSS90L, a loosely tethered free-fall profiler made by ISW Wassermesstechnik in Germany. The MSS90L diffusivity profiles are obtained, down to 500 m, from dissipation measurements made with two airfoil shear probes, using the Osborn model (Osborn, 1980)**.** Application of the Osborn model is identical in the finescale parameterization and the microstructure measurements, each using a mixing efficiency of 0.17. The processing of the microstructure data follows that of *Fer* [2006; 2009]. The noise level in dissipation rate measurements is 5×10^{-10} W kg^{-1}.

Joint microstructure and XCP measurements are available in the marginal ice zone, from a cruise over the Yermak Plateau in 2007, and in the pack ice during the drifts of the NPEO base camp near the North Pole in 2007 and 2008. The profile pairs collected in Yermak 2007 and NPEO 2008 are within 1 hour and 1 km separation. Those collected in NPEO 2007 however are

separated by 0.5 to 2.7 km and 2 to 10 hours. In total, high quality data from 31 profile pairs were recovered (4 from NPEO 2007, 18 from Yermak 2007, and 9 from NPEO 2008). Average profiles from the three separate surveys are shown in Figure 2.2. In applying K06, a constant shear-strain ratio of $R_\omega = 11$ is applied following the observations of *Fer et al.* [2010] to the Yermak Plateau survey, while the values listed in Table 2.1 are applied to NPEO 2007 and NPEO 2008. Both parameterizations show good agreement with the microstructure-based estimates, both in terms of amplitudes and vertical variability, and certainly well within the known limitations of both K06 and G89. K06 yields slightly lower diffusivities than the G89 approach used by *D'Asaro and Morison* [1992]. The discrepancy between MSS and XCP-derived results for NPEO 2007 may be due to the large time (up to 10 h) and spatial (up to 3 km) separations between XCP-MSS pairs. The NPEO 2007 XCP results are calculated from only 4 profiles, a small sample size that may not be sufficient enough to produce a representative average profile. Furthermore, this difference highlights the role of intermittent mixing processes and strengthens our approach of multi-station averaging to be able to draw conclusions on temporal and spatial trends.

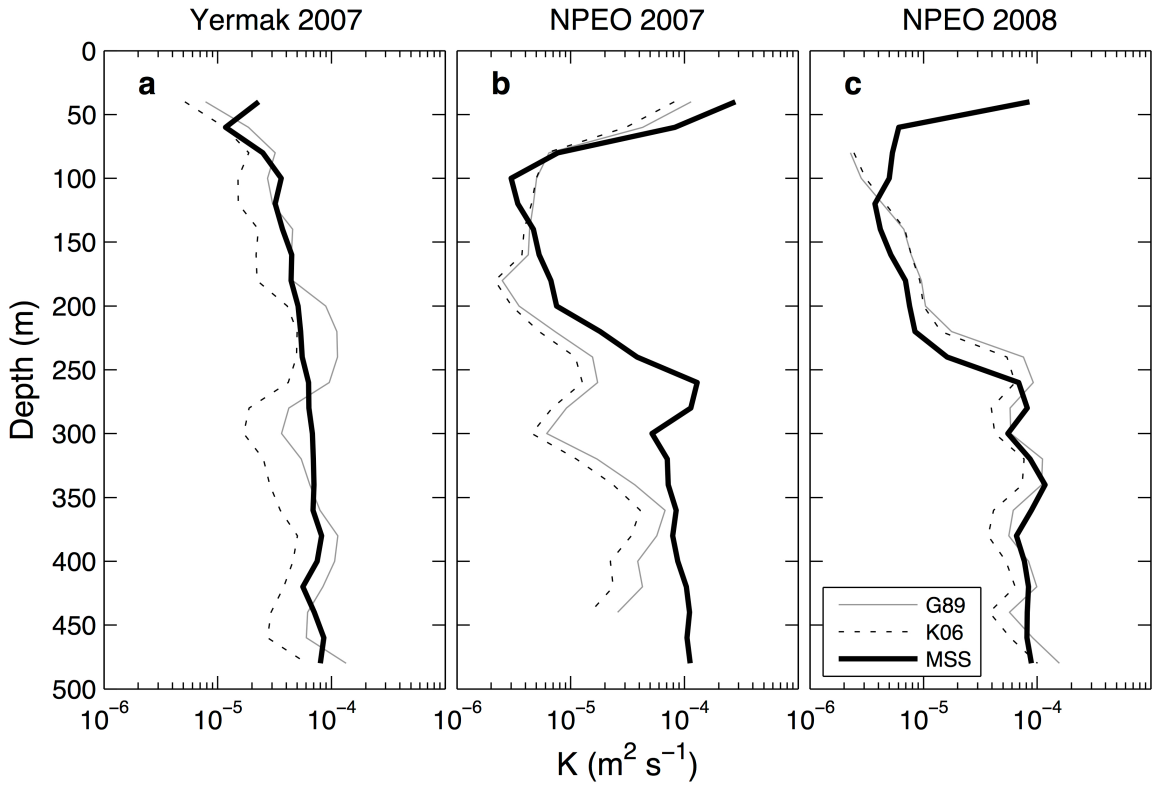

Figure 2.2. Direct comparison between K parameterized from XCP drops using the *Gregg* [1989] (G89) and *Kunze et al*. [2006] (K06) parameterizations with K estimated from microstructure observations for three surveys.

2.5. RESULTS

Comparison of vertical wavenumber power spectra of horizontal velocity from the 1980s and from NPEO show ranges of up to an order of magnitude between surveys (Fig. 2.3). Values of E_0 and j_*, along with other calculated quantities, for all surveys are shown in Table 2.1. All surveys show the presence of more vertical modes than the open ocean with all values of the cut-off mode number, j_*, greater than 25 versus j_*=6 for GM. This is consistent with results from AIWEX [*D'Asaro and Morehead,* 1991]. The increased number of vertical modes results in flatter spectra typical mid-latitude spectra. The spectral energy level, E_0, varies between surveys

with values ranging between 0.05 and 0.2 of GM. Two of the recent NPEO surveys have the highest value of E_0, roughly a fifth of GM and comparable to MIZEX 83 and *Polarstern* 87. Surveys from the Canada Basin show low E_0, consistent with previous results [*Levine et al.*, 1987, *D'Asaro and Morehead,* 1991]. This is highlighted by the AIWEX spectrum and the XCPs dropped from the *Louis St. Laurent* in 2007 with values of 0.05 and 0.11 of GM respectively. However, recent central Arctic Ocean surveys, NPEO 2010 and NPEO 2012, show similarly low energy levels, .057 and .065 of GM respectively.

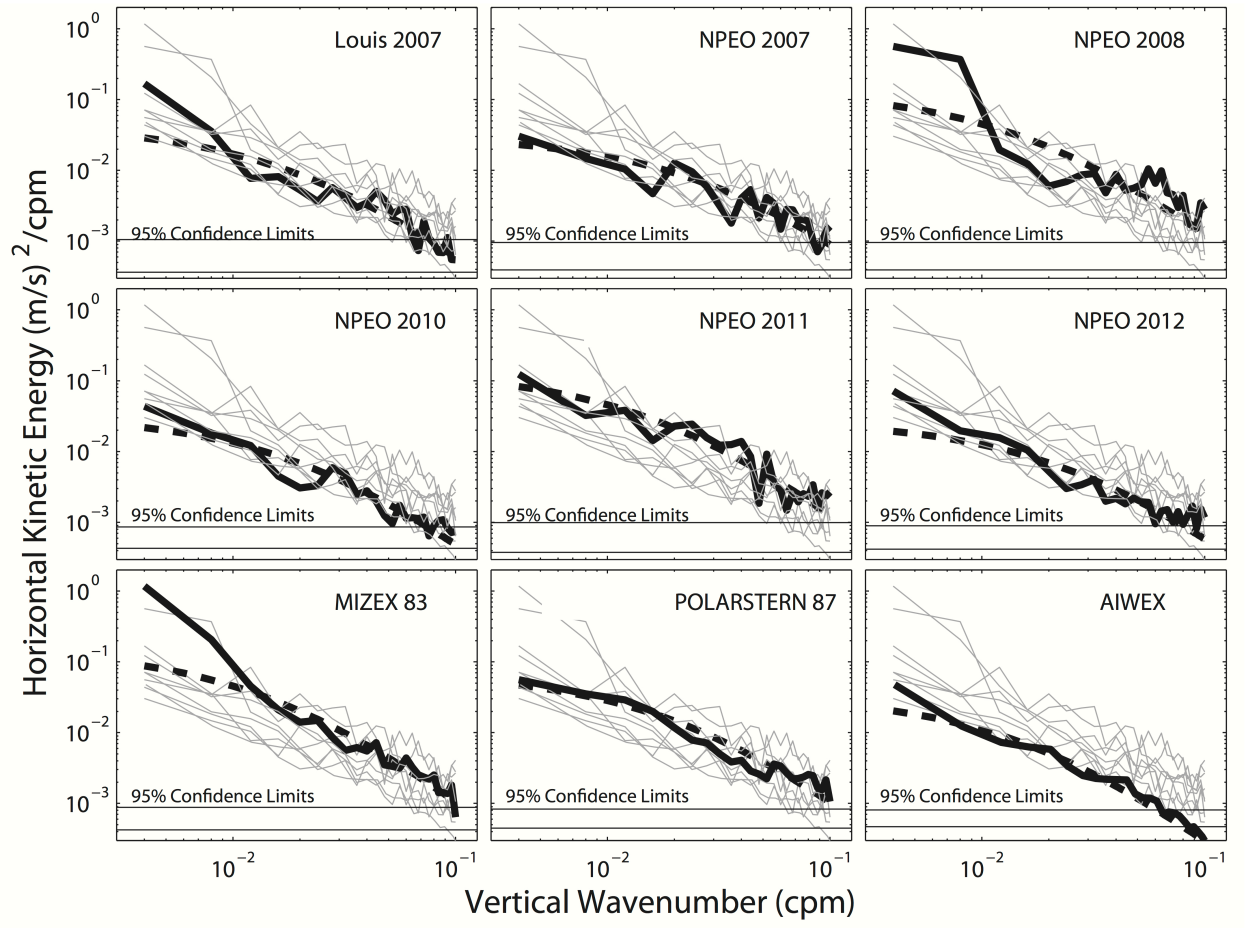

Figure 2.3. Survey averaged WKB scaled vertical wavenumber spectra of Horizontal Kinetic Energy. Survey listed in the title is given in solid black, a GM fit is given in dashed black. The light grey lines are the other surveys.

Rotary spectral analysis was also performed [*Gonella*, 1972, *Leaman and Sanford,* 1975] to calculate survey-averaged clockwise (CW) versus counter-clockwise (CCW) variance ratio (see Table 1). This can be interpreted as a ratio of downward propagating to upward propagating energy. Values for all surveys range between 1 and 2, indicating a slight net downward internal wave energy propagation. The *Louis* 2007 cruise has the highest ratio, 1.8. This was a cruise during the summer of a record minimum sea ice extent,. It makes sense in terms of enhanced internal wave generation being under reduced ice cover that this value is higher than the other surveys, which were either made during springtime or in the summertime in the presence of more sea ice. Comparison with the historical data (MIZEX 83, *Polarstern* 87, AIWEX) suggests a very small increase in the amount of downward propagating energy present between 150-400 m but the increase is not statistically significant and a clear temporal trend is hard to justify.

Table 2.1. Calculated Properties

Survey	**Date**	**# of Profiles**	j^*/j^*_{GM}	$E0/E0_{GM}$	K	R_ω	**CW/ CCW**	Max F_H
Louis 2007	08/2007	5	4.7	.11	$5.5*10^{-6}$	4	1.83	.33
NPEO 2007	04/2007	7	11	.07	$1.1*10^{-5}$	7	1.35	.22
NPEO 2008	04/2008	7	6	.25	$9.5*10^{-6}$	6	1.39	.3
NPEO 2010	04/2010	13	7.7	.06	$5.7*10^{-6}$	8	1.02	.15
NPEO 2011	04/2011	6	6	.16	$2.5*10^{-5}$	11	1.08	1.2
NPEO 2012	04/2012	10	8	.07	$5.4*10^{-6}$	10	1.21	.19
MIZEX 83	06-07/1983	11	5	.19	$1.2*10^{-5}$	11	1.03	.67
PSTERN 87	07-08/1987	20	6.3	.11	$2*10^{-5}$	11	.99	1.58
AIWEX	03-04/1987	40	7.3	.05	$1.1*10^{-6}$	12		.09

Survey-averaged diffusivity profiles are shown in Figure 2.4. Diffusivity is typically $O[10^{-6}\ m^2s^{-1}]$ in the upper (cold halocline) part of the profile consistent with estimates from *D'Asaro and Morison* [1992] and recent observations [*Fer*, 2009; *Rainville and Winsor*, 2008].

MIZEX 83, *Polarstern* 87 and NPEO 2011 have higher K, while the two Beaufort Sea surveys (AIWEX and *Louis* 2007) are the lowest. Below the CHL, diffusivity increases to O[10^{-5} m^2s^{-1}] and even approaches O[10^{-4} m^2s^{-1}] in the case of NPEO 2011. While the calculation of K_ρ is dependent on R_ω, it is not strongly so. An increase of R_ω from 3 (GM value) to 6 or 12 leads to a factor of 1.8 or 2.9 reduction in K_ρ.

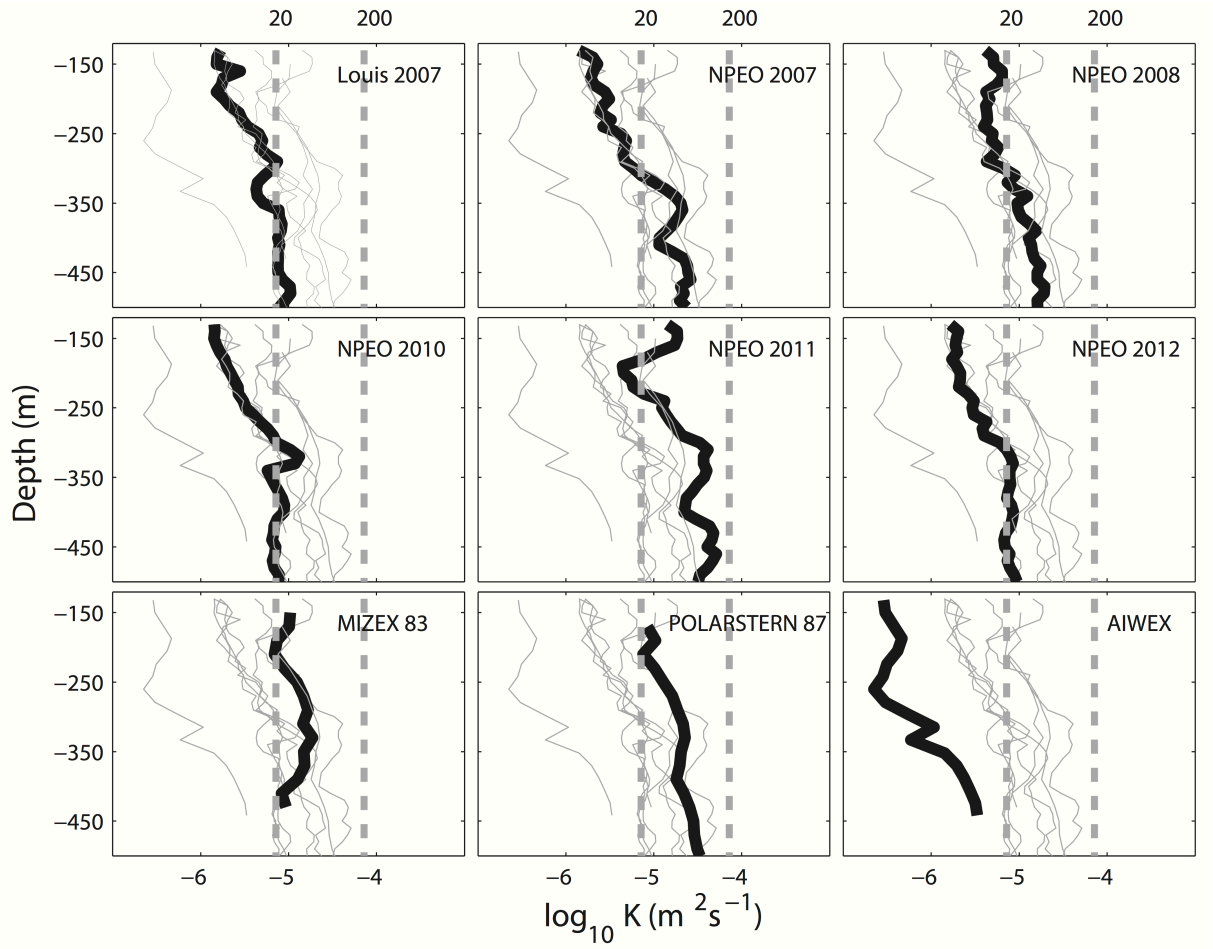

Figure 2.4. Survey-averaged diffusivity. Survey listed in the legend. Light grey lines are the other surveys. The dashed gray lines represent values of $\frac{\varepsilon}{\nu N^2} = 20$ and 200 respectively.

Buoyancy Reynolds number or Turbulent Activity Index, $\frac{\varepsilon}{\nu N^2}$, analysis supports the low diffusivities inferred from the K06 parameterization. It is a predictor of the efficiency of

turbulence in overcoming stratification and producing mixing with $\frac{\varepsilon}{\nu N^2} \approx 20$ being the minimum value for which turbulent mixing becomes important. Below this value, the turbulence is not strong enough to induce a buoyancy flux [*Gregg and Sanford*, 1988; *Stillinger et al.*, 1983] Across the CHL, this value is below 20 for all surveys except NPEO 2011, *Polarstern* 87 and MIZEX 83 (See Fig. 2.4). However for most surveys, this value exceeds 20 close to the AW temperature maximum (~250 m) where stratification weakens. For NPEO 2010, NPEO 2012 and *Louis* 2007, turbulence might be unimportant at all depth ranges analyzed.

Survey averaged mean K_ρ values between 150-400 m for all XCP data sets (Fig. 2.5) show no clear temporal trend. Excluding AIWEX, depth averaged (150-400 m) diffusivities range from 5 x 10^{-6} (*Louis* 2007) to 2 x 10^{-5} m^2s^{-1} (NPEO 2011). Calculating depth averages solely across the most stratified part of the cold halocline (e.g., 150-250 m) yields diffusivities of O[10^{-6} m^2s^{-1}], lower than most oceanic shear microstructure measurements, O[10^{-5} m^2s^{-1}], but of the same order of magnitude as recent microstructure measurements in the Arctic [*Fer*, 2009; *Rainville and Winsor*, 2008].

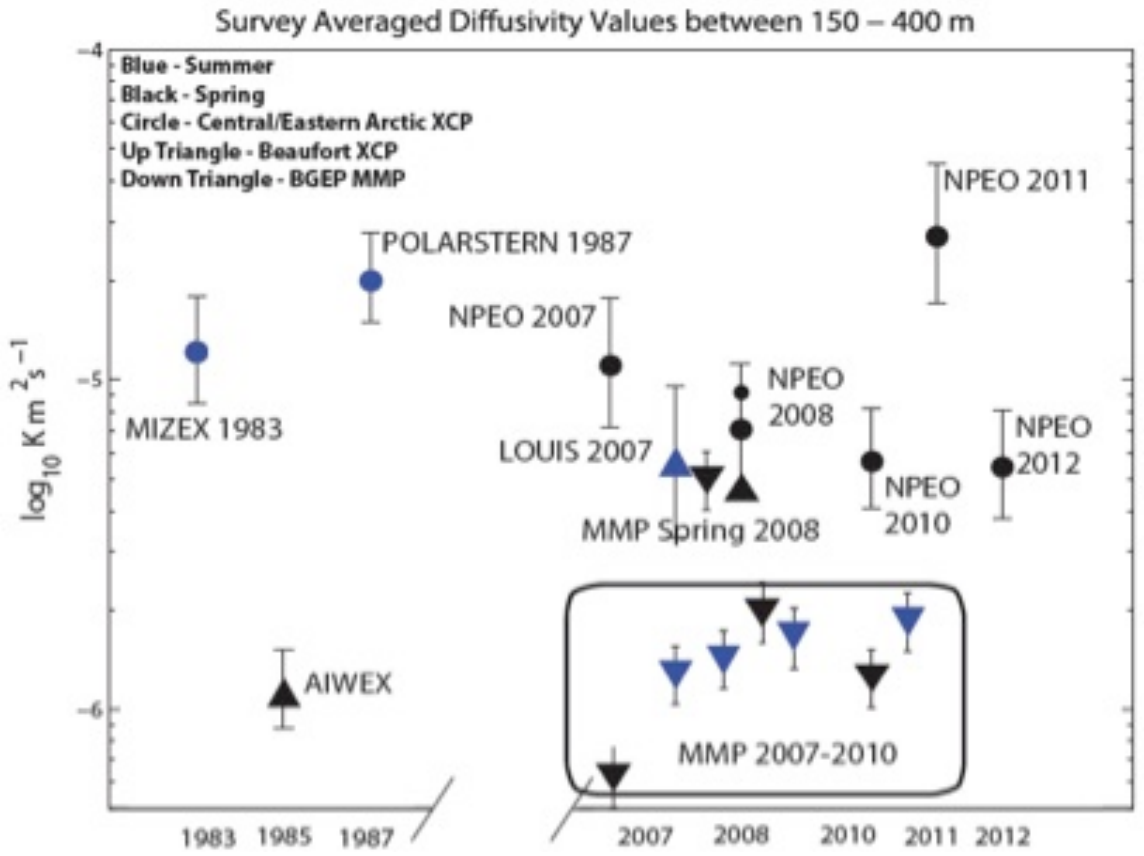

Figure 2.5. Survey-averaged mean diffusivity between 150-400 m. Black icons represent springtime surveys (March/April). Blue icons represent summertime surveys (June/July/August). Circles are Central/Eastern Arctic XCP data. Upward triangles are Beaufort Sea XCP data. Downward triangles are Beaufort Sea MMP data.

Perhaps the most surprising facet of the XCP results is the low diffusivity characterizing the Beaufort Sea region. In the early period, the average AIWEX diffusivity is an order of magnitude lower than MIZEX 83 and *Polarstern* 87. In the recent data, *Louis* 2007 and the Beaufort Sea NPEO 2008 profiles yielded diffusivities higher than AIWEX, but they are among the lowest from the recent surveys. *Louis* 2007 and NPEO 2008 (Beaufort) consisted of few profiles resulting in wide confidence limits. The diffusivities from the MMP profiles from 2007 to 2010 are directly comparable. Except for spring 2008, the MMP-derived diffusivities average 1.5×10^{-6} m^2s^{-1} compared to 1.1×10^{-6} m^2s^{-1} for AIWEX. Only the spring 2008 gives an MMP-

derived diffusivity of 5 x 10^{-6} m^2s^{-1} in agreement with the NPEO 2008 (Beaufort) values. To test whether these results were sensitive to our choice of sampling periods (spring and late summer), we also computed month-by-month averages of diffusivities for the 2007-2010 MMP time series. The month-by-month composite diffusivities range only from 1.4 x 10^{-6} m^2s^{-1} in April to 3 x 10^{-6} m^2s^{-1} in January, the April value well within the error bars for the springtime AIWEX diffusivity.

We have also calculated turbulent heat fluxes using the diffusivities derived here (Fig. 2.6). The most energetic surveys (NPEO 2011, MIZEX 83, *Polarstern* 87) display F_H ranging between -2 and 2 Wm^{-2}. Most of the NPEO 2011 profile is similar to the other NPEO surveys except for large fluxes near 120 m that results from higher diffusivity at that depth. The *Polarstern* 87 and MIZEX 83 heat fluxes are consistent with those found by *D'Asaro and Morison* [1992]. These are larger than the heat fluxes measured during the other surveys due to the proximity of ARKTIS IV/3 and MIZEX 83 to the warm Atlantic Water inflow to the Arctic Ocean and comparable to the large heat fluxes observed in the boundary current on the East Siberian continental slope [*Lenn et al.*, 2009]. The values of F_H from the NPEO data (except 2011), AIWEX and *Louis* 2007 vary between -0.3 and 0.3 Wm^{-2}, similar to double-diffusive estimates from both ITP [*Timmermans et al.*, 2008] and microstructure [*Sirevaag and Fer*, 2012] measurements. The NPEO surveys suggest that temperature gradient is still the controlling factor in this calculation as the diffusivities differed significantly in some areas, yet outside the depths of elevated diffusivities found in the NPEO 2011 profile, the heat flux profiles are remarkably consistent from year to year.

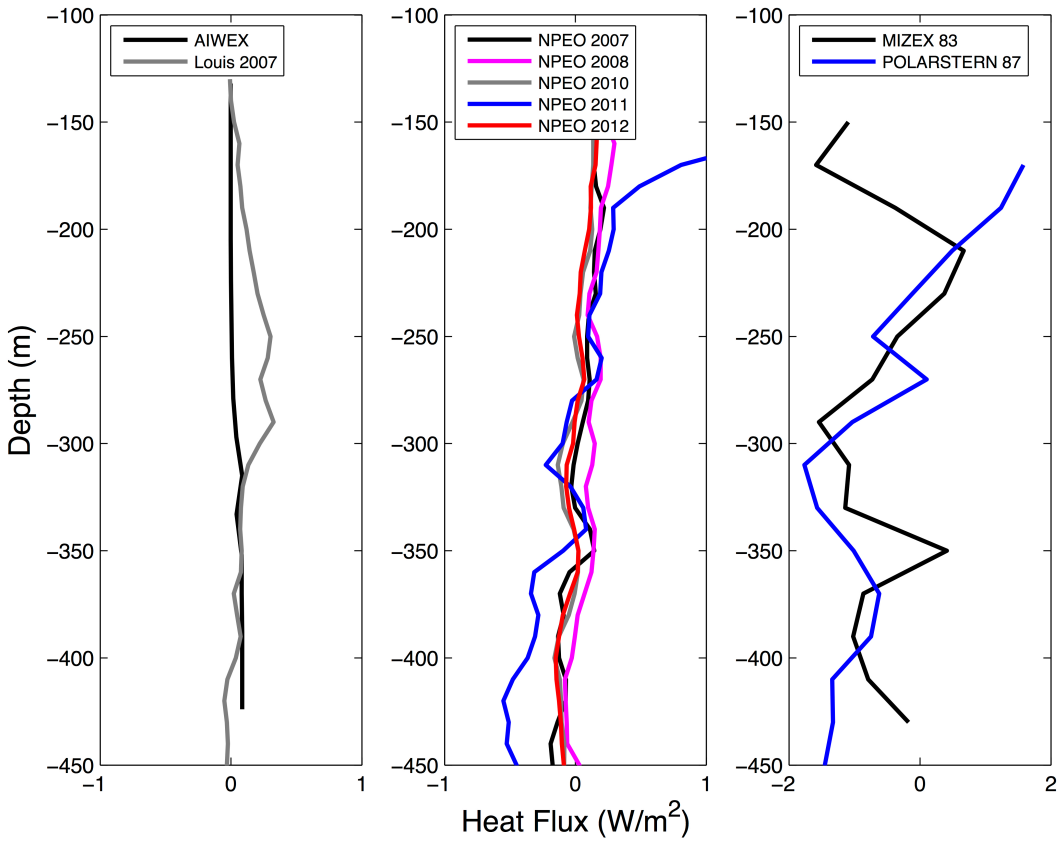

Figure 2.6. Shows values of turbulent heat flux calculated for all XCP surveys.

2.6. DISCUSSION

In the Arctic Ocean, internal wave energy varies significantly, but all surveys show less energy than typical mid-latitude GM values and much broader bandwidth. Diffusivities in the Beaufort Sea, measured recently and decades in the past show levels at the bottom of the range. Parameterized mixing values across the cold halocline are lower, O[10^{-6} m^2s^{-1}] than typical open ocean values measured by microstructure O[10^{-5} m^2s^{-1}]. However, most surveys begin to increase towards this value at around 300 m depth. Values of parameterized ε remain low (below the noise level of most previous microstructure measurements) across all depth ranges analyzed and the increasing diffusivities with depth result from the decreasing stratification.

There is also a question of whether the latitudinal dependence term, *L(f,N)* (Eq. 2.3) is applicable in this study, but our diffusivity estimates are not low because of it. This correction is an empirical result but has only been verified in mid-latitudes [*Gregg et al.* 2003]. The large f (1.45×10^{-4} s^{-1}) found at high latitudes could lead to an overestimation of K_ρ, as *L(f,N)* can effectively double the diffusivity at high latitudes in the presence of strong stratification, such as across the CHL. Our inclusion of this correction should be conservative with respect to inferring that diffusivities are low.

Our results suggest that the amount of open water and strength of the ice are not the dominant factors responsible for determining internal wave energy and mixing. The more recent estimates of diffusivity in the Beaufort Sea (*Louis* 2007 and 3 profiles from NPEO 2008) are somewhat higher than the values from AIWEX. Values from summertime when ice is thin and free to move (*Louis* 2007) and springtime when ice is thicker and more compact (NPEO 2008) are similar. Analysis of the MMP data from 2007-2010 reveals that although the spring of 2008 shows the highest diffusivities, typical diffusivities in spring are either less than or of the same magnitude as those in summer (see inset Fig. 2.5). This whole period comes immediately after the 2007 Arctic sea ice minimum and significant increases in the freshwater content of the Beaufort Sea [*McPhee et al.*, 2009; *Morison et al.*, 2012; *Proshutinsky et al.*, 2009].

In the presence of an ice cover, internal wave energy and background mixing may be most sensitive to upper ocean stratification. Internal wave energies and the consequent deep background mixing are about a factor of 5 lower in the Beaufort Sea than in the Central Arctic Ocean. These regions should have similar internal wave forcing; indeed we might expect stronger forcing in the Beaufort Sea region where record reductions in the sea ice have occurred. For the Beaufort Sea, the effect of stronger near-surface stratification (Fig. 2.7a) on internal

wave dissipation in the boundary layer immediately under sea presents a possible explanation for persistently low internal wave energies and mixing.

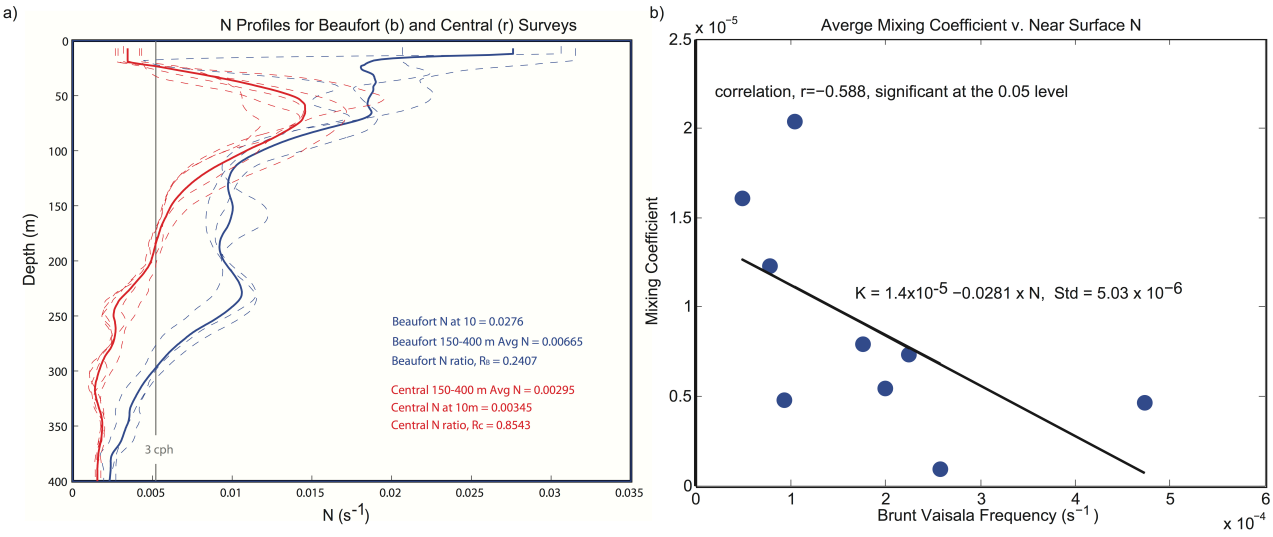

Figure 2.7. Comparisons of XCP survey stratification and mixing coefficients (a) Brunt-Vaisala frequency, *N*, profiles versus depth for XCP for Beaufort and Central Arctic Ocean surveys and average regional *N* profiles (thick lines). (b) XCP Survey averaged mixing coefficients plotted versus survey averaged *N* in the upper part of the ocean.

Internal wave energy is dissipated in oscillating boundary layers under sea ice and this process limits steady state internal wave energy [*Morison et al.*, 1985; *Pinkel*, 2005]. As illustrated in the schematic of Fig. 2.8 (a) and 2.8 (b), the surface boundary condition for internal wave horizontal velocity is free in open water, but under ice a no-slip boundary condition applies. The influence of the no-slip boundary condition imposed by the ice on internal wave velocities increases with degree of stratification below the mixed layer. Considering the normal modes of internal waves, the velocity corresponding to each mode just outside the under-ice boundary layer (e.g. at the base of the mixed layer) is proportional to the vertical derivative of the corresponding displacement mode shape. This is illustrated in crude fashion by comparing the 1st mode behavior in a two-layer ocean with deep (Fig. 2.8(b)) and shallow (Fig. 2.8(c))

upper layers. If near surface stratification is increased, due either to freshening or shoaling of the mixed layer, the horizontal velocity associated with each mode is increased relative to the velocity at greater depth. For a given internal wave energy at depth, an increase in near-surface stratification will result in greater internal wave horizontal velocity approaching the surface and greater dissipation in the turbulent underice boundary layer. This being the case, we should expect to see perpetually lower internal wave energy in the Beaufort Sea where near-surface stratification is greater than in the Nansen and Amundsen basins (Fig. 2.7a). Other things being equal, we might also expect internal wave energy and mixing to decrease after a major surface freshening as occurred in 2007-2008. Dominance of underice boundary layer dissipation in Arctic internal wave dynamics may account for the negative correlation, r = -0.59 significant at the 0.05 level, between XCP survey average mixing and near-surface stratification (Fig. 2.7b). The MMP record from Summer 2007 indicates that the diffusivity estimated by the *Louis* 2007 XCPs is anomalously high. Removing the mean diffusivity value of the *Louis* 2007 data strengthens the negative correlation of diffusivity with stratification to r = -0.71.

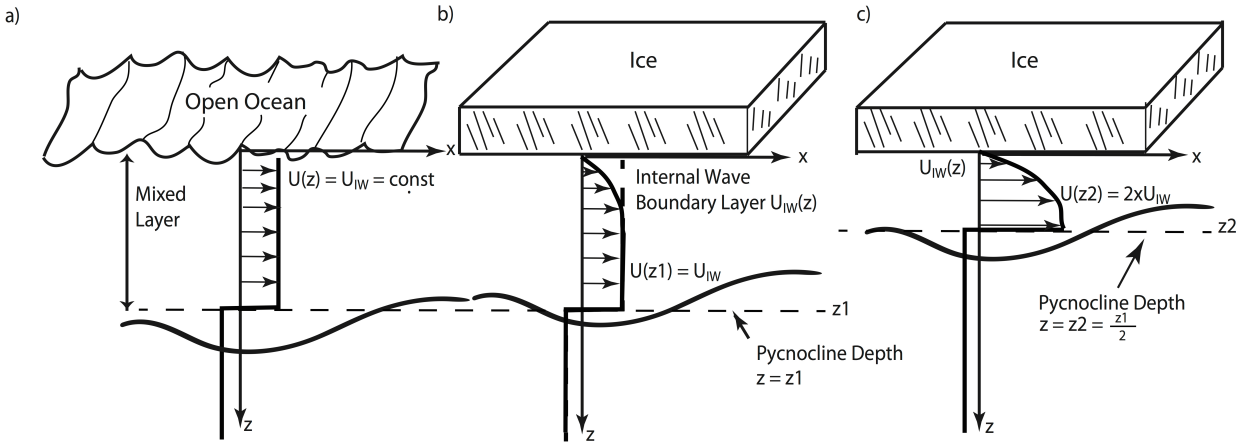

Figure 2.8. Schematic (adapted from *Morison et al.* [1985]) illustrating the difference in internal wave boundary conditions between (a) the open ocean (b) an ice covered ocean (c) an ice covered ocean with increased near-surface stratification idealized as a reduction in upper layer depth and consequent increase in the first internal wave mode upper layer velocity.

We explore the influence of stratification and boundary layer dissipation on internal wave energy by extrapolating on the results of *Morison et al.* [1985]. To estimate the dissipation of internal wave energy in the boundary layer imposed by the no-slip condition at the ice-water interface, *Morison et al.* [1985] drove an oscillating boundary layer model [*Long*, 1981] with a discrete spectrum of horizontal velocities representing free-stream internal wave horizontal velocities near the surface. These were derived from observations of vertical displacement at 50 to 150 m depth at the Fram III ice camp north of the Yermak Plateau in 1981 [*Levine et al.*, 1985]. The [*Desaubies*, 1976] formulation of the GM model was used to parameterize the displacement and velocity spectra at Fram III using N equal to 3 cph (0.0052 s^{-1}) and a magnitude about one sixth of GM. The interaction of the internal waves with the boundary layer was linearized by assuming that the turbulence level was dominated by the RMS velocity of the ice, U_{ice} = 7 cm s^{-1}, with the consequence that the boundary layer dissipation of internal wave energy, Q_{bl}, is proportional $U_{ice}U_w^2$. where U_w^2 is the internal wave energy just outside the oscillating underice boundary layer. Approximating the total internal wave energy with a first order differential equation, they found that the corresponding time scale for internal wave dissipation is τ_{bl} = 32 days, one third that for open ocean conditions, τ_{ow} = 100 days [*Olbers*, 1983] without an internal wave boundary layer. Assuming equal forcing, the ratio of internal wave energy in the under-ice environment to the open ocean internal wave energy is $E_{IC}/E_{OW} = \tau_{BL}(\tau_{BL} + \tau_{OW})^{-1}$ = 0.24 indicating a factor of four reduction in energy relative to open ocean conditions due solely to boundary layer dissipation.

The impact of near surface stratification on the rate of internal dissipation in the underice boundary layer is a fundamental outcome of WKB scaling [*Leaman and Sanford*, 1975].

Morison et al. [1985] used internal wave measurements near the surface to drive their model and thus did not consider the variation of internal wave horizontal velocity with stratification. As long as stratification near the surface is not too different from that at depth (e.g., Central Arctic Ocean N profile in Fig. 2.7a), variations in N are probably not critical to the boundary layer dissipation calculation, but in cases where N is dramatically higher in the upper part of the halocline, as in the Beaufort Sea (Fig. 2.7a), WKB scaling, $U_w \sim N^{1/2}$, [*Leaman and Sanford*, 1975] suggests U_w^2 will be amplified relative to the internal wave energy in the rest of the water column. This should result in enhanced boundary layer dissipation and a boundary dissipation time scale shortened by a factor of R, the ratio of N deep in the water column to N near the base of the boundary layer. Considering two under-ice-locations, B and C, with similar forcing, but markedly different N profiles such as the Beaufort Sea and Central Arctic Ocean, the difference in energies due to the difference in stratification would be $\frac{E_B}{E_C} = \frac{R_B\left(R_C\tau_{BL} + \tau_{OW}\right)}{R_C\left(R_B\tau_{BL} + \tau_{OW}\right)}$, where R_b and R_c are the N ratios at B and C respectively. Taking B to represent the Beaufort Sea and comparing N from 150 to 400 m to N at 10 m, we find $R_B = 0.24$ (Fig. 2.7a). Letting C represent the Central Arctic Ocean, $R_C = 0.85$. Thus, we expect that, owing only to boundary layer dissipation, internal wave energy and mixing in the Beaufort Sea to be a factor of 0.333 times the energy and mixing in the Central Arctic Ocean. The enhanced dissipation due to higher near-surface stratification in the Beaufort Sea could be responsible for a major fraction of the observed difference in internal wave energies between the basins.

Our argument does not include the effects of increasing ice velocity. If the typical RMS ice velocity increases because the ice is weaker, we might expect the dissipation of internal wave energy in the boundary layer to increase and tend to reduce internal wave energy. If the ice

moves faster because the ice is thinner and smoother we might expect a corresponding reduction on the ice-water drag coefficient and the effect on internal wave energies would be negligible. In any case, our observations suggest that in the presence of sea ice, boundary layer damping keeps internal wave energies and mixing low in spite of possible enhanced forcing due to increased ice mobility.

The average effect of boundary layer dissipation should decrease proportional to increases in the fraction of open water. This effect, along with enhanced ice motion, may overshadow the increase in under-ice boundary layer damping due summertime increases in stratification in the Beaufort Sea, where MMP-derived summer diffusivities are commonly, although not always, a little higher than wintertime diffusivities.

We add a cautionary note about stratification near the surface. The boundary layer model of *Morison et al.* [1985] assumes an unstratified boundary layer; a mixed layer of at least a few meters under the ice is required. If strong stratification extends to the very bottom of the ice, we might expect boundary layer stress and dissipation to decrease in the stable boundary layer, opening the way for temporary increases in internal energy. A more complete approach would allow for the effect of buoyancy flux [*Fer and Sundfjord*, 2007; *Perlin et al.*, 2005] in the oscillating boundary layer model.

Finally, our dissipation values across the halocline fall within the upper bound of turbulent dissipation presented in *Timmermans et al.* [2008] based on measurements made by *Halle and Pinkel* [2003] in the Canada Basin during the SIMI experiment. *Timmermans et al.* [2008] took the *Halle and Pinkel* [2003] calculated downward internal wave energy fluxes and assumed that all of the energy was dissipated in the halocline. By assuming that stratification

across the halocline averages $4x10^{-5}$ s^{-2} and that a typical CHL depth was 100 m, the measured internal wave energy flux of 0.15 mWm^{-2} would result in a diffusivity of $5x10^{-6}$ m^2s^{-1}. This is an upper bound because it requires all the energy to dissipate in the CHL, which is unlikely. Expanding the argument presented in *Timmermans et al.* [2008] and assuming average Arctic Ocean temperature gradients from our data (0.01°C m^{-1} in the Beaufort Sea and 0.0133°C m^{-1} in the central Arctic Ocean) and the same CHL depths and stratification, we find that diffusivities in the central Arctic Ocean across the CHL would have to reach $3.7x10^{-5}$ m^2s^{-1} for heat fluxes away from topography to reach 2 Wm^{-2}, the value required by *Maykut and Untersteiner* [1971] for oceanic heat to negatively affect sea ice concentration from the current thermodynamic balance. In the Beaufort Sea, diffusivity would have to be even higher to reach 2 Wm^{-2} given the less steep temperature gradients in that basin. Melting the ice from underneath in the central Arctic Ocean due to increased vertical mixing from the AW layer would require downward internal wave energy fluxes roughly 5 times as high (0.75 mWm^{-2}) as those measured by *Halle and Pinkel* [2003] during a strong storm event in the Beaufort Sea. Based on current measurements, it seems unlikely that heat fluxes of this magnitude across the CHL will happen in the near future without drastic changes in both surface forcing and temperature gradients. Increasing K_ρ in the Arctic Ocean to typical open ocean thermocline levels, 10^{-5} m^2s^{-1}, only results in heat fluxes ranging between 0.4 and 0.55 Wm^{-2}, slightly higher than double diffusive estimates [*Sirevaag and Fer*, 2012; *Timmermans et al.*, 2008].

Chapter 3. OBSERVATIONAL VALIDATION OF THE DIFFUSIVE CONVECTION FLUX LAWS IN THE AMUNDSEN BASIN, ARCTIC OCEAN

An edited version of this chapter was published by AGU. Copyright (2015) American Geophysical Union: Guthrie, J. D., I. Fer, and J. Morison (2015), Observational validation of the diffusive convection flux laws in the Amundsen Basin, Arctic Ocean, *J. Geophys. Res. Oceans*, 120, 7880–7896.

3.1 INTRODUCTION

The Atlantic Water (AW) layer persists throughout the Arctic Ocean as a subsurface temperature maximum (0.5 – 3°C), typically found at 200-300 m depths. The AW enters the Arctic Ocean through Fram Strait and circulates cyclonically around the basin with the Siberian continental slope on its right. Recirculation pathways of the AW exist along the southern side of the Nansen-Gakkel Ridge in the Nansen Basin as well as along the Eurasian side of the Lomonosov Ridge in the Amundsen Basin. Slightly cooler AW continues to follow bathymetry into the Makarov and Canada basins [*Rudels et al.*, 2004].

Starting at the surface, vertical profiles of water properties in the Amundsen Basin (AB) of the Arctic Ocean nominally consist of a low-salinity, cold mixed layer; a cold, saltier (cold halocline) layer and below, a warm, salty AW layer. The positive temperature and salinity gradients with depth above the AW core result in most of the AB being susceptible to the diffusive convective form of double diffusion (DDC) [*Kelley et al.* 2003]. A similar situation

applies to some extent for the majority of the Arctic Ocean. AW temperature maxima in the AB range from 1.0 to 1.3 °C, and salinity maxima are usually around 34.8. The commonly used form of the density ratio for DDC, $R_\rho = \beta\Delta S/\alpha\Delta T$, is a measure of the susceptibility of the water column to double diffusion, and DDC is expected for $1 < R_\rho < 10$. Here, β is the haline contraction coefficient, and α is the thermal expansion coefficient of seawater. Please note that for the salt fingering regime, R_ρ is typically defined inversely. Through the thermocline in the AB, R_ρ usually ranges between 3 to 4 and is slightly lower than in the Canada Basin overall [*Padman and Dillon*, 1987; *Sirevaag and Fer,* 2012; *Timmermans et al*., 2008].

In the deep basins of the Arctic Ocean, turbulence levels are low. The strength of turbulence is typically quantified by the dissipation of turbulent kinetic energy, ε, obtained by integrating the small-scale shear variance spectrum measured by airfoil shear probes on microstructure profilers. Away from topographic features, previous shear microstructure measurements in the Arctic Ocean have had trouble resolving the low levels of turbulence. During the Arctic Internal Wave Experiment (AIWEX) in the Canada Basin in 1985, *Padman and Dillon* [1987] found ε to be near the noise level of their instrument throughout the experiment. More recently, *Fer* [2009] and *Sirevaag and Fer* [2012] report diapycnal diffusivities of $O(10^{-6})$ m^2s^{-1} at depths less than 200 m but below that, ε typically falls below the noise level of their instruments. Internal wave energy levels have typically been an order of magnitude or more lower than mid-latitude open ocean conditions [*Levine et al.,* 1987], and comparisons of historical and recent shear measurements [*Guthrie et al.*, 2013] indicate this continues to be true in spite of declines in the ice cover. Thus, non-mechanical mixing regimes like double diffusion potentially dominate the vertical fluxes of heat and salt.

Double diffusion results when an unstable distribution of either temperature or salinity in the water column is compensated by a stable distribution of the other. In the salt fingering (SF) case salinity is the destabilizing agent as warm, salty water overlies cooler, fresher water. In the diffusive convective case, the opposite occurs as cool, fresh water overlies warm, salty water so that temperature is the destabilizing agent. This sets up an instability that results in the creation of a thermohaline staircase where the water column consists of homogeneous mixed layers separated by thin, high-gradient interfaces in both *T* and *S*.

Based on studies of single-component (e.g. thermal) convection, laboratory laws regarding the fluxes through two-component (*T* and *S*), high-gradient interfaces have been devised based on the density ratio, R_ρ, and the property jumps ΔT and ΔS across the interface. This provides an easily applied method for estimating fluxes in an oceanographic context as actual gradients are much harder to measure, but ΔT and ΔS can be ascertained from standard CTD data.

The original parameterization was presented in *Turner* [1965] based on theories of single-component convection as a scaling in terms of the Nusselt Number (*Nu*), the heat flux relative to conductive heat flux through the layer, and the Rayleigh Number (*Ra*), the strength of the thermal forcing relative to viscous damping of convection:

$$Nu = \frac{F_H}{c_p \rho k_t (\frac{\Delta T}{H})} \quad , \qquad (3.1)$$

$$Ra = \frac{g \alpha \Delta T H^3}{\upsilon k_t} \qquad (3.2)$$

$$Nu = cRa^\eta \quad . \quad (3.3)$$

In the above equations, c is an empirical function and $F_H, c_p, \rho, k_t, g, H,$ and ν are the heat flux across the interface, the specific heat capacity, the density, the molecular diffusivity of heat, gravitational acceleration, layer height, and the kinematic viscosity, respectively. For large *Ra* convection, the heat flux, F_H, should show no dependence on layer height, H, because fluid parcels near the top of the convecting layer should only be influenced by parcels nearby rather than parcels at the bottom of the layer. Thus, η is traditionally chosen as 1/3 to remove dependence of F_H on H [*Turner*, 1965].

For double diffusive convection, *Turner* [1965] showed that c was a function of the density ratio, $c(R_\rho)$. Two formulations of this variable are commonly used currently. Based on existing laboratory studies, *Kelley* [1990], K90, proposed the empirical function,

$$c(R_\rho) = 0.0032e^{\left(\frac{4.8}{R_\rho^{0.72}}\right)} \quad . \quad (3.4)$$

A more recent 3-D direct numerical simulation discussed in *Flanagan et al.* [2013], F13, found the following relation to be more accurate:

$$c(R_\rho) = 0.0157 + 0.0505(R_\rho - 1)^{-1.24} \quad . \quad (3.5)$$

With $\eta = 1/3$, the heat flux can be computed by what is commonly referred to as the 4/3rd laboratory flux law:

$$F_H = c(R_\rho)\rho c_p \left(\frac{g k_t^2 \alpha}{\upsilon}\right)^{1/3} (\Delta T)^{4/3} \quad . \qquad (3.6)$$

However, *Flanagan et al.* [2013] note that (3.5) corresponds to the use of the 1/3rd exponent in (3.3) which they claim represents their experiment poorly and suggest a downward revision. *Kelley* [2003] also questions the use of $\eta = 1/3$ in (3.3), but suggests it be retained until observational evidence indicates otherwise. A recent examination of a diffusive convective staircase in Lake Kivu, Africa yields $\eta = 0.2$ [*Sommer et al.,* 2013a]. However, other laboratory and numerical simulations of single-component convection suggest a more moderate downward revision than *Sommer et al.* [2013a]. While a thorough review of single-component Rayleigh-Bernard convection literature is outside the scope of this introduction, *Niemela et al.* [2001] show that $\eta = 0.31$ provides the best fit to their data and *Kerr* [1996] finds $\eta = 0.29$ provides the most accurate representation. Despite somewhat conflicting results, recent literature has provided mounting evidence that a downward revision of η is necessary.

The presence of diffusive convective thermohaline staircases in the Canada Basin of the Arctic Ocean has been documented since the 1960s [*Neshyba et al.,* 1971]. *Padman and Dillon* [1987] studied it in more detail with a suite of microstructure measurements made during AIWEX and *Timmermans et al.* [2008] with Ice-Tethered Profilers (ITPs) during the 2000s. *Padman and Dillon* [1987] found heat fluxes to be low, around 0.1 Wm^{-2}, and that the 4/3rd laboratory flux laws agreed to within a factor of two with the molecular heat fluxes across the interface. *Timmermans et al.* [2008] found slightly higher heat fluxes averaging 0.22 Wm^{-2}, and attributed this to an increase in the AW temperature maximum in the Canada Basin over the previous 20 years. They also made a comparison to temperature data from a single microstructure profile reported by *Rainville and Winsor* [2008] and found similar agreement to

the results presented in *Padman and Dillon* [1987]. Detailed spatial coverage of the staircase is presented for the first time in *Timmermans et al.* [2008], where the ITPs revealed that a thermohaline staircase was present between 200 – 300 m depths in 95% of the profiles made over the deep part of the Canada Basin.

The existence of thermohaline staircases in the Eurasian Basin appears more sporadic. A staircase similar to the one found in the Canada Basin was reported by *Sirevaag and Fer* [2012] during two different microstructure field experiments in the AB in 2008. *Polyakov et al.* [2012] used data from a McLane Moored Profiler attached to a bottom mooring on the Laptev Sea slope to report on a thermohaline staircase quite different than ones previously reported in the Arctic Ocean [*Padman and Dillon*, 1987; *Timmermans et al.,* 2008; *Sirevaag and Fer,* 2012]. The Laptev slope staircase was comprised of thicker (O(1) m) interfaces and (O(10) m) layers and purportedly much higher heat fluxes, O(1) Wm^{-2}, than previous studies. The *Polyakov et al.* [2011] heat fluxes are derived using the *Kelley* [1990] formulation and are significantly higher than other results due to much greater ΔT, 0.25 °C, and much lower R_ρ, 1.8-2.4.

None of the Arctic observations reviewed above were designed to resolve the heat fluxes through the thermohaline staircases. This paper discusses observations purposely designed to improve on previous tests of the validity of the $4/3^{rd}$ laboratory flux law heat flux parameterizations applied to oceanographic measurements made in the Amundsen Basin of the Arctic Ocean. Here, double diffusive heat fluxes predicted by laboratory flux law parameterizations are compared to heat fluxes calculated from direct temperature microstructure measurements: conductive, molecular fluxes in the interfaces, and the turbulent non-conductive heat fluxes in the convective layers. Furthermore, since temperature gradient spectra in the interfaces have not been previously reported, the temperature gradient spectra and the dissipation

rate of thermal variance are presented and contrasted between the interfaces and the layers, The value of the convective exponent, η, in (3.3) is explored, and these results are discussed in terms of their basin-wide implications. Data collection and processing methods are presented in Section 3.2. Results are given in Section 3.3. Conclusions and departures from previous literature are discussed in Section 3.4.

3.2 DATA AND METHODS:

3.2.1 *Overview and Hydrography:*

Observations were made from a drifting ice camp, Barneo, in April 2013. The measurement period began on 4/11/2013 when the camp was located at 89° 33' N, 87° 24' W and ended on 4/19/2013 at 89° 07' N, 62° 18' W after the camp drifted along the Eurasian flank of the Lomonosov Ridge (Fig. 3.1). Over this time, a total of 42 casts down to 350 m were made through a 51-cm hole in the 1.5 m thick sea ice. The instrument package consisted of a Seabird (SBE) 19+ CTD attached to a Rockland Scientific International Microrider (RSI MR-1000) internally recording microstructure instrument. Sensors on the Microrider included 2 shear probes to measure micro-scale shear perturbations as well as 2 Thermometric FP07s thermistors to measure micro-scale temperature fluctuations. The fast-response thermistor signal was pre-emphasized in a separate channel for high-resolution temperature gradient measurements, crucial for dissipation rate calculations. In this study, only dissipation rates inferred from FP07 measurements are reported. The instrument package was lowered with a winch at a speed of 20-

25 cms^{-1}. The SBE 19+ sampled at a rate of 4 Hz while the RSI MR-1000 sampled at 512 Hz. Manufacturer specified instrumental errors on the SBE 19+ are 0.005 °C in temperature and 0.0005 Sm^{-1} in conductivity. All salinity data discussed hereafter are derived from the SBE 19+. Due to sensor drift typical of fast-response thermistors, temperature data from the FP07s were were calibrated against the more accurate SBE 19+ measurements using a running 3rd order polynomial fit over 10-cm sections of data.

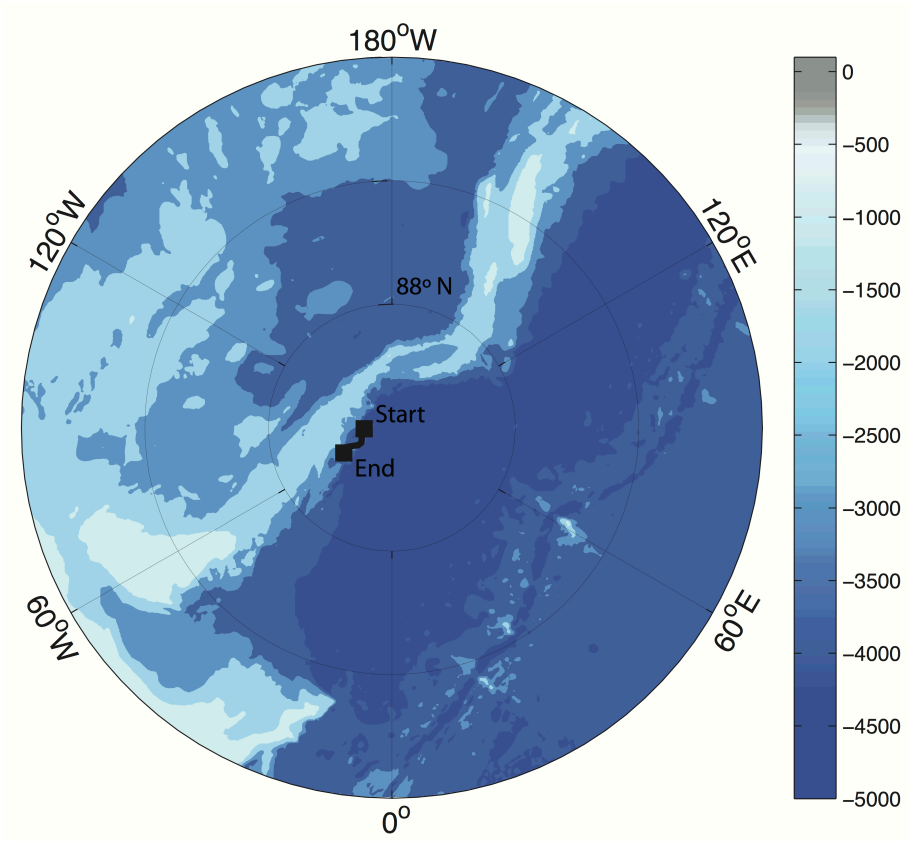

Figure 3.1. A map of the drift. The camp drifted mainly south along the flank of the Lomonosov Ridge.

Bulk T-S properties changed little over the course of the drift, implying small horizontal gradients. A sample profile of *T* and *S* versus depth from the midpoint of the drift is shown in

Figure 3.2. AW temperature maxima occurred at roughly 300 m depth and ranged between 1.1 and 1.2 °C, while AW salinity maxima occurred at the same depth and were roughly 34.8. The insets show details of interfaces and layers from the portion of the water column containing a thermohaline staircase. The staircase nominally begins at 150 m depth and extends to 230 m depth although there is variability between profiles. Often, interfaces and layers appear in the region directly above the AW temperature maximum as well.

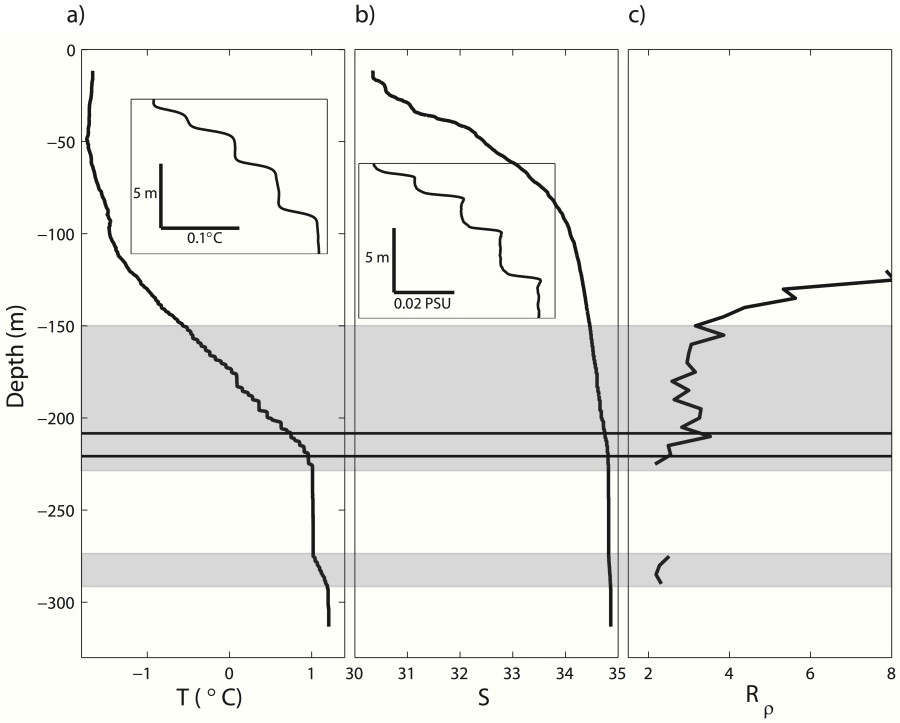

Figure 3.2. Sample temperature, salinity and R_ρ profiles from the SBE 19+. R_ρ is based on 5 m linear fits to T and S. Gray shading highlights depths where interfaces are found. The salinity scale makes resolution of individual interfaces difficult. Insets in temperature and salinity are shown.

Mixed layer depths were small throughout the drift, relative to an average springtime value in the Eurasian Basin of 71 m [*Peralta-Ferriz and Woodgate,* 2015]. Mixed layer depth was calculated as the depth at which $\Delta\rho > 0.1$ kgm^{-3} relative to the uppermost measurement. The mean mixed layer depth was 22 m. A roughly isothermal layer near the freezing point, T = -1.6

°C, was present down to approximately 60 m during the course of the experiment. The analysis presented in this paper will focus mainly on aspects of the thermohaline staircase between 150 and 250-m depths. Density ratio used in the calculation of (3.4) and (3.5) is obtained using ΔT and ΔS, the temperature and salinity jumps across the interfaces respectively. Mean staircase parameters were: ΔT = 0.026 °C, ΔS = 0.007, h = 0.1 m, H = 1.33 m, R_ρ = 3.45, Ra = 1 x 10^9, where h is the height of the interface. Histograms of these parameters derived from 360 interfaces are shown in Figure 3.3.

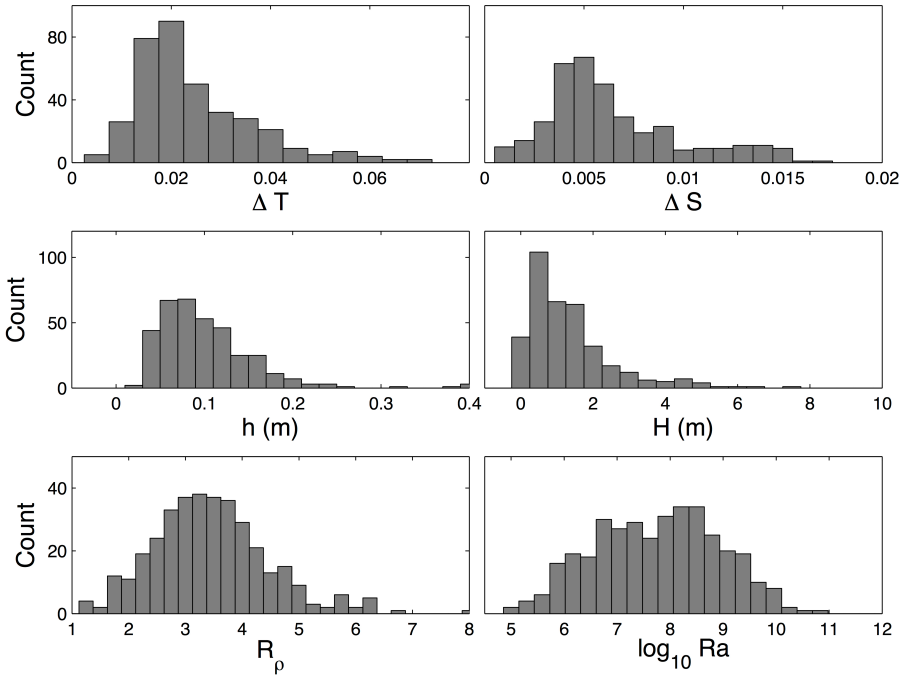

Figure 3.3. Histograms of ΔT, ΔS, h, H, R_ρ and Ra are shown using data from 360 interfaces.

3.2.2 *Spectral Analysis:*

Dissipation rate of thermal variance is obtained by spectral analysis of well-resolved temperature gradient spectra, both in the turbulent convective layers and the quiescent interfaces. A comparison of spectral levels and dissipation rates in the diffusive convective interfaces and

layers has not been previously reported. Furthermore, measurements of turbulent heat flux from microstructure profiling relies on the eddy diffusivity of heat, K_T, which is related to the dissipation rate of thermal variance, χ. The latter is measured by integrating wavenumber spectra of temperature gradient. The details of the calculations are summarized in the following. Frequency spectra of temperature gradient were calculated from the high-resolution FP07 data extracted from the homogeneous layers and from the high gradient interfaces in the thermohaline staircase. Only interfaces thicker than 10 cm were used in spectral calculations to insure a reasonable spectrum was resolvable. Extracted temperature gradient segments were detrended by removing the mean temperature gradient calculated from a linear fit in temperature-depth space and then windowed using a 50% Tukey window. Hanning, Hamming, and Bartlett windows were also tested and yielded comparable results. A Tukey window was chosen since it provided roughly 10% smaller (i.e., conservative) values of χ. Layer spectra were computed using Welch's modified periodogram if $H > 1$ m (~ 4 s of data). A standard periodogram if $H < 1$ m, since averaging the shorter segments changes induces unrealistic values at the lowest frequencies. When the Welch's method was applied, each layer was split into 8, 50% overlapping segments. Individual spectra of the subsegments were calculated and then averaged together to calculate the spectrum for the layer.

Due to the smaller data segments of the interfaces, 0.3-0.5 s of data, interface spectra were computed using a standard periodogram. No spectral content at frequencies greater than 50 Hz was used and typically the temperature gradient spectra in both layers and interfaces reached the diffusive roll-off portion, e.g. the part of the spectrum where molecular diffusion takes over, at frequencies much lower than 50 Hz. The attenuation of the signal due to the glass bead around the thermistor is accounted for using the *Gregg and Meagher* [1980] formulation, $H^2(f) =$

$(1 + (f/f_c)^2)^{-2}$, where $f_c = 1/(2\pi\tau W^{-.32})$, τ = 12 ms and W is the profiling speed. This correction was applied in the frequency domain. Frequency spectra were then converted into wavenumber spectra by dividing by the profiling speed of the instrument. For the wavenumber ranges typically analyzed in this data set, the correction for the time response results in only a modest recapture of the lost variance.

The dissipation rate of thermal variance, χ, is computed as

$$\chi = 2k_t < 3(\partial T'/\partial z)^2 > \quad . \qquad (3.7)$$

In (3.7), $(\partial T'/\partial z)^2$ represents micro-scale temperature gradient variance, and is obtained by integrating the spectra to a cutoff wavenumber at which the noise begins to dominate. A noise spectrum for temperature gradient spectra was created by averaging the most quiescent (lowest fifth percentile) sections of individual profiles, identical to the method presented in *Peterson and Fer* [2014]. Integrating the noise spectra out to 100 cpm, roughly the highest cut-off wavenumber for integration used in this study, reveals a noise floor in χ of O(10^{-12}) °C^2 s^{-1}. The factor of 3 in (3.7) follows from the assumption of local isotropy. It is unclear whether the isotropic assumption is valid within the high gradient interfaces and is therefore excluded from interface χ estimates (i.e. we exclude the factor of 3 in the interfaces, assuming that $\partial T'$ is relevant only in the z-direction). However, a recent numerical simulation in a low R_ρ environment suggests that isotropy is reduced, but not entirely absent, when double diffusive processes are dominant [*Flanagan et al.,* 2014]. Full isotropy is assumed (e.g. a factor of 3) for χ estimates within the homogeneous convecting layers. For the calculation of χ across interfaces and layers, the cut-off wavenumber was chosen following the maximum likelihood approach of

Ruddick et al. [2001], where a cut-off wavenumber was estimated by integrating the temperature gradient spectrum out to the highest wavenumber where the value of the spectrum was 1.5 times higher than the value of the noise spectrum at the same wavenumber. The curve fits to theoretical Kraichnan or Batchelor scalar turbulence spectra [*Batchelor*, 1959; *Kraichnan*, 1968] via this method also allow us to indirectly infer ε without shear probes. A recent underwater glider based study highlights the applicability of this method by comparing concurrent temperature and shear microstructure measurements [*Peterson and Fer*, 2014]. For 85% of their data, Peterson and Fer found that shear probe derived dissipation and the *Ruddick et al.* [2001] curve-fitting method agreed to within a factor of 2.8, with better agreement at lower turbulence levels. Values of ε reported in Section 3.3.4 are all inferred from the temperature gradient spectra measured by the FP07s.

3.2.3 *Heat Flux*

Heat flux calculations are made in the convective layers and interfaces. In the interfaces, we obtain the conductive heat flux using the molecular diffusivity of heat and standard Fickian diffusion,

$$F_H = -\rho c_p k_t \frac{\partial T}{\partial z} \quad . \quad (3.8)$$

We discuss methods for calculating interfacial $\frac{\partial T}{\partial z}$ in section 3.3.1. In the turbulent layers, we rely on the Osborn-Cox (OC) model,

$$K_T = \frac{\chi}{2<\frac{\partial T}{\partial z}>^2} \quad , \qquad (3.9)$$

to calculate an eddy coefficient for thermal diffusivity in the layers, and then compute the turbulent heat flux in the convective layer using (3.8) [*Osborn and Cox*, 1972]. In the application of (3.8) we use K_T (instead of k_t) and use the background temperature gradient from the sorted temperature in each layer. The OC model cannot be used in the interfaces since molecular diffusion determines the heat flux.

3.3 RESULTS

3.3.1 *Interface Structure*

The 360 interfaces included in this analysis were selected visually. The initial visual selection insures that only interfaces free of unusual disturbances such as inversions and spikes are used, as these complicate temperature gradient calculation. Once the interface is chosen visually, the beginning of the segment is determined as the first point where low-pass filtered (10 Hz) temperature gradient , $\partial T/\partial z$, increases beyond twice the large-scale background value (0.02 °Cm^{-1}), or $\partial T/\partial z$ > 0.04 °Cm^{-1}. Similarly, the end of the interface segment is chosen as the next point in the segment where $\partial T/\partial z$ drops below 0.04 °C/m. This results in a set of interfaces that appear primarily laminar, e.g. relatively smooth. However, an examination of the "laminar" interfaces in depth vs. $\partial T/\partial z$ plots reveals a variety of structures and forms. The complicated structure of interfaces when viewed in temperature gradient – depth space reveal the challenges associated with calculating temperature gradient across an interface. Four interfaces that appear smooth when viewed in temperature – depth space are shown in Figure 3.4 (a-d) in the left

panels. The same interfaces are shown in temperature gradient – depth space in the associated right panels. Temperature gradient calculated in three different ways are illustrated by the vertical lines. A linear fit across the interface in temperature – depth space, a linear fit across the middle 50% of the interface (following *Sommer et al.* [2014]), and the maximum temperature gradient measured by the FP07 across the interface are all used. The maximum temperature gradient recorded by the FP07 is often 2-6 times higher than values provided by the other methods. Through Eq. (3.8) this can have a similar effect on interfacial heat flux.

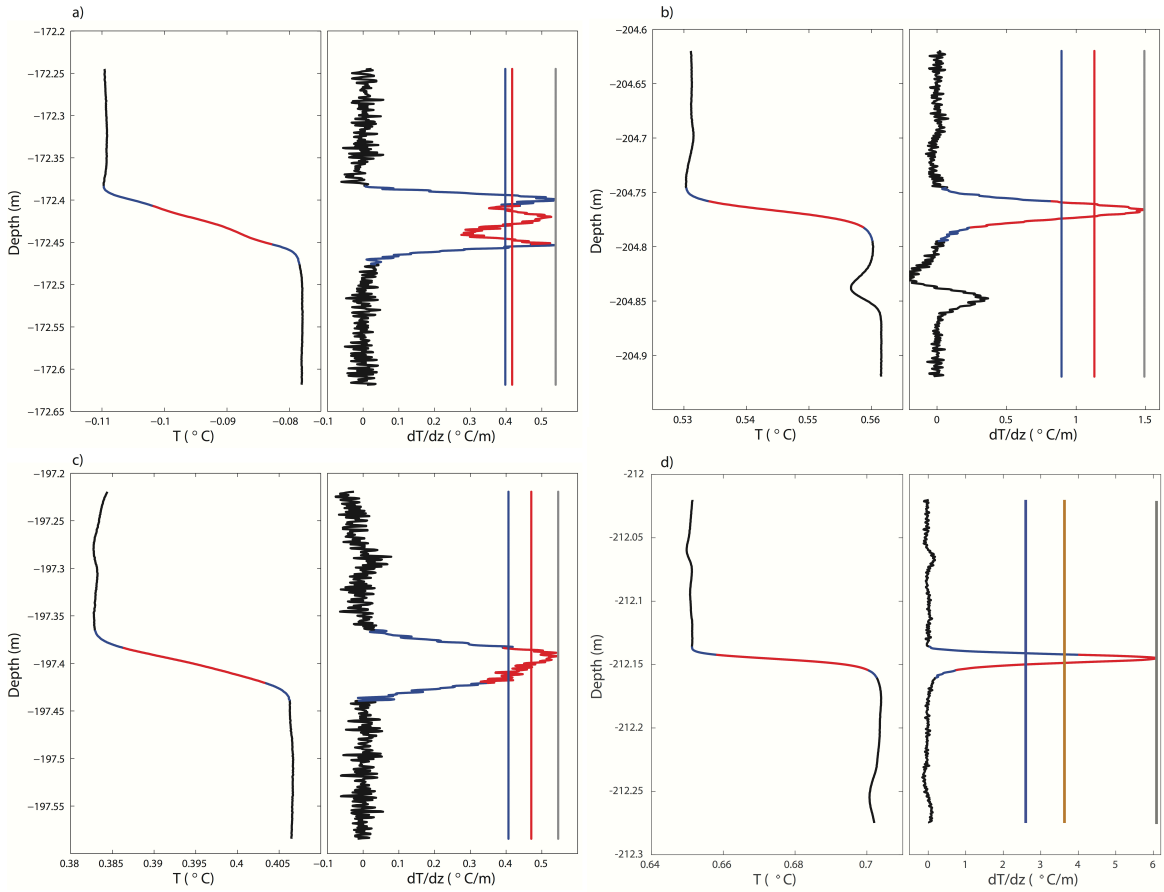

Figure 3.4. Temperature and temperature gradient data shown in this figure are taken from the FP07s. (a)-(d) represent four laminar appearing interfaces that look relatively similar in temperature-depth space but look quite different in temperature gradient-depth space. Data included in interface calculations, i.e. the segment determined by the algorithm in section 3.3.1, is shown in blue. The middle 50% of the interface is shown in red. The three vertical lines in the right subplots represent different ways to calculate temperature gradient. A linear fit to the middle 50% of the interface is shown in red, a linear fit to the interface is shown in blue and the maximum gradient in the interface segment is shown in gray.

The model proposed by *Linden and Shirtcliffe* [1978] assumes a constant temperature gradient across the core of an interface. Their Figure 1 shows a theoretical interface in temperature-depth space. The same interface shown in temperature gradient – depth space would resemble a boxcar function, with a discontinuity necessary to reach the constant core temperature

gradient at the layer-interface junction. Real, physical, oceanic interfaces are unlikely to have this idealized structure. We choose to define "cores" as the region where the temperature gradient lies within 10% of the maximum temperature gradient measured by the FP07. 85% of interfaces have cores that compose less than 30% of total interface thickness and 55% of interfaces have cores that compose less than 20% of total interface thickness. For the interfaces analyzed, mean core thickness was 1.8 cm, compared to a mean interface height of 10 cm. A comparison between the 30 Hz low-pass and raw data reveals that the interface cores are largely unaffected by high wavenumber instrument noise.

For most of the density ratio values observed here, a stable diffusive core exists near the nominal middle of the interface where the heat transport is purely molecular [*Worster*, 2004; *Sommer et al.* 2014]. The margins of the interface outside the core must present a mix of molecular and convective diffusion and consequently, a higher diffusion coefficient than purely molecular. And to the degree a profile is representative of quasi steady state heat flux through the interface, the minimum diffusion coefficient, i.e., molecular = k_t = 1.4 x 10^{-7} m^2s^{-1}, must be associated with the maximum temperature gradient. By this argument, using molecular diffusivity and the maximum temperature gradient recorded by the FP07 should provide an accurate measure of heat flux in the interface. This method has been previously reported in both *Sirevaag and Fer* [2012] and *Sanchez and Roget* [2007]. The mean maximum interfacial temperature gradient is 0.6 $°Cm^{-1}$. The value shown in Figure 3.4(d) is ten times this value, lending confidence to the ability of the FP07s to adequately capture the maximum temperature gradient within the interface core.

3.3.2 *Comparison with the 4/3rd Flux Law:*

Conductive heat flux, $F_{H(MOL)}$, across an interface is calculated using Eq.(3.8), molecular diffusivity k_t, and $\frac{\partial T_{MAX}}{\partial z}$, the maximum temperature gradient recorded by the thermistors in the interface. This flux is compared to the 4/3rd flux law estimates of both *Flanagan et al.* [2013] and *Kelley* [1990], $F_{H(F13)}$ and $F_{H(K90)}$, shown in equation (3.6). Turbulent heat fluxes in the layers derived from the OC model will be discussed in section 3.3.4. Both the laboratory experiments of *Kelley* [1990] and the DNS of *Flanagan et al.* [2013] let their experiments reach an equilibrium state before reporting results. For this reason, we have chosen to exclude the thickest and thinnest interfaces from this analysis. For $F_{H(MOL)}$, only the interfaces with thickness in the 10th to 90th percentile range are used, corresponding to interface height, h, between 4.7 cm and 16.3 cm, reducing the analyzed number of interfaces to 287.

$F_{H(MOL)}$ is well-correlated with both the *Kelley* [1990] and *Flanagan et al.* [2013] formulations of the 4/3rd laboratory flux law. A scatter plot of $F_{H(MOL)}$ versus both $F_{H(F13)}$ and $F_{H(K90)}$ is shown in Figure 5. We report the 24-hr averaged values of each quantity in Figure 3.5 as well since the recent numerical simulation of *Flanagan et al.* [2014] suggests that time averaging reduces measurement uncertainties. The correlations are slightly higher with *Flanagan et al.* [2013] than *Kelley et al.* [1990], r = 0.74 versus r = 0.70. Averaged across all interfaces examined, mean heat flux values are remarkably consistent, indicating the continued utility of the 4/3rd laboratory flux law parameterization. Mean $F_{H(MOL)}$ equals 0.33 Wm^{-2}, roughly 55% higher than $F_{H(F13)}$ (0.21 Wm^{-2}) and 100% higher than $F_{H(K90)}$ (0.16 Wm^{-2}). Unfortunately, we only have a small number of interfaces where R_ρ > 4, the value at which $F_{H(F13)}$ and $F_{H(K90)}$

really start to diverge (see *Flanagan et al.* [2013] Fig. 2b). When only interfaces where $R_\rho > 4$ are examined, $F_{H(F13)}$ appears to work much better than $F_{H(K90)}$ in comparisons with $F_{H(MOL)}$. The correlation coefficient, *r*, is only 0.01 higher but heat fluxes are much closer in magnitude for this range of R_ρ. $F_{H(K90)}$ equals 0.09 Wm^{-2}, while $F_{H(F13)}$ equals 0.14 Wm^{-2} compared to $F_{H(MOL)}$ equal to 0.27 Wm^{-2} (not shown). This highlights the improvement of (3.5) compared (3.4) when dealing with higher R_ρ. It is possible that the scatter in Figure 3.5 can be explained by the oscillating nature of the instantaneous heat flux through a single interface. We refer the reader to Figure 2a of *Flanagan et al.* [2013]. Their DNS shows that the staircase reaches a state of "quasi-equilibrium." Thus, while $F_{H(MOL)}$ could represent the instantaneous flux, $F_{H(F13)}$ might better represent a time-averaged flux through an interface not captured in the microstructure measurements. This agrees qualitatively with results presented in *Worster* [2004] that fluxes through interfaces are inherently time dependent.

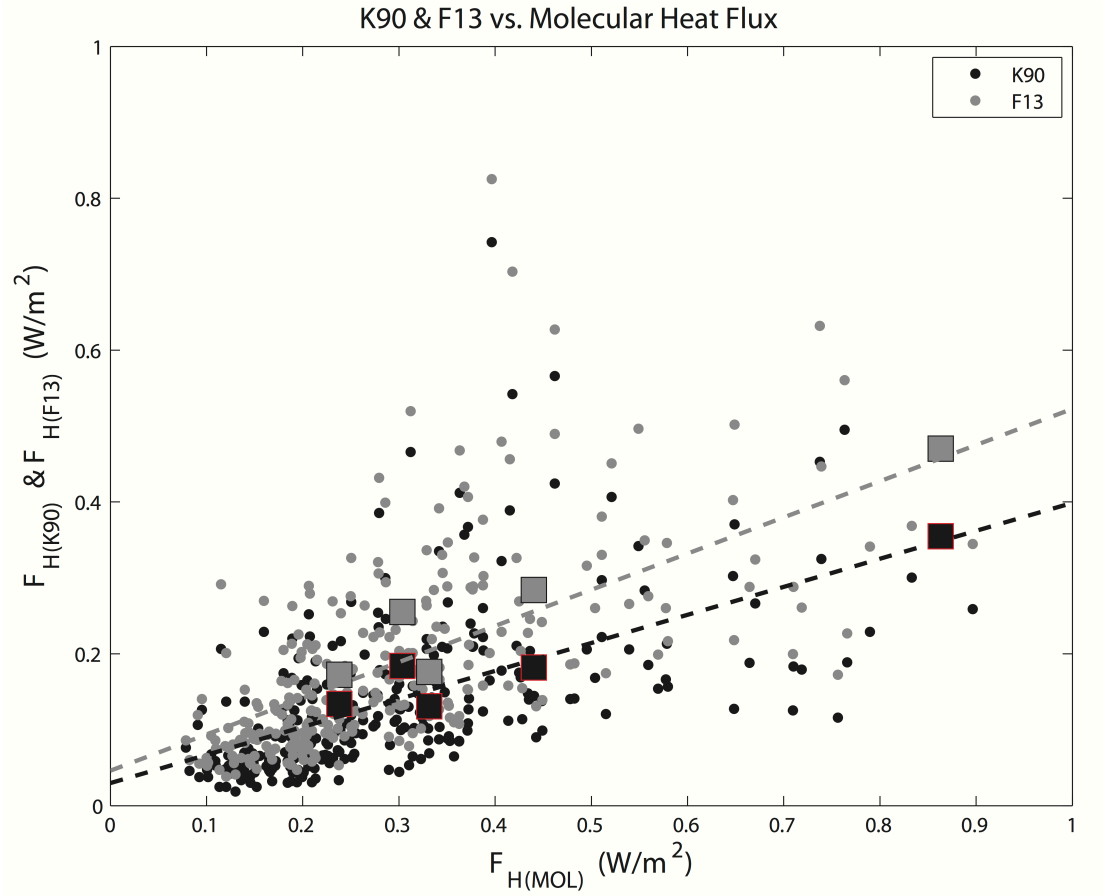

Figure 3.5. $F_{H(K90)}$ (black) and $F_{H(F13)}$ (gray) vs. $F_{H(MOL)}$ are shown. 24-hr averaged values are given by the large squares.

3.3.3 *Ra vs. Nu Scaling:*

Formulations of the 4/3rd flux laws are based on equations (3.1) to (3.3). This relationship implies that non-dimensional heat flux, *Nu*, is equal to the product of a function, *c*, of density ratio, R_ρ, and a *Ra* power law with exponent η. Previous results have suggested η = 1/3 to remove the *H*, layer height, dependence in the 4/3rd flux law (3.6) based on theories of single-component convection and a simple scaling argument. Although *Kelley* [1990] suggested a

downward revision of this exponent, he argued that it should remain 1/3 until some experimental evidence showed otherwise. A recent study of DDC in Lake Kivu, Africa [*Sommer et al*., 2013a] found evidence of $\eta = 0.2$ which they argue would require substantial downward revision of heat fluxes calculated using the extant 4/3rd flux laws for certain values of *Ra*. However, the authors considered only one power law fit (their Fig. 9a) and make no mention of the values of the correlation coefficient for their η estimation. The relationship is undoubtedly statistically significant as evidenced by the bootstrapping shown in their Figure 9b but examining their Figure 9a, it appears that $\eta = 1/3$ could provide a fit as reasonable as $\eta = 0.2$.

The same relationship from this data set is shown in Figure 3.6. *Nu* is calculated in (3.1) using $F_{H(MOL)}$ as described in the previous section. A power law fit to the relationship reveals $\eta = 0.29$ and the correlation between *Ra* and *Nu* is high, $r = 0.74$. We have chosen to use a parametric Kendall rank type correlation since it can better detect non-linear relationships [*Kendall*, 1983]. Performing the power law fit for 500 bootstrapped samples gives a 95% confidence interval error estimate (shown in brackets) such that $\eta = 0.29$ [0.28 0.31] [*Efron and Gong*, 1983]. The use of a Deming regression, which assumes equal error variance in both variables and provides another error estimate, gives a very similar answer, $\eta = 0.30$ [0.28 0.32] [*Deming*, 1943].

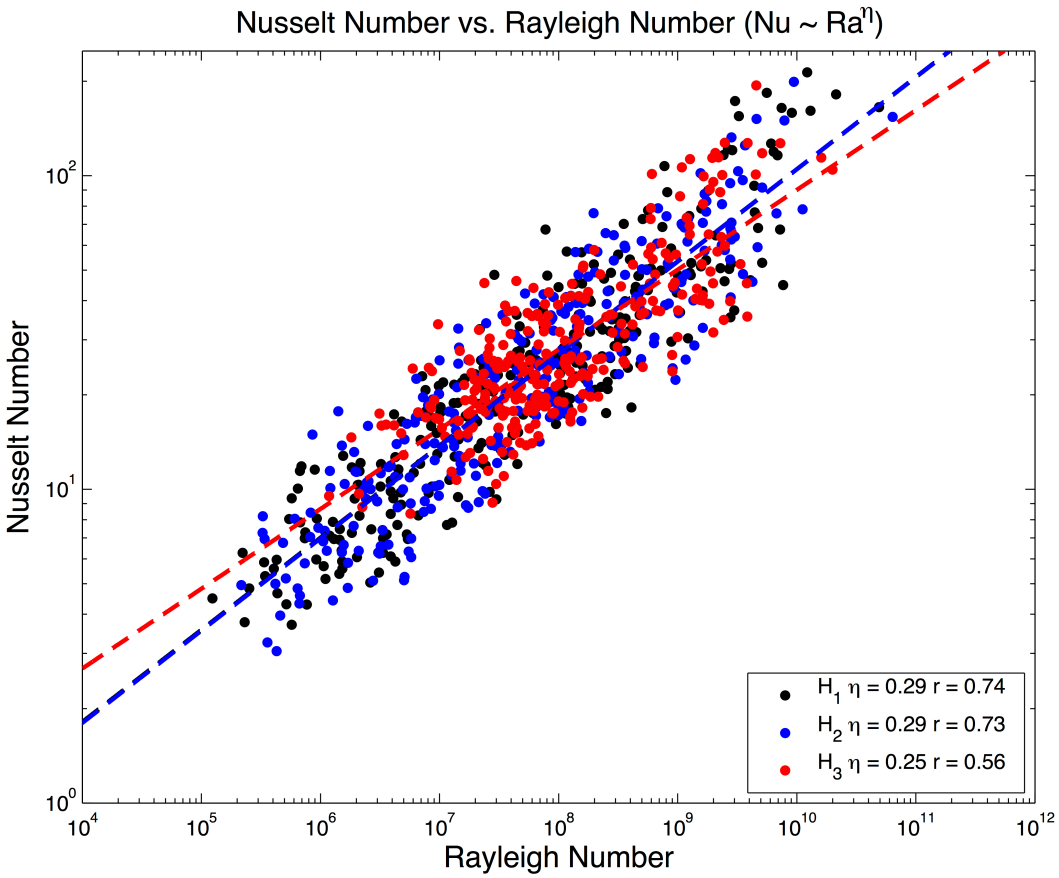

Figure 3.6. A plot of *Nu* vs. *Ra* for different methods of *H* calculation. Dashed lines show power law fits to the relationship. *Nu* is calculated as (3.2) where $F_H = F_{H(MOL)}$, while *Ra* is calculated as (3.3). H_1 (in black) = $H_{lower} + h$, H_2 (in blue) = $H_{upper} + h$ and H_3 (in red) = (H_{lower} + H_{upper} +)/2. Correlations and η values are given in the legend. The lack of points at the lower *Ra* range for H_3 due to averaging appears to bias the power law fit low.

This relationship appears sensitive to how *H*, layer height, is defined. *Sommer et al.* [2013a] calculate $H = (H_{upper} + H_{lower} + h)/2$ where H_{upper} is the layer height above the interface, H_{lower} is the layer height below the interface and *h* is the interface thickness. In this study, *H* is chosen as the layer below the interface, but we will now investigate the sensitivity of our results to how *H* is chosen. The relationship in (3.1) is tested using three separate definitions of *H*. $H_1 = H_{lower} + h$, $H_2 = H_{upper} + h$ and $H_3 = (H_{lower} + H_{upper} + h)/2$, The coefficient, η equals 0.29 [0.28

0.31] for H_1 and H_2, and 0.25 [0.23 0.28] for H_3. The Kendall rank type correlations are $r = 0.74$ for H_1, $r = 0.73$ for H_2, and $r = 0.56$ for H_3. The above values are given using only the 10^{th} to 90^{th} percentile range in interface thickness, however, the relationship is robust to the inclusion of all interfaces, with $\eta = 0.29$ [0.27 0.30] for H_1 and H_2 and $\eta = 0.24$ [0.21 0.26] for H_3, but lower correlations ($r = 0.66$, 0.64, 0.45 respectively). In Figure 3.6, the effect of collapsing Rayleigh number space is clear. Although the H_3 values populate the same envelope as H_1 and H_2, η is biased low since there are fewer values at the extreme ends of Rayleigh number space. While all three choices of H are physically reasonable, H_3 does not appear to be a good choice for our data set since there is no statistically significant relationship between H_1 and H_2 in our data set ($r = 0.01$ and $p > 0.85$), and the error bars on η estimates are roughly 50% larger than when using H_1 or H_2.

However, we must also account for the inclusion of $c(R_\rho)$ in (3.3). Because both (3.4) and (3.5) are based on the assumption that $\eta = 1/3$, we have chosen to perform the analysis above in bins of varying R_ρ following *Sommer et al.* [2013a]. Individual regressions are performed for 0.5 width bins of R_ρ from 2 to 5 for all 3 choices of H listed above. The bins contain the following number of interfaces, respectively: [30, 52, 57, 58, 37, 14]. These results are shown in Figure 3.7. Error bars shown are based on 95% confidence intervals from the use of a Deming regression. We have chosen to show these since they are more conservative (slightly larger) than the error bars determined through the bootstrap technique. While there appears to be a weak dependency of η on R_ρ (decreasing with increasing R_ρ), the range in R_ρ is too narrow and the error bars too large to be conclusive. This analysis suggests that our regression results from Fig 3.6 are not biased by the dependency of regressors on R_ρ. The mean value of η calculated this way agrees with the calculations in the previous two sections. For H_1, $\eta = 0.29$, for H_2, $\eta = 0.30$

and for H_3, $\eta = 0.26$. Not surprisingly, there is substantial bin to bin variability due to the smaller number of interfaces used. The mean values of η for different choices of H are identical with the first and last bins removed, i.e. only considering $2.5 < R_\rho < 4.5$.

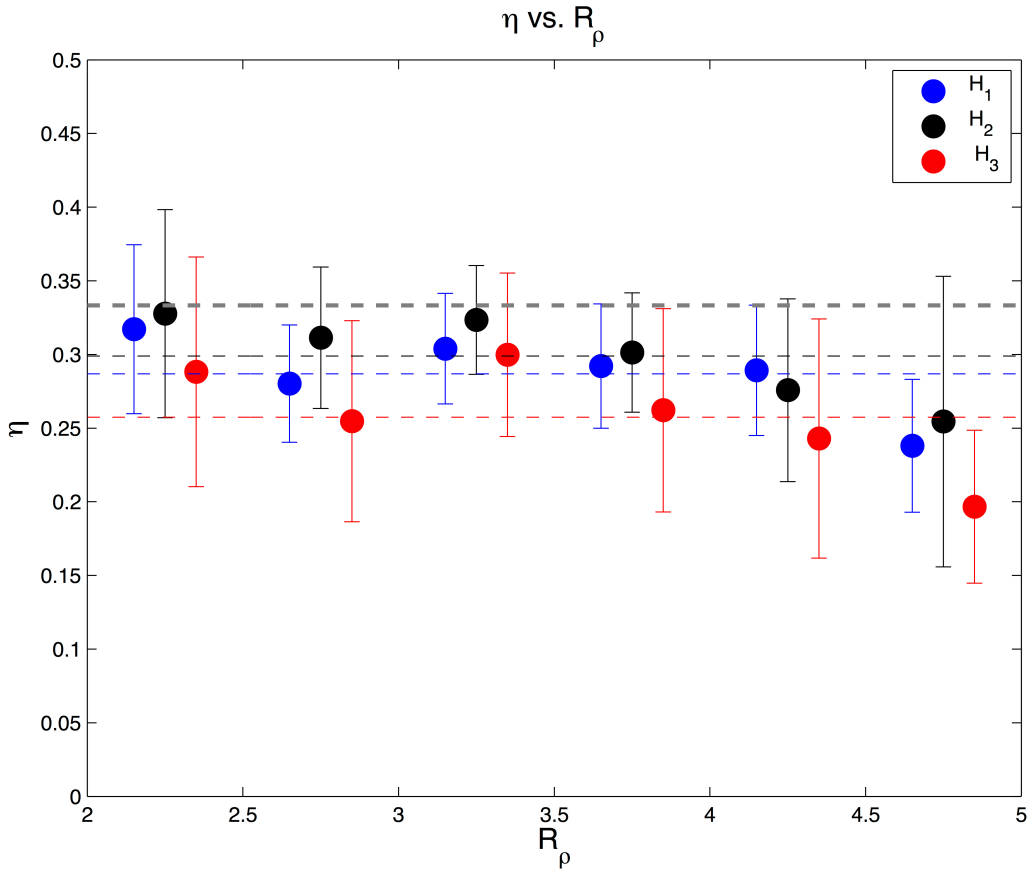

Figure 3.7. Plot of η vs. R_ρ. Circles are shown for different values of H. R_ρ is shown in 0.5 width bins from 2 to 5. Error bars are the 95% confidence intervals based on the Deming regression. We have chosen to show the error bars from the Demming regression instead of the bootstrap because they are slightly larger Dashed blue, black and red lines show the mean value of η for the three different choices of H. Dashed gray line is the canonical $\eta = 1/3$. Mean values of η for each choice of H are identical with the first and last bins removed, i.e. only considering $2.5 < R_\rho < 4.5$.

There is support in the single-component convection literature of a downward revision of η for the Ra ranges analyzed in our data set, although this is still an area of extensive research.

Direct numerical simulations of single-component convection have suggested that η = 2/7 ~ 0.29, very close to our values, might be the most appropriate choice [*Kerr*, 1996]. Kelley [1990] proposes a similar exponent. A laboratory study of single-component thermal convection by *Niemala et al.* [2001] found η = 0.31 over 18 orders of magnitude in *Ra*. If a downward revision of η is necessary, then heat fluxes should be slightly dependent on *H*. Regardless, the reintroduction of *H* into (3.6) changes heat flux values very little, as *H* = 1.36 m and η = 0.29 results in heat fluxes only 4% lower than predicted by the current flux laws. However, recalculating $F_{H(F13)}$ with η = 0.29 gives a mean interfacial heat flux of 0.36 Wm^{-2}, very close to the mean value of $F_{H(MOL)}$. A similar plot to Figure 3.5 is shown in Figure 3.8 but with $F_{H(F13)}$ calculated using η = 0.29 instead of η = 1/3. η = 0.29 is only applied to $(\alpha\Delta T)^{1+\eta}$, as this is the form presented in *Flanagan et al.* [2013] (see their equation 1). Color filled squares are averaged values binned by R_ρ ranging from 2 to 5 in 0.25 width bins. Note the nearly 1 to 1 correspondence between values for $R_\rho \geq 3$. We see some disagreement at low R_ρ. Thjis may be related to the fact that possibility of entrainment of fluid from the interface core is not represented in the calculation of $F_{H(MOL)}$. The recent numerical simulation of *Sommer et al.* [2014], reveals that mixed layer turbulence was only able to entrain interfacial fluid when $R_\rho < 3$.

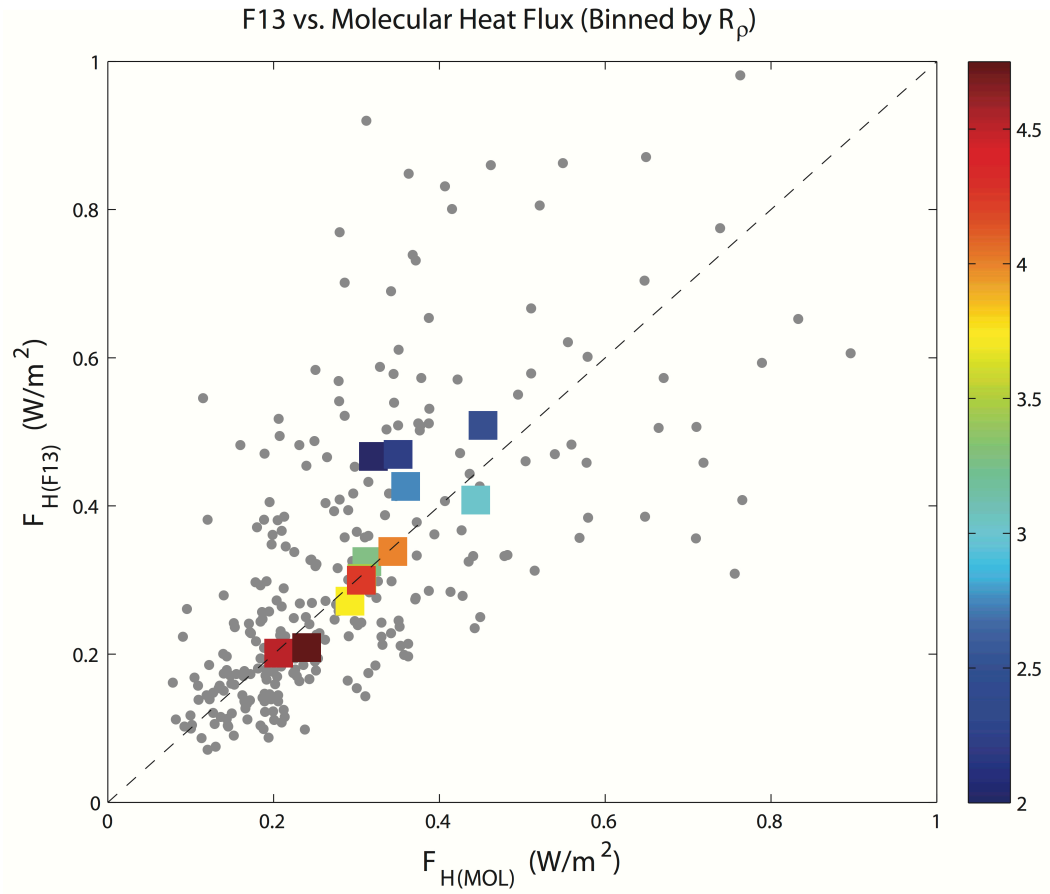

Figure 3.8. $F_{H(F13)}$ vs. $F_{H(MOL)}$ is shown. $F_{H(F13)}$ is calculated using η equals 0.29 as determined in section 3.3. Squares represent average values of $F_{H(F13)}$ and $F_{H(MOL)}$ binned by R_ρ (color scale) from 2 to 5 in 0.25 bin widths. The dashed gray and black lines show a linear fit to the data and a reference line for a perfect 1 to 1 correspondence, respectively.

3.3.4 *Spectral Calculations: χ and ε*

The average wavenumber spectra of temperature gradient are substantially different in the layers and in the interfaces. To ensure a reasonable interface spectrum is produced, we use a subset of the above data, consisting of 146 interfaces thicker than 10 cm to check on χ differences between layers and interfaces. χ in the interfaces is twenty times higher than in the

layers. Values reported below are based on the maximum likelihood estimator for a lognormal distribution, with 95% confidence intervals given in brackets. In the interfaces χ_{int} equals 6 x 10^{-9} C^2s^{-1} [4 x 10^{-9} 9 x 10^{-9}] and in the layers χ_{lay} equals 3 x 10^{-10} C^2s^{-1} [2 x 10^{-10} 5 x 10^{-10}]. This result is robust to whether or not the interface/layer pair passes the goodness-of-fit test listed in *Ruddick et al.* [2001] as well as to the choice of layer below or above the interface. Sample temperature gradient spectra and curve fits to theoretical Kraichnan spectra for an interface/layer pair are shown in Figure 3.9a. Admittedly, error bounds on individual interface spectra are quite large (a factor of 10) due to only 2 degrees of freedom. However, we report only χ_{int}, averaged over 146 samples, reducing the error bounds to less than a factor of 2. Averaged interfacial and layer temperature gradient spectra are shown in Figure 3.9b. Due to different segment lengths, individual spectra were first band-averaged to a common wavenumber vector (preserving total variance) and then averaged. The noise spectrum used in all spectral analysis is shown as well. The deviation at low wavenumber for the survey averaged interface spectra is similar to the results of *Dillon and Caldwell* [1982] for segments with low Cox number, $c = \langle(\frac{\partial T'}{\partial z})^2\rangle / \langle(\frac{\partial T}{\partial z})^2\rangle$. They argue that effects from the background temperature gradient can contaminate the low wavenumber part of the spectra, which seems especially applicable in the high gradient interfaces. In an attempt to address this problem in the interfaces, we have tried removing cubic and quadratic polynomial fits to the *dT/dz* segments before calculating spectra. Removing a cubic fit gives χ_{int} equals 3.3 x 10^{-9} C^2s^{-1}, a factor of two lower than the reported value above, but still an order of magnitude higher than χ_{lay}.

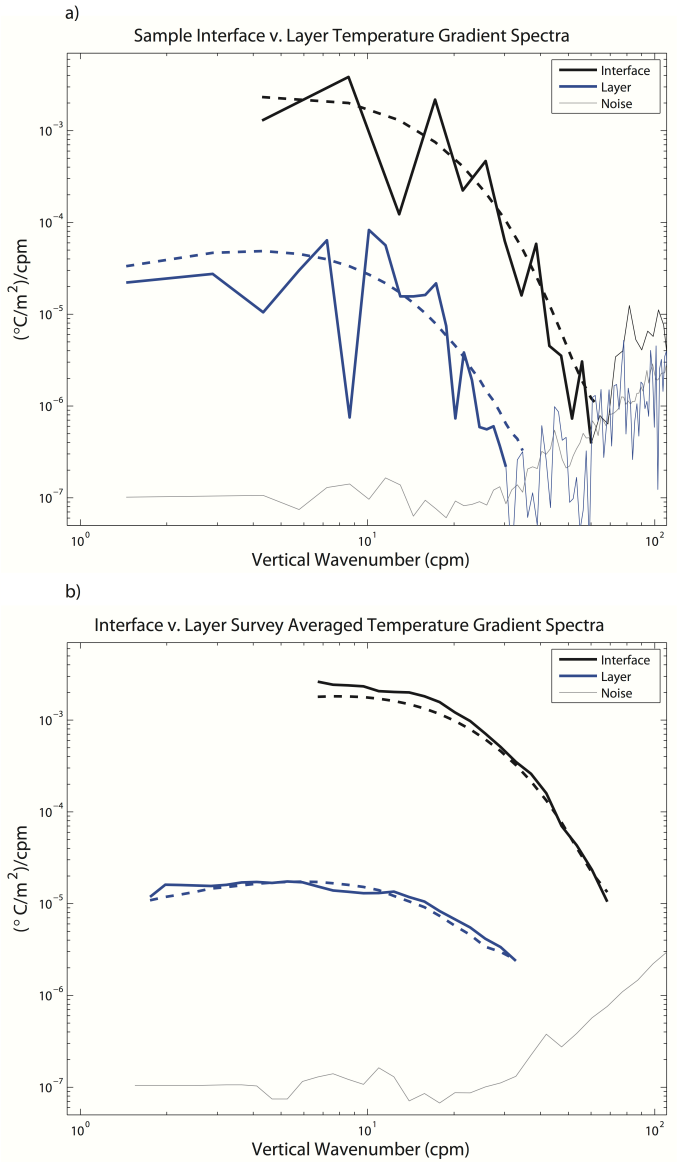

Figure 3.9. (a) Sample spectra are shown for an interface (black) and the layer (blue) directly below. Fits to the theoretical Kraichnan spectrum are shown in dashed. The noise spectrum for the data set is shown in gray. For this particular example, χ_{int}= 7 x 10^{-9} C^2s^{-1} and χ_{lay} = 5 x 10^{-10} C^2s^{-1}. (b) Survey averaged spectra are shown for interfaces (black) and layers (blue). χ_{int}= 4 x 10^{-9} C^2s^{-1} and χ_{lay} = 3 x 10^{-10} C^2s^{-1} for the survey averaged spectra.

Using the *Ruddick et al.* [2001] method also allows for the estimation of ε from the temperature gradient spectra in the interfaces and layers through curve-fitting. Only 54 of the interfaces and 65 of the layers used in the analysis pass the goodness-of-fit test. Compared to χ,

the difference in ε between the interfaces and layers is much smaller and of the same order of magnitude with ε_{int}= 5 x 10^{-10} Wkg^{-1} [3 x 10^{-10} 7 x 10^{-10}] and ε_{lay}= 3 x 10^{-10} Wkg^{-1} [2 x 10^{-10} 4 x 10^{-10}]. Curve fitting to the survey averaged spectra provides similar results for the interface but a slightly smaller ε_{lay}= 1 x 10^{-10} Wkg^{-1} [6 x 10^{-11} 2 x 10^{-10}] with error estimates providing the range of values in brackets. Given the small number of interfaces passing the goodness-of-fit test, the similarity of the result and the error bars involved, it is not possible to draw firm conclusions regarding dissipation rate of TKE. Indeed, direct calculation of ε using shear spectra in interfaces and layers is probably beyond the community's ability to resolve currently. Separation of layers and interfaces into different segments would be challenging and the calculation of ε across a 10-cm interface at typical shear-focused microstructure profiler drop rates (0.5 to 1 m s^{-1}) is probably not possible with only 0.1 s of data. The low ε levels expected at staircase depths in the Arctic Ocean, O(10^{-10} Wkg^{-1}), further complicate this issue. *Taylor* [1988] proposed that in a uniform, steady state staircase, the buoyancy flux through the interfaces would be dissipated in the layer above, e.g. $\varepsilon = B_\rho \approx \frac{g\alpha}{\rho c_p} F_H$ as presented in *Padman* [1994]. Using F_H = 0.33 Wm^{-2} predicts ε_{lay} = 4.7 x 10^{-11} Wkg^{-1}, which is just outside the error bounds on ε calculated from a theoretical Kraichnan fit to the survey averaged layer spectrum, indicating that the staircase is most likely not in equilibrium during our measurement period.

Spectral calculations made in the turbulent homogeneous layers also provide us with another method of calculating heat fluxes through the staircase through the application of (3.7), (3.8) and (3.9), $F_{H(OC)}$. χ is calculated from individual layer segments with spectral analysis described in Section 3.2.2. Following both *Sirevaag and Fer* [2012] and *Roget and Sanchez* [2007], we calculate $\partial T/\partial z$ used in (3.9) by sorting the temperature profile through a layer and

then performing a linear fit to the layer segment. Derived through this method, mean layer $F_{H(OC)}$ = 0.33 ± 0.02 Wm^{-2}, essentially identical to the value of $F_{H(MOL)}$.

Both results in ε and χ are qualitatively similar to the results presented in *Gregg and Sanford* [1987] from the salt fingering staircase east of Barbados during the CSALT experiment. They also found a nearly 2 order of magnitude difference in χ between layers and interfaces, $\chi_{int-CSALT}$= 1.1 x 10^{-7} C^2s^{-1} and $\chi_{lay-CSALT}$ = 5.7 x 10^{-9} C^2s^{-1}, although they did find three times larger ε in the interface compared to the layer, $\varepsilon_{int-CSALT}$= 4.9 x 10^{-10} Wkg^{-1} and $\varepsilon_{lay-CSALT}$= 1.4 x 10^{-10} Wkg^{-1}. The ε values presented in *Gregg and Sanford* [1987] were computed from shear microstructure measurements, where ours were determined indirectly through curve fitting to theoretical temperature gradient spectra, which might explain the slight discrepancy. They also show that the salt fingering laboratory flux laws overestimate the buoyancy flux through an interface by two orders of magnitude compared to the microstructure measurements. While the values of ε and χ presented in this study are quite similar to the results published in *Gregg and Sanford* [1987], the laboratory flux laws in the diffusive convective regime of double diffusion seem to do a remarkable job in predicting actual interfacial heat fluxes, as shown in the previous section.

3.4 DISCUSSION

Our observations of vertical heat flux through a thermohaline staircase in the Amundsen Basin of the Arctic Ocean agree well (within 55%) with parameterizations developed from theory and laboratory experiments. Assuming that the heat flux is constant through the interface, it can be calculated based on the molecular diffusivity of heat and the maximum temperature

gradient measured by the thermistors to yield $F_{H(MOL)}$. The 4/3rd flux law (3.6) based on laboratory results and using η equal to 1/3rd produces flux estimates 55% lower than $F_{H(MOL)}$. However, changing η from 1/3rd to 0.29 in (3.6) based on the findings in this study results in very similar mean staircase heat fluxes of 0.36 ± 0.02 Wm^{-2} when we use the slightly modified form of $F_{H(F13)}$ reported in section 3.3.3. These values are consistent with turbulent heat flux, $F_{H(OC)}$, calculated through spectral analysis and the use of the Osborn-Cox mixing model. This indicates that using extant flux laws based on a higher exponent will lead to underestimates of heat fluxes due to double diffusion. Modifying the laboratory flux laws as recommended above results in only a 10% difference between $F_{H(F13)}$, $F_{H(MOL)}$, and $F_{H(OC)}$, and even better correspondence for $R_\rho > 3$, as shown in Figure 3.8. We recommend future studies use this modified version until new formulations of $c(R_\rho)$ based on a smaller value of η are derived in the laboratory or through direct numerical simulation.

If the double diffusive heat fluxes are typically this small, is this correction important? One might argue that the data set (number of interfaces) is small and 0.33 Wm^{-2} as the mean staircase heat flux is not representative, but the 287 calculated interfacial heat fluxes are lognormally distributed (not shown) and should signify a representative subset. This value is nearly the same as the value presented in *Timmermans et al.* [2008] if η = 0.29 is used instead of 1/3. If we extrapolate this result to the total area of the deep basins of the Arctic Ocean (7 x 10^{12} m^3), this results in total vertical heat loss from the AW of 2.3 TW, or roughly 6% of the total heat transported into the Arctic Ocean through Fram Strait (41 TW). If we assume that $\eta = 1/3$ is correct, then, double diffusion likely results in 1.4 TW of vertical heat loss from the AW. While a difference of 1 TW is probably not large compared to interannual variations in basin-scale budgets since it is considerably smaller than interannual variability of the AW inflow

[*Schauer et al*., 2008], it is likely significant as a long-term bias in heat flux estimates, and an effort should be made to further verify the proper choice of η. While the lack of a consistent thermohaline staircase in the Amundsen Basin limits the applicability of these results to the smooth *T* and *S* profiles often found in this region, a recent study of shear-based parameterized mixing shows comparable heat flux values [*Guthrie et al.,* 2013].

The results presented in this study differ slightly from a pair of recently published articles [*Sommer et al.*, 2013a; *Sirevaag and Fer* 2012]. From their Lake Kivu dataset, *Sommer et al.* [2013a] found reasonable agreement between interfacial heat fluxes and the K90 version of (3.6). From their Lake Kivu dataset, *Sommer et al.* [2013a] found reasonable agreement between interfacial heat fluxes and the K90 version of (3.6). Recalculation of the exponents presented in *Sommer* et al. [2013a] using the three different definitions of *H* in *Ra* did not change the value of η they report (*J. Carpenter*, pers. comm., 2015). It is possible that their method of calculating molecular fluxes introduces some of the discrepancy. *Sommer et al.* [2013a] use measured $\partial T/\partial z$ at the midpoint of the interface, which could result in underestimating fluxes if maximum $\partial T/\partial z$ is not located at the exact midpoint. *Sommer* et al. [2014] use a linear fit to the middle 50% of the interface, which would result in lower values than the ones presented here as well. We also report mean ΔT 2.5 times as large as the Lake Kivu data set, 0.026 °C compared to 0.01 °C, which might further explain some of the differences in the comparisons of the results.

Sirevaag and Fer [2012] found that $F_{H(K90)}$ greatly overestimated $F_{H(MOL)}$ in their data sets from the AB. The disagreement between our results and *Sirevaag and Fer* [2012] can be attributed to at least two important differences between our methods. Firstly, the instrumentation and sampling is substantially different: the faster profiling speed (0.6 m s^{-1}) and the treatment of the temperature channel of their profiler MSS-90 (difference in electronics and further lowpass

filtering their data to 30 Hz, leading to smoothing on a 2-cm scale) likely limited the authors' ability to adequately resolve the temperature gradient in the 1-2-cm thick core of the interface. This would mean an underestimate in heat fluxes and explains their supposition that (3.6) vastly overestimated interfacial heat fluxes in their data set. Secondly, *Sirevaag and Fer* [2012] use ΔT from 10-cm averaged, precision CTD data (not the FP07 data at full resolution), to be consistent with the salinity jump ΔS used in staircase parameter calculations. It is highly likely that the scenario presented in the following paragraph could have affected their results by overestimating ΔT. Due to the nonlinear relationship to F_H in (3.6), this would significantly overestimate the heat fluxes determined through the use of the laboratory 4/3rd flux law parameterizations.

Challenges still exist in using the laboratory flux laws with CTD data, as even fast sampling, slowly profiled CTDs can erroneously show a single interface when the temperature microstructure profile reveals two. This could lead to a 100% overestimate in estimated heat fluxes. For the relatively small heat fluxes reported in *Timmermans et al.* [2008] and *Sirevaag and Fer* [2012], this is less consequential to the long-term thermodynamics because heat fluxes that small are unlikely to play any significant role in basin-scale AW heat budget considerations. However, this sampling problem could have profound impact on staircases similar to the one reported in *Polyakov et al.* [2012]. If O(0.1) m interfaces measured by the 4 Hz sampling SBE 19+ lowered at 25 cms^{-1} can be shown to consist of more than one interface in the FP07 thermistor data as in Figure 3.10, then it seems reasonable that the large, O(1) m interfaces measured by the 1 Hz sampling McLane Moored Profiler data reported in *Polyakov et al.* [2012] might contain multiple smaller interfaces. In such a case, the reported large heat fluxes, 2-8 Wm^{-2}, could represent a factor of two overestimate or more.

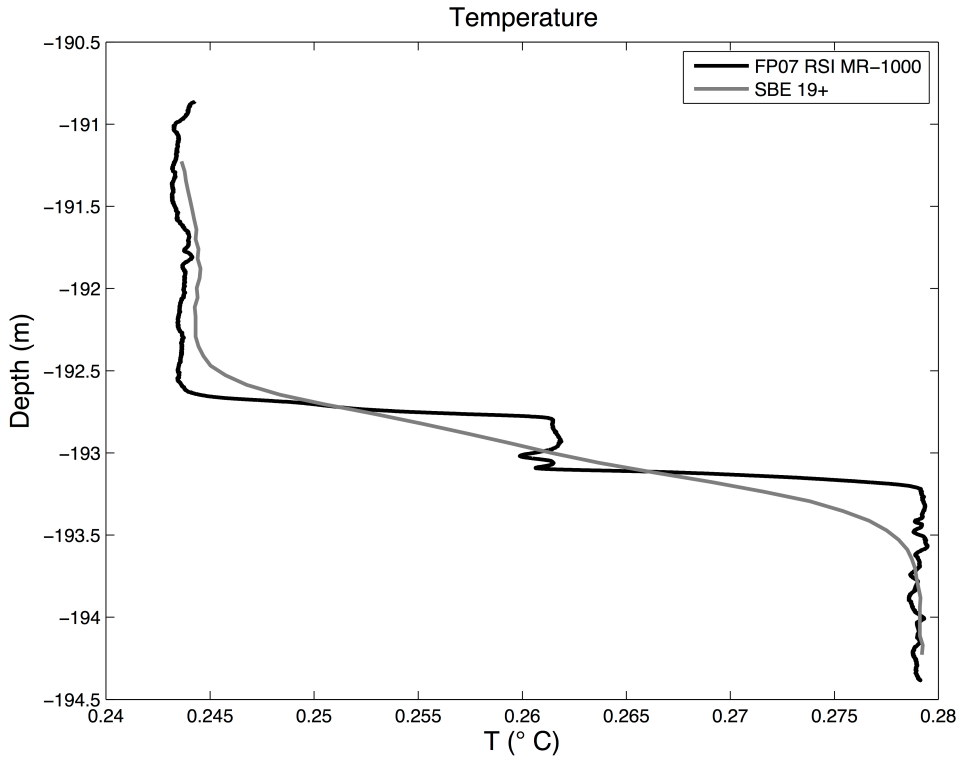

Figure 3.10. A sample interface is shown as seen by both the RSI MR-1000 (black) and the SBE 19+ (gray). Even though, the SBE 19+ samples at 4 Hz, compared to the 1 Hz sampling of ITPs and MMPs, it still resolves only a single interface when the MR-1000 clearly shows two.

During this drift, vertical heat fluxes from the AW core were small over the deep part of the Amundsen Basin and this suggests, as with previous studies, that most of the heat loss in the Atlantic Water layer in the Arctic Ocean must occur near the margins and over topography.

Chapter 4. THERMOHALINE STAIRCASES IN THE AMUNDSEN BASIN: POSSIBLE DISRUPTION BY SHEAR AND MIXING

An edited version of this chapter has been submitted for publication in Journal of Geophysical Research - Oceans.

4.1 INTRODUCTION

Collectively, wind and tidal forces are responsible for the input of an estimated 2 TW of energy into the abyssal ocean [*Munk and Wunsch*, 1999]. A large fraction of this energy can propagate across basins as low mode internal tides and near-inertial waves. Away from generation sites and topography, the turbulence generated by the breaking of these internal waves is thought to be the main mixing mechanism below the mixed layer in the deep abyssal ocean.

However, due to the different molecular diffusivities of heat and salt, another mixing mechanism, double diffusion, can occur in the ocean. Double diffusion occurs when large-scale vertical Temperature and Salinity gradients both increase or decrease with depth. If T and S both decrease with depth, e.g. warm and salty water overlies colder and fresher water, this is referred to as Salt Fingering (SF). If T and S both increase with depth, e.g. colder and fresher water overlies warmer and saltier water, this is referred to as Diffusive Convection (DC) [*Gregg and Sanford*, 1987; *Kelley et al.*, 2003]. The potential energy contained in the destabilizing tracer feeds the instability and generates turbulence. The importance of double diffusion as a vertical mixing mechanism is typically determined by the density ratio, R_ρ. Density ratio is determined

by large-scale vertical temperature and salinity gradients and is often referred to differently in the literature for SF and DC. For SF, $R_\rho = \alpha \frac{\partial T}{\partial z} / \beta \frac{\partial S}{\partial z}$ but for DC, $R_\rho = \beta \frac{\partial S}{\partial z} / \alpha \frac{\partial T}{\partial z}$.

For the most part, double diffusion is considered active in areas where thermohaline staircases occur. Thermohaline staircases are defined as regions of the water column containing thicker, homogeneous convecting layers separated by thinner, high-gradient interfaces. SF staircases are typically found only when $R_\rho < 2$ but DC staircases have been found when $1 < R_\rho < 10$ [*Gregg and Sanford*, 1987; *Kelley et al.*, 2003].

The question of how internal wave driven turbulence and shear and double diffusion coexist is largely still open, although more progress has been made in the salt fingering literature. One of the main differences between parameterized interfacial heat and salt fluxes for the SF and DC cases is the extent to which they depart from microstructure observations. Results from the CSALT experiment found that the fluxes derived from laboratory parameterizations overestimated measured interfacial fluxes from microstructure observations by an order of magnitude [*Gregg and Sanford*, 1987]. *Kunze* [1987] suggested that internal wave shear might be responsible by effectively tilting the salt fingers so they aligned in the horizontal rather than the vertical, decreasing vertical fluxes and becoming "salt sheets." This argument was supported by optical microstructure measurements showing extensive horizontal banding within the interfaces. It is also supported by results from a recent numerical simulation by *Radko et al*. [2015] that applied stochastic shear at oceanic background Garrett-Munk (GM) levels to a thermohaline staircase, finding that the shear decreased the salt fingering fluxes by a factor of two to three [*Garrett and Munk*, 1972]. While the authors do not comment on how turbulent mixing affects staircase formation in that article, they do discuss it in a previous paper. In a separate numerical simulation using average T and S structure reminiscent of the CSALT region,

Radko et al. [2014] find that staircase formation depends on both density ratio and turbulent mixing. For the density ratio typical of that region, R_ρ = 1.7, K_ρ < 1.35 x 10^{-6} m^2s^{-1} is necessary for the staircase to form. This mixing value is nearly an order of magnitude lower than those typically found in the mid-latitude open ocean [*Gregg*, 1987]. The *Radko et al*. [2014] results suggest the necessity for shear-driven turbulent fluxes to be lower than potential double diffusive fluxes to allow staircase formation.

The interaction between shear and thermohaline staircases for the DC case has not been examined nearly as thoroughly. Two of the only studies have focused on the interaction between thermohaline staircases and the vertical shear present in geostrophic eddies [*Padman,* 1994; *Bebieva and Timmermans*, 2015]. *Padman* [1994] suggests that the concentration of shear across high-gradient interfaces could actually enhance the double diffusive transport as the added shear could cause the interfacial Richardson Number, $Ri = N^2/S^2$, to approach the critical value, Ri = 0.25, required for shear instability. *Bebieva and Timmermans* [2015] present Ice-Tethered Profiler data of an Atlantic Water eddy in the Canada Basin and show that in areas of high geostrophic shear on the edges of the eddy, no staircase is present in the DC favorable stratification above the AW temperature maximum. However, in the eddy's core, where geostrophic shear is weaker, a staircase is present. The fact that DC staircases are typically found in quiescent waters like the Arctic Ocean [*Padman and Dillon*, 1987; *Timmermans et al.*, 2008; *Guthrie et al*., 2015], and geothermally heated lakes in Canada and Africa [*Scheifele et al*., 2015; *Sommer et al*., 2013] seems indicative of relatively low background mixing rates being necessary for staircase formation, especially since these staircases have been reported for a wide range of large-scale density ratio conditions, R_ρ = 2-7. To date, no results have been published similar to *Radko et al*. [2013] showing staircases only form for small K_ρ.

This article presents a straightforward comparison between two extremely similar temperature microstructure datasets collected in the Amundsen Basin of the Arctic Ocean in 2013 and 2014. We will use observations to show that enhanced upper-ocean mixing could be responsible for the absence of a thermohaline staircase in 2014 even though values of the density ratio suggest that double diffusion should be active. We also include data collected in a similar location in 2008 (previously published in *Sirevaag and Fer* [2012]) as an interesting companion data set. The paper is organized as follows. Data and methods are presented in section 4.2. Results, including general hydrographic data and mixing estimates are shared in section 4.3. Section 4.4 examines possible dynamical causes accounting for the differences in the T/S nature of the two surveys, possible heat flux divergence in the 2013 data, as well as more general basin-scale implications.

4.2 Data and Methods

4.2.1 *Overview*

The bulk of the data presented in this article were collected as part of the 2013 and 2014 field seasons of the North Pole Environmental Observatory (NPEO) staged from the Russian ice camp Barneo during April 2013 and April 2014. The 2013 data were previously reported in *Guthrie et al.* [2015]. The 2013 and 2014 measurement periods occurred in slightly different locations. The 2013 experiment started at 89° 33’ N, 87° 48’ W on April 11th. Measurements ended on April 20th at 89° 08’ N, 61° 45’ W, during which time a total of 42 casts were made. The 2013 ice camp largely drifted south on the Eurasian side of the Lomonosov Ridge towards the Canadian Arctic Archipelago. The 2014 measurements period began at 88° 35’ N, 15° 24’E on April 17th. Measurements ended on April 23rd at 88° 3’ N, 14° 15’ E, during which time a total of 50 casts were made. This ice camp began closer to the center of the Amundsen Basin and

drifted south towards Svalbard and Fram Strait. A map showing the locations of both drifts is presented in Figure 4.1. The NPEO 2007 and NPEO 2008 drifts and a single profile location near the Lomonosov Ridge, collected in 2008, previously reported in *Fer* [2009], *Fer* [2014] and *Sirevaag and Fer* [2012], are shown in this figure as well.

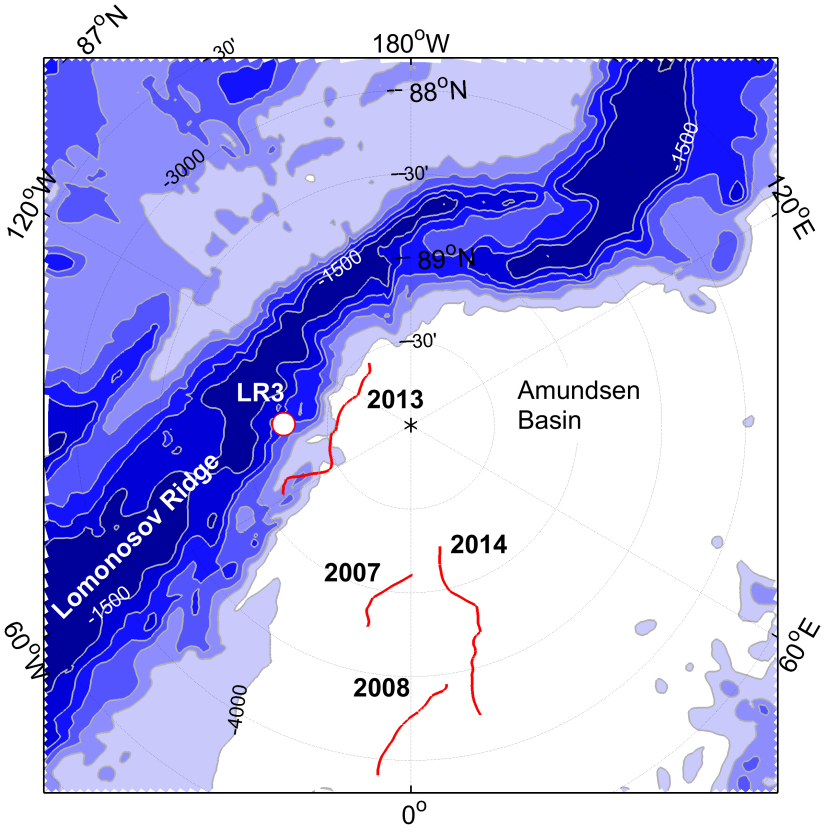

Figure 4.1. Map showing drift locations of NPEO 2007, 2008, 2013, 2014 as well as station LR3 made during NPEO 2008.

Both the NPEO 2013 and 2014 data sets consist of similar instrument configurations. Each uses an internally recording Rockland Scientific International Microrider (RSI MR-1000) equipped with 2 Thermometric FP07 fast response thermistors to measure temperature microstructure. Two different Seabird (SBE) CTDs were attached to the MR to provide more

accurate temperature and salinity measurements. In 2013, a SBE 19+ was used, while in 2014, an SBE 911+ was used. Measurements were made from a heated hut and a winch was used to lower the instrument package through a hole cut into the sea ice. Profiles were typically made down to 350 m at a speed of 25-30 cm s^{-1}.

4.2.2 *Microstructure Processing*

The dissipation rate of thermal variance, χ, is estimated through spectral analysis of temperature gradient segments recorded by the FP07s, where

$$\chi = 2k_t < 3(\partial T'/\partial z)^2 > \quad , \quad (4.1)$$

and k_t = 1.4 x 10^{-7} m^2s^{-1}, the molecular thermal diffusivity. Spectral analysis was performed on 4-s segments of data, roughly 1-1.2 m, using Welch's modified periodogram. Segments were detrended and then windowed using a Hanning window. Following *Ruddick et al.* [2000] and *Guthrie et al.* [2015], $(\partial T'/\partial z)^2$ in (4.1), temperature gradient variance, is obtained by integrating the temperature gradient spectrum out to a cutoff wavenumber where instrument noise begins to dominate the signal. A noise spectrum was established by averaging low energy (lowest fifth percentile) sections of profiles. The cutoff wavenumber is chosen as the highest wavenumber where the value of the temperature gradient spectrum was 1.5 times higher than the value of the noise spectrum. Assuming full isotropy results in the factor of 3 presented in (4.1). Although it is unclear if this assumption is valid in a low energy regime like the Amundsen Basin, we conservatively include it in our calculations in both 2013 and 2014 so a direct comparison can be made.

Vertical eddy thermal diffusivity is calculated using the Osborn-Cox (OC) relation,

$$K_T = \frac{\chi}{2<\frac{\partial T}{\partial z}>^2}. \qquad (4.2)$$

We then calculate turbulent heat fluxes using Fickian diffusion, $F_H = -\rho c_p K_t \frac{\partial T}{\partial z}$. Direct comparisons of K_T in 2013 and 2014 can only be made in the "smooth" sections of profiles, e.g. depth ranges where no thermohaline staircase is present as the Osborn-Cox relation assumes that χ results from overturns acting against a mean gradient [*Osborn and Cox*, 1972]. This limits the comparison of (4.2) using OC to a range of 50-120 m between the two surveys. We use this depth range because it covers the region from the depth of the deepest mixed layers encountered during 2014 to the shallowest thermohaline staircase appearance in 2013. The details of microstructure processing during NPEO 2007 and NPEO 2008 are outlined in detail in *Fer* [2009], *Fer* [2014], and *Sirevaag and Fer* [2012]. K_T will be calculated down to 200 m in the NPEO 2007, 2008 and 2014 data sets, since there is no staircase above this depth.

4.3 RESULTS

4.3.1 *Hydrography and Density Ratio*

Overall, the large-scale vertical T and S characteristics of the 2013 and 2014 profiles are similar and typical of the Amundsen Basin. Representative T and S profiles from each drift are shown in Figure 4.2. The profiles are most different in the upper ocean, due in large part to fresher, surface waters in 2013 compared to 2014. Average surface salinity was 31 in 2013 and 33 in 2014. This has a profound impact on the strength of the stratification in the upper part of the water column. Average Mixed Layer Depth (MLD) was calculated as the depth at which $\Delta\rho$ > 0.1 kgm^{-3} relative to the uppermost measurement. Average MLD was 22 m in 2013 and 33 m

in 2014. Similarly, buoyancy frequency, $N^2 = -\frac{g}{\rho_0}\frac{\partial \rho}{\partial z}$, measured from the base of the mixed layer down to 120 m is quite different between the years. N^2 in 2013 was 3 x 10^{-4} s^{-1} three times as strong as N^2 equal to 1 x 10^{-4} s^{-1}in 2014. We believe that these changes were a result of large-scale circulation changes in the Arctic Ocean, in particular the orientation of the transpolar drift. The results of this article in connection with large-scale circulation will be discussed more in Section 4.4.4.

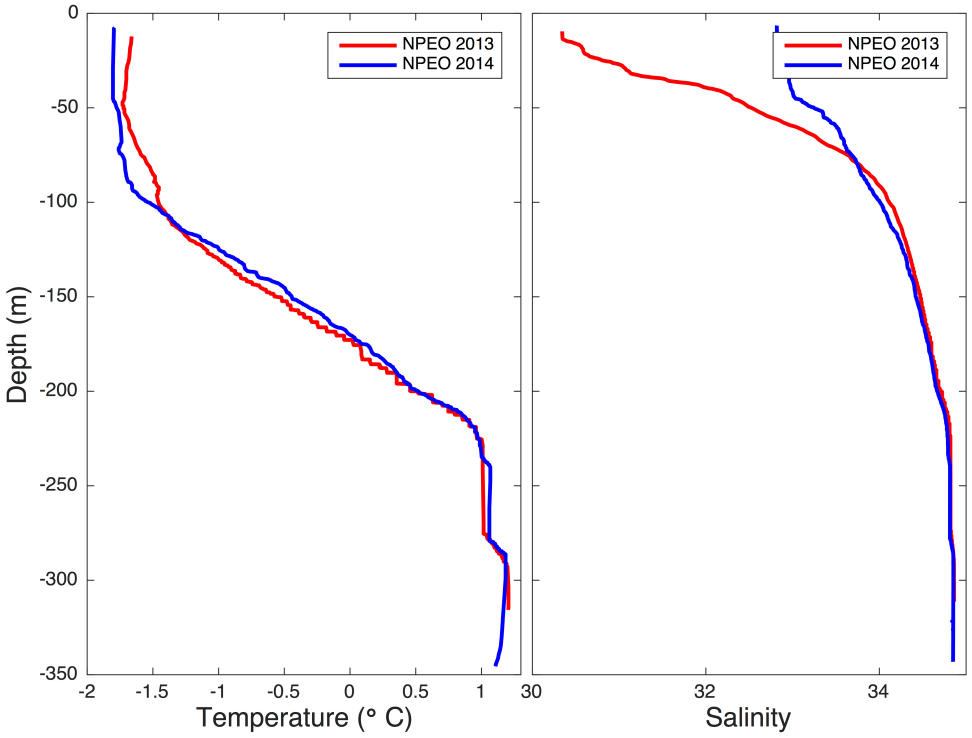

Figure 4.2. T and S Profiles from NPEO 2013 and 2014. Note the presence of a thermohaline staircase starting at 150 m in the NPEO 2013 Temperature profile. Below 100 m, large-scale T and S gradients are indistinguishable.

Below 100 m, large-scale vertical gradients of T and S are very similar. However, differences in the nature of the profiles start to emerge at 120 m depth. Below this range the 2013 profile has an extensive thermohaline staircase characterized by homogeneous mixed layers and sharp interfaces in T and S. A staircase is sometimes apparent in the 2014 data but typically

starts further down the water column, around 200 m. On average, the first identifiable interface occurs at 143 m depth in 2013 and at 217 m depth in 2014, indicating that substantially more of the DC-favorable stratification possessed a thermohaline staircase in 2013 when compared to 2014.

Density ratio, R_ρ, is often used as a marker for the susceptibility of the water column to double diffusion. The 10-m binned values of R_ρ for 2013 and 2014 from 140-220 m are shown in Figure 4.3. The red horizontal line in the box plot marks the median for all casts at that depth range. The two plots are virtually indistinguishable from one another although more variability is present in 2013 compared to 2014. Survey averaged between 150-200 m, we actually see higher R_ρ in 2013 compared to 2014, 3.8 versus 3.6, even though the lower R_ρ would suggest that staircase formation should be likelier in 2014. A similarly counterintuitive comparison applies to the Canada Basin where thermohaline staircases have been observed by Ice-Tethered Profilers and shipborne CTD measurements for much higher values of the density ratio. For example, Fig. 3 in *Timmermans* et al. [2008] shows the presence of thermohaline staircases for $3.5 < R_\rho < 7$. Most values reported in the "no staircase" regime in NPEO 2014 for depth ranges shown in Fig. 4.3 are in the lower end of that R_ρ range or even below it, suggesting that the small differences in R_ρ between NPEO 2013 and 2014 are unlikely to be the cause of the absence of a staircase in the 2014 observations.

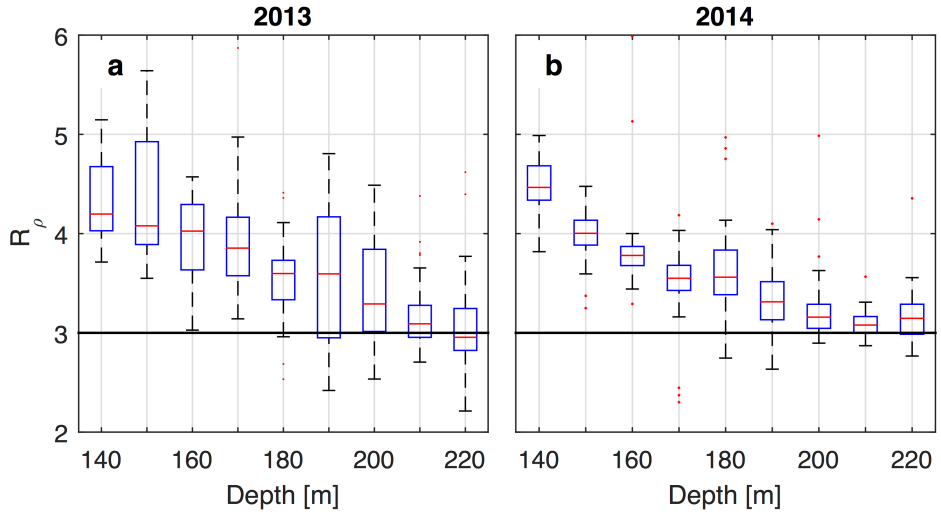

Figure 4.3. Box and Whisker plot showing survey-averaged 10-m binned R_ρ from 140 – 220 m. The red dashed line shows the median value, while the blue edges of the box show the 25th and 75th percentile values. The error bars show the highest and lowest values.

4.3.2 *Mixing*

Survey averaged 5-m binned vertical profiles of χ are shown in Fig. 4.4. Error bars are the 95th percentile confidence intervals based on the maximum likelihood estimator for a lognormal distribution. Only values from 50 to 120 m are reported, as 50 m is roughly the value of the deepest mixed layer in the drifts and 120 m marks the depth range at which the thermohaline staircase begins in the 2013 data. In 2014, χ is elevated above the 2013 values at every depth in this range, sometimes by more than an order of magnitude. Depth and survey averaged χ are as follows with 95th percentile ranges given in the brackets: χ_{13}= 2.4 x 10^{-10} °C^{2}s^{-1} [1.4 x 10^{-10} to 4 x 10^{-10}], χ_{14}= 1.8 x 10^{-9} °C^{2}s^{-1} [8.7 x 10^{-10} to 3.7 x 10^{-9}]. The reported 2013 values are quite low but still two orders of magnitude greater than the estimated noise floor of the measurements, 10^{-12}. These results suggest substantially more turbulence in these depth

ranges in 2014 compared to 2013. An examination of all the calculated χ values confirms this. Histograms of individual χ values estimated from each 4-s segment of data spanning all profiles between 50 – 120 m are shown in Fig. 4.5. A 2-sided Kolmogorov-Smirnov test indicates that these distributions are statistically different at a 99.9% confidence level. The distributions also adequately characterize the higher likelihood for turbulence in 2014 as well as significantly more energetic turbulence.

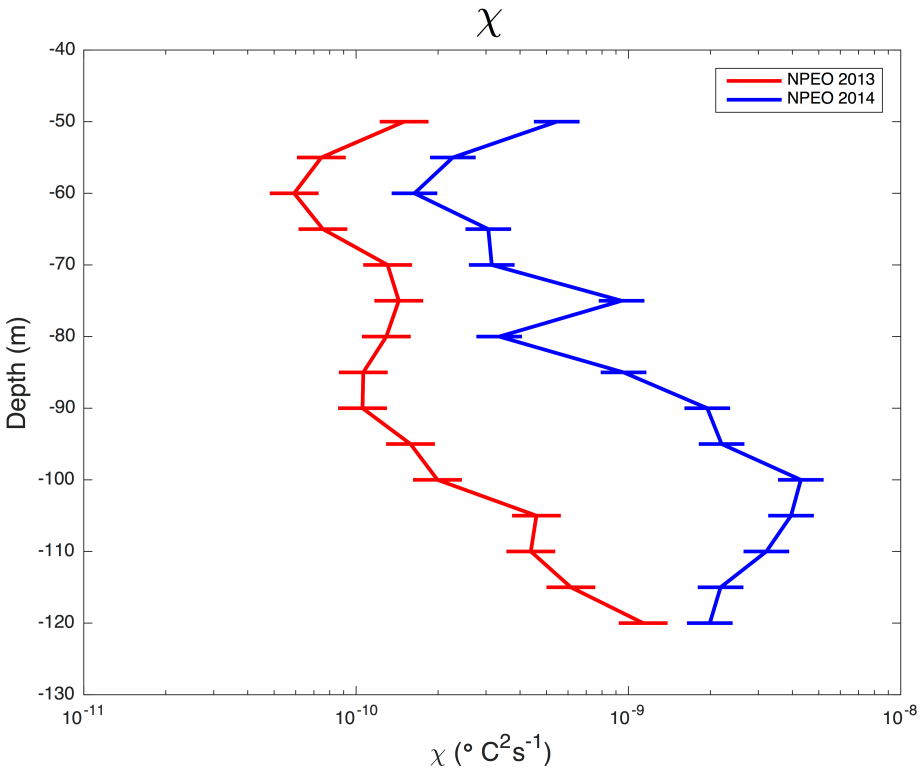

Figure 4.4. Survey averaged χ values shown in 5-m bins for NPEO 2013 and 2014. Error bars show the 95th percentile confidence interval based on the maximum likelihood estimator of a lognormal distribution.

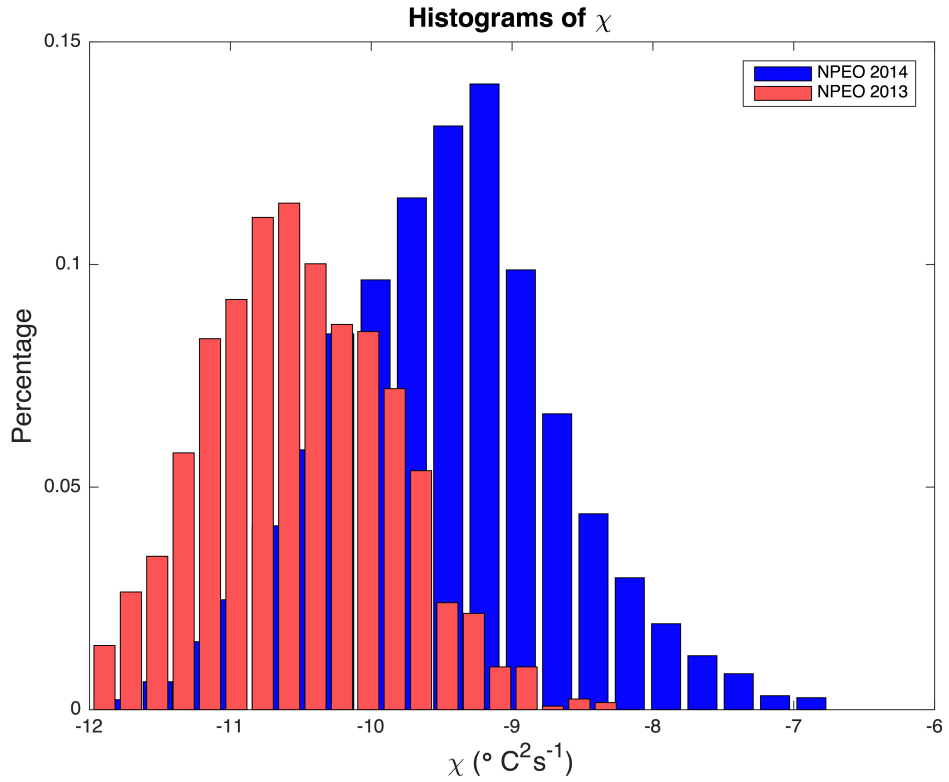

Figure 4.5. Histograms of χ for NPEO 2013 and 2014. These are all individual values of χ calculated between 50 – 120 m. Values are calculated based on 4-s (1 – 1.2 m) segments of temperature gradient data.

Survey averaged 5-m binned profiles of K_T calculated from (4.2) are shown in Fig. 4.6. To arrive at these values, χ is calculated as described in the previous section. The temperature gradient, $\frac{\partial T}{\partial z}$, is calculated based on a first-order polynomial fit to a high resolution vertical profile of temperature from the MR. This fit is made over the same bin segment as χ for each individual profile. Individual profiles of 5-m binned K_T are created for each cast and then survey averaged with error bars given as described in the above section. Turbulent diffusivity values between the two surveys are made more pronounced by the compounding effect of weaker turbulence, χ, and stronger stratification, N^2, in 2013 compared to 2014. Even though the relation for K_T, (4.2), does not rely on density stratification directly, the effect of the stronger

stratification on K_T in 2013 is apparent since $\frac{\partial T}{\partial z}$ is identical between the two surveys in this depth range, averaging 0.011 °C m^{-1} in both years. Values of K_T in 2013 are consistently low, with the highest value approaching 4 x 10^{-6} m^2s^{-1}. Below 60 m, most of the values in 2013 are less than 10^{-6} m^2s^{-1}, averaging 7 x 10^{-7} m^2s^{-1}. The reported values assume fully isotropic turbulence, which is most likely not valid. If isotropy is neglected, K_T in 2013 below 60 m is equal to 2.3 x 10^{-7} m^2s^{-1}, barely 1.5 times the molecular value. These reported values would be among the lowest ever measured by microstructure in the Ocean. The values of K_T in 2014 are significantly higher, averaging 1.8 x 10^{-5} m^2s^{-1} from 50 – 120 m and 2.3 x 10^{-6} m^2s^{-1} from 120 – 200 m. The upper values are roughly the same order of magnitude as typical mixing rates in the open ocean mid-latitude thermocline [*Gregg*, 1987] while the lower values are the same order of magnitude that's been reported in prior observations as well as used by numerical modelers [*Guthrie et al.*, 2013; *Zhang and Steele*, 1997].

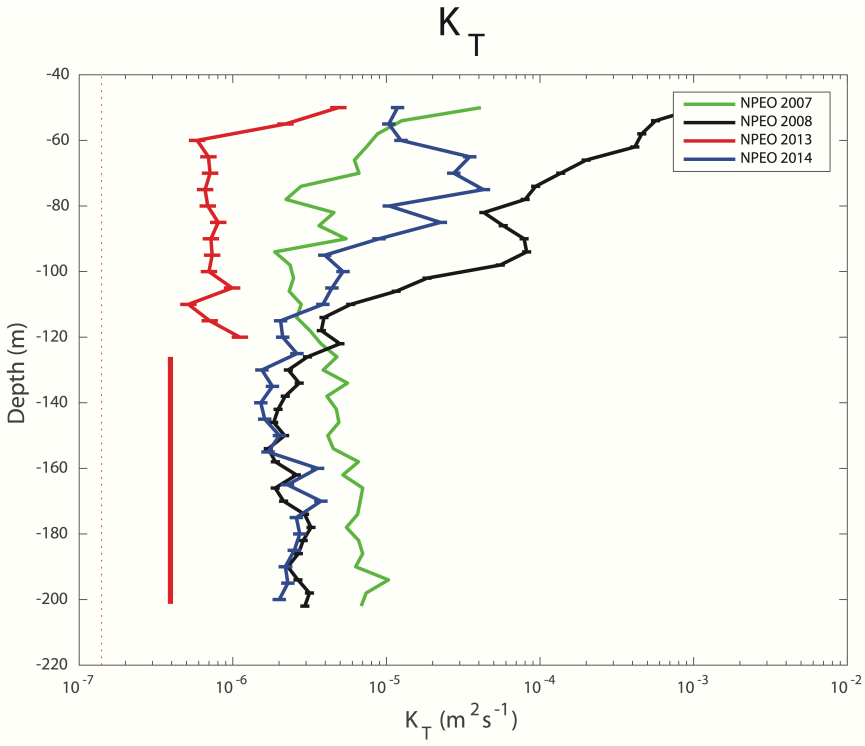

Figure 4.6. Survey-averaged K_T profiles in 5-m bins for NPEO 2007, 2008, 2013 and 2014. Error bars show the 95th percentile confidence interval based on the maximum likelihood estimator of a lognormal distribution. Please note that the NPEO 2007 profile is actually K_{ρ}.

Unfortunately, the presence of the staircase inhibits our ability to calculate K_T below 120 m using (4.2) in 2013 by obfuscating the meaning of χ, preventing a direct comparison between the two surveys below 120 m. If we assume that the true turbulent χ_{13} between 120 – 200 m is the same as it is between 50 – 120 m, we can make an estimate of K_T over the depth range by using background average $\frac{\partial T}{\partial z}$. This gives a value of 4 x 10^{-7} m^2s^{-1}, only roughly three times higher than molecular diffusion alone and an order of magnitude lower than the 2014 values calculated using (4.2). Because of the limited capacity for our measurements to yield K_T in the staircase region, the extrapolation of upper ocean χ to the staircase depth range in the 2013 data represents our best estimate of eddy diffusivity in the staircase, and it is hard to think of a reason

why χ should increase with depth in a region without freely propagating internal tides and weak flow overall. *Rainville and Winsor* [2008] noted elevated mixing above the Lomonosov Ridge during a survey in 2005, but this effect was confined to the region directly above the bottom (within 400 m) and not apparent whatsoever in the upper ocean. Similarly, near-inertial internal wave energy tends to decay with depth [*Alford et al.*, 2012; *Martini et al.*, 2014]. Therefore, if we assume that all turbulent fluctuations of temperature between 50 – 120 m are due to internal wave activity, then the depth range below should have even smaller χ, establishing $K_T = 4 \times 10^{-7}$ m^2s^{-1} as an upper bound on the background turbulent diffusivity in the staircase depth region in 2013.

Of the possible parameters likely to influence the presence or absence of a thermohaline staircase: location, hydrography, density ratio and background mixing, only calculated mixing values, K_T, are significantly different enough between the two surveys to warrant discussion of it being the cause. To strengthen this argument, we present microstructure data collected during NPEO 2007 and 2008 and previously reported in *Fer* [2009], *Fer* [2014], and *Sirevaag and Fer* [2012]. Representative temperature profiles from each of the drifts are shown in Fig. 4.7 to highlight the anomalous thermohaline staircase present during NPEO 2013. The NPEO 2007 data consists of 100 profiles made in a location in between NPEO 2008 and NPEO 2013. Rather than K_T, we report K_ρ values from shear microstructure measurements from NPEO 2007. The NPEO 2008 data consists of 169 profiles collected in a location similar to NPEO 2014 as well as a single profile, referred to as LR3, made near the Amundsen Basin side of the Lomonosov Ridge in a location similar to NPEO 2013. The NPEO 2007 and 2008 data are similar to NPEO 2014 in that a thermohaline staircase begins at roughly 200 m depth. NPEO 2007 was characterized by a strong near-inertial mixing signal reported in *Fer* [2014] and the 120 – 200 m

mixing values are the highest reported in any of the four surveys. Between 50 – 120 m, K_ρ = 6.5 x 10^{-6} m^2s^{-1} and between 120 – 200 m, K_ρ = 5.9 x 10^{-6} m^2s^{-1}. For NPEO 2008, between 50 – 120 m, K_T = 1.9 x 10^{-4} [1.2 x 10^{-4} 3 x 10^{-4}] m^2s^{-1} and between 120 – 200 m, K_T = 2.6 x 10^{-6} [2.1 x 10^{-6} 3 x 10^{-6}] m^2s^{-1}. The NPEO 2007 and 2008 values suggest significantly higher mixing in these years compared to 2013. Below 120 m, mixing values in 2008 are nearly identical to those found in 2014, but from 150 – 200 m, survey averaged R_ρ = 4 in 2008, a value that coincides with the presence of a staircase in the Canada Basin [*Timmermans et al.*, 2008]. The single profile made at LR3, which contained no evidence of a thermohaline staircase at any depth range, displays similarly high mixing values. Between 50 – 120 m, K_T = 2.2 x 10^{-5} m^2s^{-1} and between 120 – 200 m, K_T = 3.2 x 10^{-6} m^2s^{-1}. For the lower depth range, R_ρ = 3.6 at LR3, even lower than the averaged NPEO 2008 value.

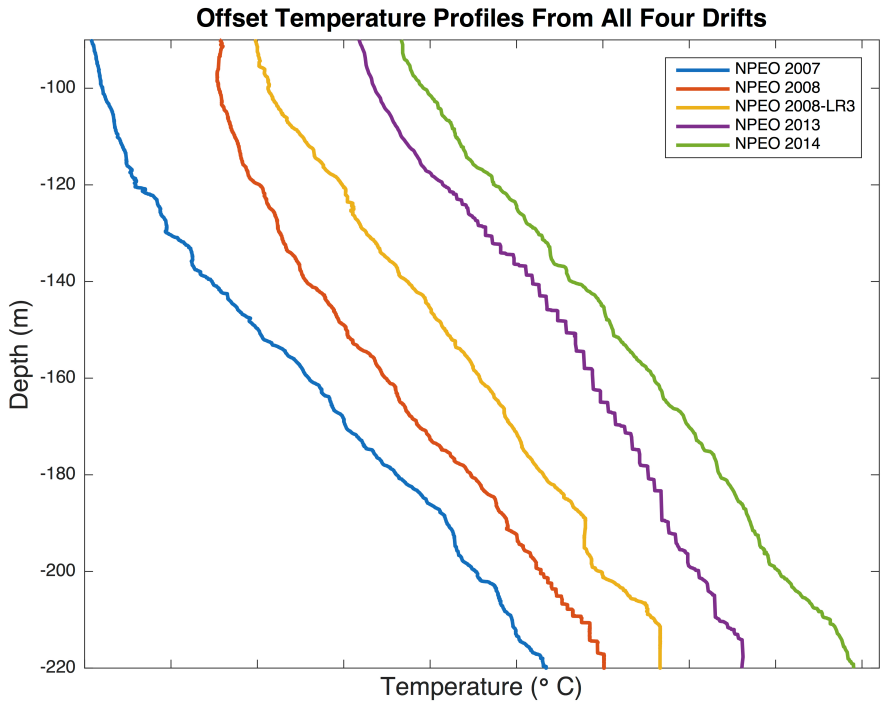

Figure 4.7. Waterfall plot of temperature profiles from all four drifts plus station LR3 during NPEO 2008. Data shown is from FP07 thermistors. Temperature has been offset from 0.5 to 2 °C to highlight the differences in the profiles. Note the extensive staircase up to 120 m present only during NPEO 2013. NPEO 2008 shows a staircase beginning at 200 m while no staircase is visible in the NPEO 2014, NPEO 2007 or LR3 profiles.

These results suggest a lower bound of 2-3 x 10^{-6} m^2s^{-1} for the background diffusivity necessary to disrupt DC thermohaline staircase formation for $3 < R_\rho < 4$ for the area and time periods covered in the survey. The results are consistent between the NPEO 2007, 2008 and 2014 surveys, indicating even weak mixing, O(10^{-6}) m^2s^{-1}, compared to typical oceanic values can prevent the staircase from forming. These low levels of mixing are consistent with a direct numerical simulation performed in *Radko et al.* [2014] for the Salt Fingering regime. The maximum K_T allowing for thermohaline staircase formation in the DC case remains to be explored in numerical simulations.

4.3.3 *Heat Flux*

Vertical profiles of survey averaged turbulent heat fluxes are shown in Fig. 4.8. Between 50 – 120 m, including the Cold Halocline portion of the water column, there is a marked difference between the two years. Heat fluxes are negligible in 2013 in this depth range, indicating very little vertical heat transfer from the AW layer into the mixed layer. In contrast, heat fluxes throughout this depth range were measurable in 2014, and as high as 0.6 Wm^{-2}, but averaging 0.4 Wm^{-2}. Individual values corresponding to turbulent patches could reach values > 1 Wm^{-2} at times in 2014.

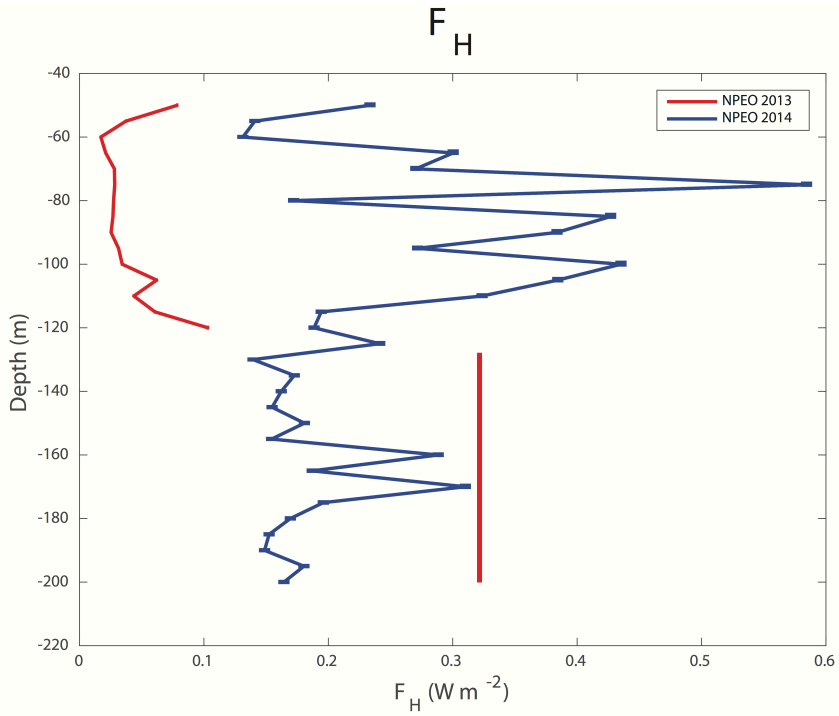

Figure 4.8. Survey-averaged F_H profiles in 5-m bins for NPEO 2013 and 2014. Error bars show the 95th percentile confidence interval based on the maximum likelihood estimator of a lognormal distribution. For reference, the double diffusive heat fluxes during NPEO 2013 in the staircase depth range (120 – 200 m) are 0.33 Wm^{-2} and shown by the vertical red line.

Double diffusive heat fluxes below 120 m during 2013 were previously reported in *Guthrie et al.* [2015] and averaged 0.33 Wm^{-2}. The survey averaged turbulent heat fluxes measured in 2014 below 120 m using (4.2) and Fickian diffusion were 0.2 Wm^{-2}. Two recent studies have reported enhanced χ compared to ε, the turbulent dissipation of kinetic energy, in areas with stratification favorable to double diffusion [*Merrifield and St. Laurent*, 2015; *Nagai et al.*, 2015]. The heat flux results from NPEO 2014 most likely represent a combination of turbulence and double diffusion.

It may seem surprising that heat fluxes in 2014 are nearly the same and even slightly lower when compared to the double heat diffusive fluxes through the thermohaline staircase in 2013. However, previous results have shown that shear and turbulence can decrease double diffusive heat and salt fluxes [*Radko et al.*, 2015]. This is arguably due to the contrasting nature of salt (or mass) transport relative to heat transport in the two processes. When turbulent mixing prevails, salt (mass) and heat transport are down gradient and with the same turbulent diffusion coefficient. In contrast, the double diffusive process selectively transports heat. Water at the top of a convective layer becomes denser due to thermal contraction and water at the bottom of the layer less dense due to thermal expansion. This produces cellular convection that feeds molecular heat flux, but almost no salt flux, across the diffusive interfaces between layers. Therefore, mixing of heat up the DC staircase occurs with minimal change in total potential energy of the staircase and is thus very efficient relative mixing of salt (mass). It is easy to imagine that input of greater mechanical energy into turbulent mixing would breakdown the mass distribution characteristic of DC mixing and essentially shut it down while producing turbulent diffusion of heat consistent with the turbulent diffusion of salt but less than the thermal diffusion of the DC process that was destroyed.

It is important that despite the different mixing regimes, the heat fluxes remain low and in line with previous Arctic Ocean estimates in either case as these heat fluxes are only roughly $1/4^{th}$ to $1/3^{rd}$ of the 1 Wm^{-2} imbalance necessary to account for recent sea ice volume reductions [*Kwok and Untersteiner*, 2011]. Also, the similarity of the F_H values in 2013 and 2014 coupled with the fact that the 2013 thermohaline staircase and other reported staircases in the Amundsen Basin are most likely not in steady state [*Guthrie et al.*, 2015; *Sirevaag and Fer*, 2012] suggests that this section of the water column in the Amundsen Basin is often right on the cusp of staircase formation such that the appearance of the staircase depends on only slight modulations of background mixing.

The mismatch between the 50 – 120 m F_H and the double diffusive heat fluxes below 120 m in the 2013 data suggest the occurrence of heat flux divergence in the water column directly above the top of the thermohaline staircase. A section of a vertical temperature profile from a single cast made during NPEO 2013 is shown in Fig. 4.9. A feature possibly formed by this heat flux divergence is apparent from 140 – 150 m. This section of the profile resembles a "heat bubble" with very little expression apparent in the salinity profile. There is no known water mass that occupies this depth range in the Amundsen Basin and similar features are not seen in the NPEO 2014 data set. While the feature is not apparent in a survey-averaged temperature profile, the "bubbles" appear in nearly half of the profiles made during NPEO 2013. While their depth varies between 120 and 150 m, they are always found just above the top of the thermohaline staircase. Heat content is calculated as $HC = \rho c_p \int_{z2}^{z1} (T - T_{fit})$, where T_{fit} is the assumed original profile created by linearly interpolating the points on either side of the "bubble". For this feature, HC = 4 x 10^6 Jm^{-2}. Assuming an imbalance of roughly 0.3 Wm^{-2} based on negligible heat fluxes above this feature, this suggests a timescale of 150 days for the feature to form.

Recent 3-D numerical simulations suggest that double diffusive heat fluxes are often an order of magnitude higher during the initial stages of staircase formation when compared to the heat fluxes maintained upon reaching equilibrium, so it's possible that our timescale estimate could be biased high. It's unclear if this phenomenon is important to basin-scale heat budgets in the Arctic Ocean as they have not been reported nor suggested before to our knowledge. They most likely only occur during extended periods of weaker than normal vertical mixing in the Eurasian Basin, where double diffusive heat fluxes are likely to be higher than in the Canada Basin due to larger temperature gradients and lower density ratios. Assuming somehow that all this "extra" heat was able to reach the Mixed Layer instantaneously, we can use the following equation to calculate basal sea ice melt:

$$\Delta h_I = \frac{HC}{\rho_I L_I} \qquad (4.3)$$

where Δh_I, ρ_I, and L_I are the change in ice thickness, the density of ice (900 kgm^{-3}) and the latent heat of fusion of sea ice (3 x 10^5 $kg\ J^{-1}$), respectively. This suggests an estimated ice melt of 1.5 cm, showing that even in the unlikely case that all of this heat were able to affect the bottom of the ice, it's unlikely to affect surface heat budgets in any meaningful way compared to variables like incoming solar radiation.

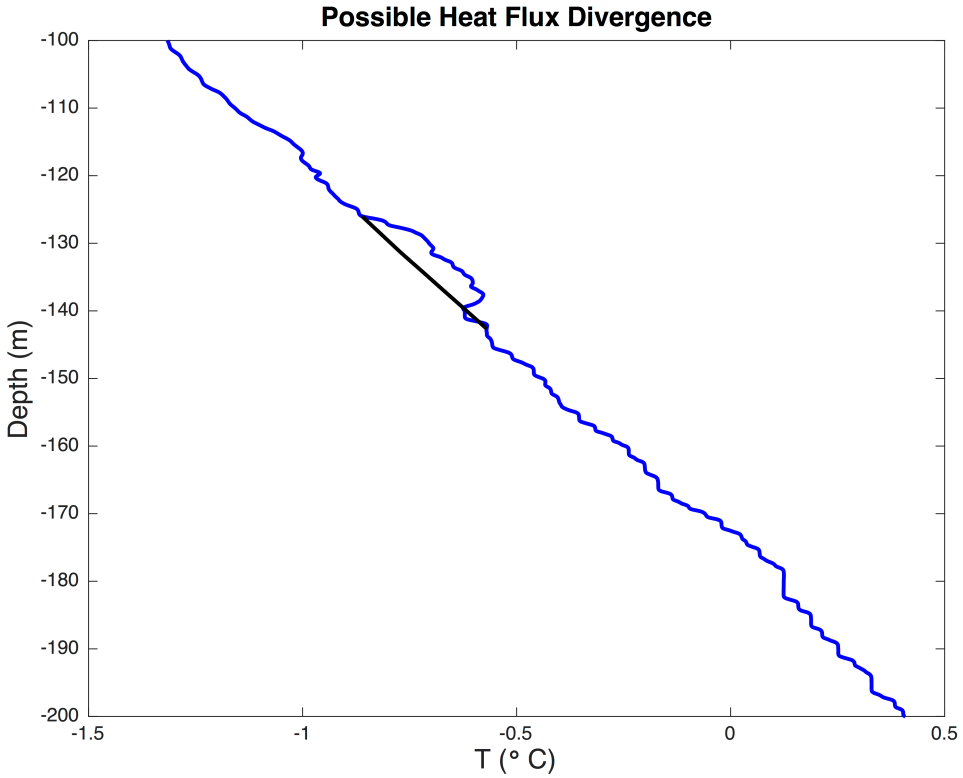

Figure 4.9. The blue line shows Depth vs. Temperature from Cast #22 during NPEO 2013. Heat fluxes were negligible above 120 m during this survey. Staircase-averaged heat fluxes were 0.33 Wm^{-2}. Note the "bubble" from 130 m and 140 m, possibly resulting from heat flux divergence. The black line is a simple linear fit to the points on either side of the "bubble" and is used to calculate Heat Content.

4.4 DISCUSSION

4.4.1 *Possible Dynamical Clues*

Analysis of ERA-interim reanalysis winds revealed no significant differences in wind speed between January-April 2013 and January-April 2014. Similarly, the International Arctic Buoy Program (IABP) deployed Polar Area Weather Stations at NPEO 2013 and 2014 (http://iabp.apl.washington.edu). The wind speed records between 2013 and 2014 during the

duration of the measurement periods were markedly similar as well (not shown). However, there are differences in the nature of the sea ice drift velocity between the two years.

We use measurements of ice velocity to examine the forcing behind the increased mixing found in 2014. Fifteen minute GPS data is available via a nearby Ice-T buoy deployed by colleagues at L'Ocean of the University of Pierre and Marie Cure. Description of the buoy, GPS data acquisition and processing can be found in *Vivier et al.* [2016]. Ice velocity can be determined from differencing the GPS position. The complex demodulation method presented in *McPhee* [2008] allows the separation of ice velocity into clockwise, counterclockwise, semidiurnal (inertial) and diurnal velocities. The generation of near-inertial internal gravity waves is believed to be governed by clockwise inertial oscillations in the mixed layer [*D'Asaro,* 1989*; Alford,* 2012]. Previous observations in the Arctic have found clockwise velocities at the inertial frequency to be typically the same in the sea ice and in the mixed layer [*Martini et al.*, 2014; *McPhee,* 1986]. Maximum clockwise inertial ice velocities are relatively small in both drifts, reaching 4 cm s^{-1} in 2014 and 1 cm s^{-1} in 2013 (not shown). Similarly, GPS data collected during NPEO 2007 and 2008 also show maximum clockwise inertial ice velocities of roughly 4 cms^{-1}. While none of these values are particularly large when compared to mixed layer currents forced by storms in the mid-latitude ocean, the difference is suggestive of as much as a factor of sixteen enhancement of near-inertial internal wave energy in 2014 relative to 2013. The value presented in 2014 is quite similar to the mean inertial ice velocity value of 5 cms^{-1} presented for summertime Beaufort Sea Ice-Tethered Profiler data presented in *Dosser and Rainville* [2015]. Their ice velocity results were also presented with an accompanying increase in near-inertial internal wave amplitude down to 200 m.

In 2013 and 2014, a total of five XCPs were deployed through the same hydro-hole utilized by the MR/CTD combination during breaks in profiling. These XCPs are used to examine differences in internal wave shear between the two surveys. 2 XCPs were deployed in 2013 and 3 XCPs were deployed in 2014. All reported values are survey averaged between the two years to give slightly better confidence intervals. *U* and *V* velocity spectra are calculated between 100-200 m and then added together. The resulting velocity spectra are multiplied by $(2\pi k_z)^2$, where k_z is the vertical wavenumber, to create vertical shear spectra. Shear spectra are integrated out to 0.1 cpm, equivalent to a 10-m vertical wavelength, to calculate shear variance. The full processing scheme is identical to the XCP processing and shear calculations described in *Guthrie et al.* [2013]. Between 100-200 m, shear variance in 2014 was nearly twice as high as in 2013. Unfortunately, due to the limited degrees of freedom resulting from the small number of profiles, we are unable to claim statistical significance at the 95% confidence interval. Using the finescale parameterization to calculate K_ρ employed in *Guthrie et al.* [2013] reveals K_ρ = 2.4 x 10^{-6} m^2s^{-1} in 2014 and K_ρ = 7 x 10^{-7} m^2s^{-1} in 2013. The 2014 K_ρ is similar to the K_T reported from temperature microstructure in this same depth range. These differences are not as high as the reported differences in χ between 50 – 120 m from the temperature microstructure, and the reported parameterized XCP mixing values are still small in 2014. This suggests the ability of even small increases in shear and background mixing to disrupt staircase formation.

4.4.2 *Connections to Basin-Scale Circulation*

A considerable shift in the location of the Transpolar Drift, a defining circulation feature in the Arctic Ocean, occurred between 2013 and 2014. *Morison et al.* [2014] propose that the shift is the result of changes in the atmospheric circulation as determined by the Arctic

Oscillation Index [*Thompson and Wallace,* 1998]. The winter (NDJFMA) AO in 2013 was highly negative, with an index of -0.6. In contrast, the winter AO in 2014 was highly positive with an index of 1.3. Contour plots of salinity from the NPEO airborne hydrography in 2013 and 2014 are shown in Fig. 4.10. In 2014, the core of the Transpolar Drift and the front between fresher Pacific-derived water and saltier Atlantic-derived water are shifted towards the Canadian Archipelago along the 90 W longitudinal line. This results in higher surface salinity at our 2014 NPEO measurement site as surface waters at the drift location become Atlantic-derived. The opposite occurred in 2013 with the Transpolar Drift spread into East longitudes and centered almost directly over the North Pole, very close to the location of the 2013 NPEO ice camp. As discussed in section 4.3.1, these surface changes result in upper ocean stratification three times as strong in 2013 compared to 2014. As shown in section 4.3.2, this has profound impacts on the intensity of the mixing in the upper 100 m. Both NPEO 2007 and 2008 have similar mixed layer salinities as NPEO 2014 and also occur during years with positive AO index values. The particularly weak values of upper-ocean turbulence measured during NPEO 2013 likely arise as a direct consequence of the enhanced stratification near the North Pole in the Amundsen Basin that spring. It is possible that these large-scale circulation changes could have profound impacts on the vertical fluxes of heat in the central Amundsen Basin given the contrasting nature of the mixing regime encountered in 2013 compared to the other surveys.

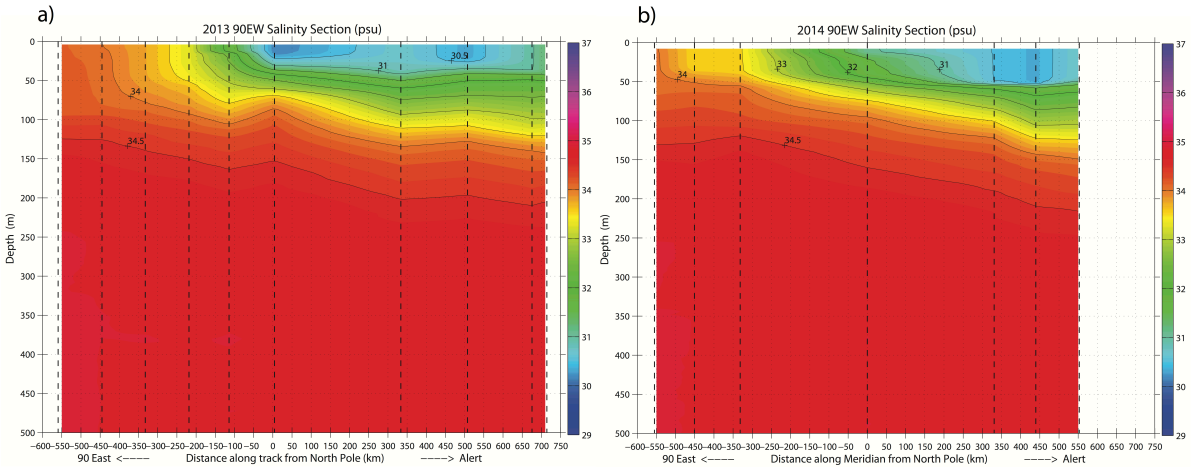

Figure 4.10. (a) Depth-Latitude contour plot of Salinity from 90 East down 90 W for NPEO 2013. (b) Depth-Latitude contour plot of Salinity from 90 East down 90 W for NPEO 2014. Data is from NPEO airborne hydrography stations. Note the position of the front between Pacific-derived and Atlantic-derived waters located almost directly at the North Pole in 2013. This same salinity front has shifted almost 450 km towards the Canadian Arctic Archipelago in 2014, leading to the surface stratification differences between the two surveys.

Stratification directly inhibits turbulence, but could also play a pivotal role in the dynamics associated with the internal wavefield, primarily through the under-ice dissipation mechanism outlined in *Morison et al.* [1985]. Larger mixed layer depths have also been shown to enhance internal wave energy, particularly near-inertial waves [*Gill*, 1984]. Survey averaged mixed layer depths are 10 m deeper in 2014 compared to 2013, but it's unclear whether a difference of this magnitude is able to significantly affect the strength of the internal wavefield.

4.5 CONCLUSIONS

We have presented results from four microstructure surveys made in the Amundsen Basin of the Arctic Ocean from 2007 through 2014. A thermohaline staircase, indicative of the diffusive convective form of double diffusion, was present at differing depth ranges in at least three of the four surveys. Even though the surveys were all made in April and located within a

200 km radius of one another, variability in surface salinity and the intensity of upper-ocean mixing was substantial particularly in 2013 when compared to the other three sets of measurements. Based on analysis of the hydrography, location, large-scale density ratio and turbulent diffusivity of heat between the four surveys, it appears that exceptionally weak mixing, even for the normally quiescent Arctic Ocean, is responsible for the extensive thermohaline staircase present during NPEO 2013. It is plausible that this weak background mixing in 2013 was forced by an increase in near-surface stratification resulting from large-scale circulation changes and this resulted in the formation of a thermohaline staircase at depths where they are not commonly reported, e.g. 120 – 200 m.

Upward vertical heat fluxes from the Atlantic Water layer were consistent between NPEO 2013 and 2014 despite double diffusion being the dominant mixing mechanism in 2013 and turbulence being the dominant mixing mechanism in 2014. The similarity in heat fluxes from 120 – 200 m suggest that this region of the Amundsen Basin is usually on the cusp of thermohaline staircase formation and average background turbulence would have to increase by a sustained factor of 2 to result in any meaningful long-term changes in heat flux. In the region above the staircase, however, the nature of the heat fluxes between these two surveys in the 50 – 120 m depth range were quite different with substantial survey-averaged heat fluxes through the cold halocline, 0.4 Wm^{-2}, in 2014 compared to negligible heat fluxes through the same range in 2013. This likely resulted in heat flux divergence in 2013 heating the area immediately above the thermohaline staircase. Such a feature was present in half the profiles made during that survey, but these features are likely unimportant in basin-scale considerations.

While the heat flux from the Atlantic Water layer varied little between the surveys, it is possible that the large-scale circulation differences could play a pivotal role in modulating the

vertical heat flux through the cold halocline layer in the Amundsen Basin during winter and spring. It is unclear whether or not the cold halocline heat fluxes measured in 2014 are representative of averaged seasonal values as previous authors have reported no heat flux through the same layer [*Fer*, 2009]. If they are representative, then sustained heat fluxes of this magnitude from the cold halocline into the mixed layer could account for 2.3 cm of sea ice melt over a 6-month period. This suggests a process that is likely unimportant on annual timescales, but perhaps important interannually.

Chapter 5. CONCLUSION

This dissertation has focused on understanding background mixing in the Arctic Ocean and how it has changed with changing forcing and ice cover. We have examined shear measurements made over more than 30 years to determine the variation in internal wave energy and mixing in different regions of the Arctic Ocean. To improve estimates of thermal diffusivity and heat fluxes in the deep basins of the Arctic Ocean from the base of the mixed layer down to the Atlantic Water layer, we have presented results from three different data sets collected in the central Arctic Ocean as well as leveraging earlier microstructure observations. Spatial and temporal variations have been examined through the use of a diverse set of shear measurements made in the last thirty years. Using temperature microstructure, the regimes of turbulent mixing and double diffusion in the Amundsen Basin during spring have been explored. We have also provided an updated version of a well-known heat flux parameterization for double diffusion that agrees to within 10% of the observed values. Heat fluxes for each mixing regime have been compared and contrasted, and we have discussed the implications of different levels of

background turbulent diffusivity on thermohaline staircase formation. A concise summary of the chapters and possible future work follows below.

5.1 SUMMARY

5.1.1 *Revisiting Internal Waves and Mixing in the Arctic Ocean*

In the first chapter, emphasis was placed on basin-scale characteristics of turbulence and internal wave energy based on XCP and MMP data collected as part of NPEO airborne hydrography and moorings in the Beaufort Gyre deployed by the Beaufort Gyre Exploration Project. Overall, it appears that the internal wave field in the central Arctic Ocean remains weaker than at mid-latitudes, with values rarely approaching mid-latitude GM levels. However, there are geographical differences within the Arctic Ocean. Energy levels in the Canada Basin are lower than in the Amundsen Basin. This is surprising as sea ice losses have been most extensive in the western Arctic Ocean. We attribute these lower energy levels to an enhancement of the under-ice dissipation mechanism introduced in *Morison et al.* [1985] by the stronger near-surface stratification in the Canada Basin. Corresponding diffusivity values estimated through the finescale parameterization are also low, typically $O(10^{-6})$ m^2s^{-1} in the more stratified region of the water column down to 250-300 m, and show minimal temporal variability. Inferred diffusivity values from XCPs deployed during AIWEX are nearly identical to more recent estimates from the MMPs on the BGEP moorings, indicating very little change in the intervening thirty years. These results agree qualitatively with *Martini et al.* [2014], who used a year-long current meter time series on the Beaufort Sea continental slope and found internal wave energy levels roughly the same as AIWEX.

5.1.2 *Observational Validation of the Diffusive Convection flux laws in the Amundsen Basin, Arctic Ocean*

With internal wave driven mixing low, double diffusive convection is potentially the dominant mechanism of ocean heat flux from warm waters at depth to the surface layer and ice cover. In the second chapter, heat fluxes through a thermohaline staircase were quantified and shown to agree with the parameterized heat fluxes calculated from the 4/3rd laboratory flux law. We used temperature microstructure profiles collected during NPEO 2013 in the Amundsen Basin to achieve this. Vertical profiles revealed an extensive thermohaline staircase sometimes beginning at 120 m depth and extending down to 250 m. Heat fluxes through the thermohaline staircase were calculated in three ways: assuming purely molecular diffusion through the interface and the maximum measured interfacial temperature gradient, applying the Osborn-Cox relation in the homogeneous convecting layers and using the 4/3rd laboratory flux law. Previous flux law formulations underestimated heat fluxes compared to the microstructure observations. Using the first method allowed us to check the validity of the exponent in the laboratory flux law, using the following relationship, $Nu = Ra^{\eta}$, where η = 1/3rd typically. We found η = 0.30 to be a better fit to our data. This value is similar to the exponent suggested by a number of laboratory and numerical experiments, both for standard thermal convection and double diffusion. To our knowledge, this is the first time support for this value of η has been found through in-situ field measurements. Updating the flux law with this newly calculated exponent resulted in observed and parameterized heat fluxes agreeing within 10%, a significant improvement compared to prior observations. We also caution that the nature of the staircase in

the Amundsen Basin, e.g. thinner interfaces and thinner layers than the Canada Basin, could present challenges in analyzing staircase characteristics solely through CTD data.

5.1.3 *Thermohaline Staircases in the Amundsen Basin: possible disruption by shear and mixing*

The third chapter provided a synthesis of microstructure measurements made during NPEO 2007, 2008, 2013 and 2014. The results from NPEO 2013 and 2014 show substantial differences in the mixing between the two surveys. Survey-averaged K_T was 1.8 x 10^{-5} m^2s^{-1} in 2014 and 1 x 10^{-6} m^2s^{-1} in 2013 between 50-120 m. Histograms of χ reveal more energetic turbulence in 2014 as well. Between 120 and 200 m, a thermohaline staircase is present in 2013 but not in 2014, despite lower R_ρ in 2014. However, heat fluxes through this depth range are remarkably consistent between the two years, despite different dominant vertical heat transfer mechanisms. We argue that particularly weak mixing resulting from increased near-surface stratification was shown to allow staircase formation higher up in the water column during NPEO 2013. This result is consistent with the NPEO 2007 and 2008 surveys as well. An upper-bound on background mixing necessary, 2 x 10^{-6} m^2s^{-1}, to disrupt staircase formation for $3 < R_\rho < 4$ was proposed. The results from the third chapter are suggestive of the importance of surface stratification in determining the level of turbulence further down in the water column, something that could explain the differences between the Canada and Amundsen Basins discussed in Chapter 2.

5.1.4 *Atlantic Water heat flux discussion*

Results from all three chapters shows that vertical heat flux from the Atlantic Water layer is typically capped at a value of 0.2 – 0.3 Wm^{-2} in the deep parts of the Amundsen Basin, regardless of the dominant vertical heat transfer mechanism. Previous results calculating double diffusive heat fluxes in the Canada Basin provide a similar, albeit slightly smaller value, 0.05 – 0.22 Wm^{-2}, although this should be updated with the revised flux law parameterization presented in Chapter 3. Similar results through the use of the finescale parameterization utilized in Chapter 2 are reported in *Lique et al.* [2014]. These values are validated by a recent modeling study by *Nummelin et al.* [2014] that found a deep basin-averaged heat flux from the AW of 0.12 Wm^{-2} was sufficient to balance the advective heat flow of AW through Fram Strait. These results suggest that heat flux from the Atlantic Water layer is only important regionally in the Arctic Ocean, near the inflow regions and in areas where upwelling can advect it onto the shelves. A seminal paper by *Treshnikov* [1967] discussing AW heat fluxes appears especially prescient in hindsight, as the author reasonably predicted that the majority of heat lost from the AW occurred near the inflow regions and in the Nansen Basin.

5.1.5 *Future Work*

One important piece of future work involves verifying the large, 2-8 Wm^{-2}, heat fluxes reported by *Polyakov et al.* [2012]. The authors apply the *Kelley* [1990] formulation of the DC $4/3^{rd}$ flux law to a thermohaline staircase over the Atlantic Water core in the Laptev Sea. The nature of the staircase is quite different compared to ones previously discussed in the Arctic as it has much larger interfaces, O(1) m, and layers, O(10) m. It's unclear whether or not the $4/3^{rd}$ flux law is applicable to this type of staircase since no verification with microstructure has been

reported. Such large homogeneous layers are sometimes present in the center of the Amundsen and Canada Basins as well and are typically located directly above the AW temperature maximum. They appear to be closely related to a set of interleaving features that have been documented in the Arctic for nearly 30 years and are proposed to result from inflowing Fram Strait Branch Water interacting with existing colder Atlantic Water already present in the Arctic Ocean basin. It remains to be seen what forces these layers to be homogeneous, rather than intrusion-like. But it is possible that these are intrusions that for some reason become homogeneous and resemble a much larger thermohaline staircase. *Merryfield* [1999] finds a similar relationship in an analytical model for the Salt Fingering case, but there is no reason that a similar relationship wouldn't exist for the DC case as well. He found that intrusions began to resemble a thermohaline staircase similar to the one discussed by *Polyakov et al.* [2012] for low values of R_ρ and low values of background mixing rate, two things representative of the region of the *Polyakov et al.* [2012] staircase as well as the central Amundsen and Canada Basins.

Since AW heat only plays a minimal role in the ocean-sea ice budgets in the deep basin, more work should be done in investigating the role of Pacific Summer Water (PSW) in modulating sea ice concentration in the Canada Basin. PSW's close proximity to the mixed layer means the heat trapped within the layer could be susceptible to both direct entrainment and mixing by near-inertial waves. Little is known about the role of PSW heat in affecting the sea ice balance as results have provided different assessments in its importance. *Toole et al.* [2010] used data from an Ice-Tethered Profiler over the course of a winter in the central Canada Basin and found that entrainment was never strong enough to reach the PSW. Meanwhile, *Kawaguchi et al.* [2013] reported heat flux values of 1000 Wm^{-2} in the vicinity of Barrow Canyon during a microstructure survey made during Fall 2012.

An analogous situation exists in the Amundsen Basin as well in the Cold Halocline layer. By definition, the Cold Halocline contains less heat than the PSW layer. However, the mixing estimates made during NPEO 2013 and 2014 show a significant difference in the heat flux from this layer up to the surface, as high as 0.6 Wm^{-2} in 2014 compared to negligible heat fluxes in 2013. Unfortunately, the limited temporal duration of our measurements prevent us from quantifying the heat from this layer on longer timescales, e.g. over a season. Despite containing a small amount of heat, the layer also acts as a fundamental barrier between the AW and the mixed layer. In the presence of the CHL, entrainment only brings cold, salty water into the mixed layer rather than the warmer AW. A number of studies have shown the importance of this layer in preventing AW heat from reaching the bottom of the sea ice and the disappearance of this layer could substantially alter the nature of ocean-to-ice heat fluxes in the Amundsen Basin [*Steele and Boyd*, 1994; *Davis et al.*, 2015].

The results of this dissertation are suggestive of perpetual quiescence in the deep Amundsen and Canada Basins. A logical next step then would be to search for possible factors explaining the lethargy of the deep Arctic Ocean other than the presence of sea ice. If the results of *Munk and Wunsch* [1998] are to be believed and the wind and the tide are the primary drivers of mechanical energy input into the ocean, then we must start with them. Since tidal forces are expected to remain constant on human timescales, wind energy input in the form of near-inertial oscillations and internal waves should be the focus of the study. A pair of recent studies by *Dosser and Rainville* [2016] and *Martini et al.* [2014] have perhaps shown a very slight increase in near-inertial internal wave energy in the Canada Basin. But these increases have not been as large as hypothesized, especially given the nature of the catastrophic decline in sea ice extent over the past 30 years. The results of the dissertation have clearly demonstrated that the central

Arctic Ocean is still much less energetic than the mid-latitude ocean. We identify two possibly important parameters besides the presence of a sea ice cover below. β, the variation of the Coriolis frequency with latitude, has been shown to be a key parameter in diminishing the horizontal wavelength of near-inertial oscillations in the mixed layer set up by atmospheric storms to a smaller size that allows this energy to be transferred down into the pycnocline as internal waves [*D'Asaro et al.*, 1995]. At 75 °N, β is roughly one-third the magnitude it is at 45 °N, possibly resulting in less efficient kinetic energy propagation out of the pycnocline. Mixed layer depth also changes the partition of energy into vertical modes, as deeper mixed layers preferentially move a larger percentage of the available energy into the first few modes, the ones that are able to propagate furthest [*Zervakis and Levine*, 1995]. The surface Arctic Ocean is particularly stratified in the Summer and Fall, largely due to melting sea ice. However, these are the seasons with the loosest ice cover, which should enable the most efficient transfer of momentum from the atmosphere to the ocean, as internal ice stresses should be smallest. This could mean that atmospheric storms are only "locally" important as the shallow mixed layers imply that these low-mode near-inertial waves propagate out of the generation region with only a small percentage of the available energy. If this is true, then a paradox exists as the season that should have the most efficient transfer of momentum from the atmosphere into the ocean is actually limited by the stronger stratification from sea ice melt.

BIBLIOGRAPHY

Alford, M. H., M. F. Cronin and J. M. Klymak (2012), Annual Cycle and Depth Penetration of Wind-Generated Near-Inertial Internal Waves at Ocean Station Papa in the Northeast Pacific, *J. Phys. Oceanogr.*, ***42***, 889–909.

Batchelor, G.K., (1959), Small-scale variation of convected quantities like temperature in turbulent fluid. Part 1: general discussion and the case of small conductivity, *J. Fluid Mech.*, **5(1)**, 113–133.

Bebieva, Y., and M.-L. Timmermans (2016), An examination of double-diffusive processes in a mesoscale eddy in the Arctic Ocean, *J. Geophys. Res. Oceans*, **121**, 457–475.

D'Asaro, E. A. (1989), The decay of wind-forced mixed layer inertial oscillations due to the β effect, J. Geophys. Res., **94(C2)**, 2045–2056.

D'Asaro, E. A., and M. Morehead (1991), Internal waves and velocity fine structure in the Arctic Ocean, *J. Geophys. Res.*, ***96*****(C7)**, 12,725-712,738.

D'Asaro, E. A., and J. H. Morison (1992), Internal waves and mixing in the Arctic Ocean, *Deep Sea Research*, ***39***(Suppl. 2), S459-S484.

Davis, P. E., C. Lique, H. L. Johnson and J. D. Guthrie (2016), Competing effects of elevated vertical mixing and increased freshwater input on the stratification and sea ice cover in a changing Arctic Ocean. *Journal of Physical Oceanography*, ***46*****(5)**, 1531-1553.

Deming, W.E. (1943), Statistical adjustment of data, John Wiley & Sons, New York, NY.

Desaubies, Y. J. F. (1976), Analytical Representation of Internal Wave Spectra, *Journal of Physical Oceanography*, ***6*****(6)**, 976-981.

Dillon, T. M., and D. R. Caldwell (1980), The Batchelor spectrum and dissipation in the upper ocean, *J. Geophys. Res. Oceans, **85*****(C4)**, 1910-1916.

Dosser, H. V., and L. Rainville (2015), Dynamics of the changing near-inertial internal wave field in the Arctic Ocean, *Journal of Physical Oceanography*, **46:2**, 395-415.

Efron, B., and G. Gong (1983), A leisurely look at the bootstrap, the jackknife, and cross-validation, *The American Statistician*, ***37*(1)**, 36-48.

Fer, I. (2009), Weak vertical diffusion allows maintenance of cold halocline in the central Arctic, *Atmos. Ocean. Sci. Lett*, ***2*(3)**, 148-152.

Fer, I. (2014), Near-inertial mixing in the central Arctic Ocean. *Journal of Physical Oceanography*, ***44*(8)**, 2031-2049.

Fer, I., and A. Sundfjord (2007), Observations of upper ocean boundary layer dynamics in the marginal ice zone, *Journal of Geophysical Research: Oceans*, ***112*(C4)**.

Flanagan, J. D., A. S. Lefler, and T. Radko (2013), Heat transport through diffusive interfaces, *Geophys. Res. Lett.*, **40**, 2466–2470.

Flanagan, J.D., T. Radko, W. J. Shaw, and T. P. Stanton (2014), Dynamic and Double-Diffusive Instabilities in a Weak Pycnocline. Part II: Direct Numerical Simulations and Flux Laws, *J. Phys. Oceanogr.*, **44**, 1992–2012.

Fofonoff, N. P. (1985), Physical properties of seawater: A new salinity scale and equation of state for seawater, *Journal of Geophysical Research*, ***90***, 3332-3342.

Garrett, C. J., and W. H. Munk (1972), Space-time scales of internal waves, *Geophys. Fluid Dyn*, ***2***, 225-264.

Garrett, C. J., and W. H. Munk (1975), Space-time scales of internal waves: A progress report, *Journal of Geophysical Research*, ***80***, 291-297.

Gill, A. E. (1984). On the behavior of internal waves in the wakes of storms. *Journal of Physical Oceanography*, ***14*(7)**, 1129-1151.

Gonella, J. (1972), A rotary-component method for analyzing meteorological and oceanographic vector time series, *Deep Sea Res.*, ***19***, 833-846.

Gregg, M. C. (1987), Diapycnal mixing in the thermocline: A review, *J. Geophys. Res.*, **92(C5)**, 5249–5286.

Gregg, M. C. (1989), Scaling turbulent dissipation in the thermocline, *Journal of Geophysical Research*, ***94*****(C7)**, 9686-9698.

Gregg, M. C., and T. B. Meagher (1980), The dynamic response of glass rod thermistors, *J. Geophys. Res.*, **85(C5)**, 2779–2786.

Gregg, M. C. and T. B. Sanford (1987), Shear and turbulence in thermohaline staircases, *Deep Sea Research Part A. Oceanographic Research Papers*, **34(10)**, 1689-1696.

Gregg, M. C., and T. B. Sanford (1988), The dependence of turbulent dissipation on stratification in a diffusively stable thermocline, *Journal of Geophysical Research: Oceans*, ***93*****(C10)**, 12381-12392.

Gregg, M. C., T. B. Sanford, and D. P. Winkel (2003), Reduced mixing from the breaking of internal waves in equatorial waters, *Nature*, ***422***, 513-515.

Guthrie, J. D., J. H. Morison, and I. Fer (2013), Revisiting internal waves and mixing in the Arctic Ocean, *J. Geophys. Res. Oceans*, **118**, 3966–3977.

Guthrie, J. D., I. Fer, and J. Morison (2015), Observational validation of the diffusive convection flux laws in the Amundsen Basin, Arctic Ocean, *J. Geophys. Res. Oceans*, **120**, 7880–7896.

Halle, C., and R. Pinkel (2003), Internal wave variability in the Beaufort Sea during the winter of 1993/1994, *Journal of Geophysical Research-Oceans*, ***108*****(C7)**.

Kelley, D. E. (1990), Fluxes through diffusive staircases: A new formulation, *J. Geophys. Res.*, **95(C3)**, 3365–3371.

Kelley, D.E., H.J.S. Fernando, A.E. Gargett, J. Tanny, and E. Özsoy (2003), The diffusive regime of double-diffusive convection, *Progress in Oceanography*, **56(3-4)**, 461-481.

Kendall, M. G. (1938), A new measure of rank correlation, *Biometrika*, **30**, 81–93.

Kerr, R.M., (1996), Rayleigh number scaling in numerical convection, *Journal of Fluid Mechanics*, **310**, 139-179.

Kraichnan, R.H., (1968), Small-Scale Structure of a Scalar Field Convected by Turbulence, *Physics of Fluids*, **11**, 945-953.

Kunze, E., E. Firing, J. M. Hummon, T. K. Chereskin, and A. M. Thurnherr (2006), Global abyssal mixing inferred from lowered ADCP shear and CTD strain profiles, *J. Phys Ocean.*, ***36*(12)**, 2350-2352.

Kwok, R., G. F. Cunningham, M. Wesnahan, I. Rigor, H. J. Swally, and D. Yi (2009), Thinning and volume loss of the Arctic Ocean sea ice cover: 2003-2008, *Journal of Geophysical Research*, ***114***, C07005.

Kwok, R., and N. Untersteiner (2011), The thinning of Arctic sea ice, *Phys. Today*, ***64*(4)**, 36-41.

Large, W. G., J. C. McWilliams, and S. C. Doney (1994), Oceanic Vertical Mixing - a Review and a Model with a Nonlocal Boundary-Layer Parameterization, *Reviews of Geophysics*, ***32*(4)**, 363-403.

Leaman, K. D., and T. B. Sanford (1975), Vertical energy propagation of inertial waves: a vector spectral analysis of velocity profiles, *J. Geophys. Res.*, ***80*(15)**, 1975-1978.

Lee, C. M., E. Kunze, T. B. Sanford, J. D. Nash, M. A. Merrifield, and P. E. Holloway (2006), :Internal tides and turbulence along the 3000-m isobath of the Hawaiian Ridge, *Journal of Physical Oceanography*, ***36***, 1165-1183.

Lenn, Y. D., P. J. Wiles, S. Torres-Valdes, E. P. Abrahamsen, T. P. Rippeth, J. H. Simpson, ... S. Kirillov (2009), Vertical mixing at intermediate depths in the Arctic boundary current, *Geophys. Res. Lett.*, ***36***, L05601.

Levine, M. D., C. A. Paulson, and J. H. Morison (1985), Internal Waves in the Arctic Ocean - Comparison with Lower-Latitude Observations, *Journal of Physical Oceanography*, ***15*****(6)**, 800-809.

Levine, M. D., C. A. Paulson, and J. H. Morison (1987), Observations of Internal Gravity-Waves under the Arctic Pack Ice, *Journal of Geophysical Research-Oceans*, ***92*****(C1)**, 779-782.

Lique, C., J. D. Guthrie, M. Steele, A. Proshutinsky, J. H. Morison, and R. Krishfield (2014), Diffusive vertical heat flux in the Canada Basin of the Arctic Ocean inferred from moored instruments. *Journal of Geophysical Research: Oceans*, ***119*****(1)**, 496-508.

Long, C. E. (1981), A simple model for time-dependent stably stratifioed turbulent boundary layers, University of Washington, Seattle.

Maykut, G. A., and N. Untersteiner (1971), Some results from a time-dependent thermodynamic model of sea ice, *Journal of Geophysical Research*, ***76*****(6)**, 1550-1575.

McPhee, M. G. (2008), *Air-Ice-Ocean Interaction: Turbulent Ocean Boundary Layer Exchange Processes*, Springer, 157-160.

McPhee, M. G., and L. H. Kantha (1989), Generation of internal waves by sea ice. *Journal of Geophysical Research*, ***94*****(C3)**, 3287-3302.

McPhee, M. G., A. Proshutinsky, J. Morison, M. Steele, and M. Alkire (2009), Rapid change in freshwater content of the Arctic Ocean, *Geophysical Research Letters*, ***36*****(10)**.

Merrifield, M., and R. Pinkel (1996), Inertial currents in the Beaufort Sea: Observations of response to wind and shear, *J. Geophys. Res., **101*****(C3)**, 6577-6590.

Merrifield, S. T., L. St. Laurent, B. Owens, A. M. Thurnherr, and J. M. Toole (2016), Enhanced Diapycnal Diffusivity in Intrusive Regions of the Drake Passage, *J. Phys. Oceanogr.*, **46(4)**, 1309-1321.

Morison, J., C. E. Long, and M. D. Levine (1985), The dissipation of internal wave energy under arctic ice, *Journal of Geophysical Research*, ***90*(C6)**, 11,959-911,966.

Morison, J., R. Kwok, C. Peralta-Ferriz, M. Alkire, I. Rigor, R. Andersen, and M. Steele (2012), Changing Arctic Ocean freshwater pathways, *Nature*, ***481*(7379)**, 66-70.

Morison, J., R. Andersen, R. Kwok, W.M. Smethie, I. G. Rigor, M. B. Alkire, … M. Steele (2014), The Transpolar Drift in the Central Arctic Ocean as measured by AON observations, Poster presented at the AGU Fall Meeting in San Francisco, CA.

Munk, W. (1966), Abyssal Recipes, *Deep-Sea Res. II*, ***13***, 707-730.

Munk, W., and C. Wunsch (1998), Abyssal recipes. II. Energetics of tidal and wind mixing, *Deep-Sea Research, Part I*, ***45*(12)**, 1977-2010.

Nagai, T., R. Inoue, A. Tandon, and H. Yamazaki (2015), Evidence of enhanced double-diffusive convection below the main stream of the Kuroshio Extension, *J. Geophys. Res. Oceans*, **120**, 8402–8421.

Nash, J. D., M. H. Alford, E. Kunze, K. Martini, and S. Kelly (2007), Hotspots of deep ocean mixing on the Oregon continental slope, *Geophysical Research Letters*, **34**.

Neshyba, S., V. T. Neal, and W. Denner (1971), Temperature and conductivity measurements under Ice Island T-3, *J. Geophys. Res.*, **76(33)**, 8107–8120.

Niemela, J. J., L. Skrbek, K. R. Sreenivasan, and R. J. Donnelly (2000), Turbulent convection at very high Rayleigh numbers, *Nature*, **404**, 837– 840.

Olbers, D. J. (1983), Models of the oceanic internal wave fields, *Reviews in Geophysics*, ***21*****(7)**, 1567-1606.

Osborn, T. R. (1980), Estimates of the local rate of diffusion from dissipation measurements, *J. Phys. Oceanogr.*, ***10***, 83-89.

Osborn, T.R., and C.S. Cox (1972), Oceanic fine structure, *Geophys. Fluid Dyn.*, ***3***, 321-345.

Padman, L. (1994), Momentum fluxes through sheared oceanic thermohaline steps, *J. Geophys. Res.*, **99(C11)**, 22491–22499.

Padman, L., and T. M. Dillon (1987), Vertical heat fluxes through the Beaufort Sea thermohaline staircase, *J. Geophys. Res.*, **92(C10)**, 10799–10806.

Padman, L., and T. M. Dillon (1991), Turbulent mixing near the Yermak Plateau during the Coordinated Eastern Arctic Experiment, , *J. Geophys. Res.*, ***96***, 4769-4782. .

Padman, L., M. Levine, T. Dillon, J. Morison, and R. Pinkel (1990), Hydrography and microstructure of an Arctic cyclonic eddy, *Journal of Geophysical Research: Oceans*, ***95*****(C6)**, 9411-9420.

Peralta-Ferriz, C. and R. A. Woodgate (2015), Seasonal and interannual variability of pan-Arctic surface mixed layer properties from 1979 to 2012 from hydrographic data, and the dominance of stratification for multiyear mixed layer depth shoaling, *Progress in Oceanography*, ISSN 0079-6611.

Perlin, A., J. N. Moum, J. M. Klymak, M. D. Levine, T. Boyd, and P. M. Kosro (2005), A modified law-of-the-wall applied to oceanic bottom boundary layers, *Journal of Geophysical Research: Oceans*, ***110*****(C10)**.

Peterson, A.K. and I. Fer (2014), Dissipation measurements using temperature microstructure from an underwater glider, *Methods in Oceanography*, **10**, September 2014, Pages 44-69, ISSN 2211-1220.

Pinkel, R. (2005), Near-inertial wave propagation in the western Arctic, *Journal of Physical Oceanography*, ***35*(5)**, 645-665.

Plueddemann, A. J., R. Krishfield, T. Takizawa, K. Hatakeyama, and S. Honjo (1998), Upper ocean velocities in the Beaufort Gyre, *Geophysical Research Letters*, ***25*(2)**, 183-186.

Polyakov, I. V., J. E. Walsh, and R. Kwok (2011), Recent Changes of Arctic Multiyear Sea Ice Coverage and the Likely Causes, *Bulletin of the American Meteorological Society*, ***93*(2)**, 145-151.

Polyakov, I.V., A. V. Pnyushkov, R. Rember, V. V. Ivanov, Y.-D. Lenn, L. Padman, and E. C. Carmack (2012), Mooring-Based Observations of Double-Diffusive Staircases over the Laptev Sea Slope. *J. Phys. Oceanogr.*, **42**, 95–109.

Polzin, K. L., J. M. Toole, and R. W. Schmitt (1995), Finescale parameterizations of turbulent dissipation, *J. Phys. Oceanogr.*, ***25***, 306-328.

Proshutinsky, A., R. Krishfield, M. L. Timmermans, J. Toole, E. Carmack, F. McLaughlin, W. J. Williams, S. Zimmermann, M. Itoh, and K. Shimada (2009), Beaufort Gyre freshwater reservoir: State and variability from observations, *Journal of Geophysical Research-Oceans*, ***114***.

Radko, T., A. Bulters, J. D. Flanagan, and J. M. Campin (2014). Double-diffusive recipes. Part I: Large-scale dynamics of thermohaline staircases. *J. Phys. Oceanogr.*, ***44*(5),** 1269-1284.

Radko, T., J. Ball, J. Colosi, and J. Flanagan (2015), Double-Diffusive Convection in a Stochastic Shear. *J. Phys. Oceanogr.*, ***45*(12)**, 3155-3167.

Rainville, L., and P. Winsor (2008), Mixing across the Arctic Ocean: Microstructure observations during the Beringia 2005 Expedition, *Geophys. Res. Lett.*, ***35*****(8)**, L08606.

Rainville, L., and R. A. Woodgate (2009), Observations of internal wave generation in the seasonally ice-free Arctic, *Geophysical Research Letters*, ***36.***

Rothrock, D. A., D. B. Percival, and M. Wensnahan (2008), The decline in arctic sea-ice thickness: Separating the spatial, annual, and interannual variability in a quarter century of submarine data, *Journal of Geophysical Research-Oceans*, ***113*****(C5)**.

Ruddick, B., A. Anis, and K. Thompson (2000), Maximum Likelihood Spectral Fitting: The Batchelor Spectrum. *J. Atmos. Oceanic Technol.*, **17**, 1541–1555.

Rudels, B., E.P. Jones, U. Schauer and P. Eriksson (2004), Atlantic sources of the Arctic Ocean surface and halocline waters. *Polar Res.,* **23(2)**, 181-208.

Sánchez, X., and E. Roget (2007), Microstructure measurements and heat flux calculations of a triple-diffusive process in a lake within the diffusive layer convection regime, *J. Geophys. Res.*, **112**, C02012.

Schauer, U., B.-M. A., W. Walczowski, E. Fahrbach, J. Piechura and E. Hansen (2008), Variations of measured heat flow through the Fram Strait between 1997 and 2006. p. 65-85. In R. R. Dickson, J. Meincke and P. Rhines [eds.], Arctic-Subarctic Ocean Fluxes: Defining the Role of the Northern Seas in Climate. Springer Science.

Scheifele, B., R. Pawlowicz, T. Sommer, and A. Wüest (2014), Double Diffusion in Saline Powell Lake, British Columbia. *Journal of Physical Oceanography*, ***44*****(11)**, 2893-2908.

Simmons, H. L., R. W. Hallberg, and B. K. Arbic (2004), Internal wave generation in a global baroclinic tide model, *Deep-Sea Res. II*, ***51***, 3043-3068.

Sirevaag, A., and I. Fer (2012), Vertical heat transfer in the Arctic Ocean: The role of double-diffusive mixing, *Journal of Geophysical Research: Oceans*, ***117*****(C7)**.

Sommer, T., J. R. Carpenter, M. Schmid, R. G. Lueck, M. Schurter, and A. Wüest (2013), Interface structure and flux laws in a natural double-diffusive layering, *J. Geophys. Res. Oceans*, **118**, 6092–6106.

Sommer, T., J. R. Carpenter, M. Schmid, R. G. Lueck, and A. Wüest (2013), Revisiting Microstructure Sensor Responses with Implications for Double-Diffusive Fluxes. *J. Atmos. Oceanic Technol.*, **30**, 1907–1923.

Sommer, T., J. R. Carpenter, and A. Wüest (2014), Double-diffusive interfaces in Lake Kivu reproduced by direct numerical simulations, *Geophys. Res. Lett.*, **41**, 5114–5121.

St. Laurent, L. C., H. L. Simmons, and S. R. Jayne (2002,), Estimating tidally driven mixing in the deep ocean, *Geophys. Res. Lett., **29*****(23)**, 2106.

Steele, M., and T. Boyd (1998), Retreat of the cold halocline layer in the Arctic Ocean, *Journal of Geophysical Research-Oceans*, ***103*****(C5)**, 10419-10435.

Steele, M., R. Morley, and W. Ermold (2001), PHC: A global ocean hydrography with a high-quality Arctic Ocean, *Journal of Climate*, ***14*****(9)**, 2079-2087.

Stillinger, D. C., K. N. Helland, and C. W. V. Atta (1983), Experiments on the transition of homogeneous turbulence to internal waves in a stratified fluid, *Journal of Fluid Mechanics,*, ***131***, 91-122.

Stroeve, J., M. M. Holland, W. Meier, T. Scambos, and M. Serreze (2007), Arctic sea ice decline: Faster than forecast, *Geophysical Research Letters*, ***34*****(9)**.

Taylor, J. (1988), The fluxes across a diffusive interface at low values of the density ratio. *Deep Sea Research Part A. Oceanographic Research Papers*, **35(4)**, 555-567.

Thompson, D. W. J., and J. M. Wallace (1998), The Arctic Oscillation signature in the wintertime geopotential height and temperature fields, *Geophysical Research Letters*, ***25*****(9)**, 1297-1300.

Timmermans, M. L., J. Toole, R. Krishfield, and P. Winsor (2008), Ice-Tethered Profiler observations of the double-diffusive staircase in the Canada Basin thermocline, *Journal of Geophysical Research-Oceans*, ***113***.

Turner, J. S. (1965). The coupled turbulent transports of salt and heat across a sharp density interface. *Int. J. Heat and Mass Transport*, **8**, 759-767.

Vivier, F., J. K. Hutchings, Y. Kawaguchi, T. Kikuchi, J. H. Morison, A. Lourenço, and T. Noguchi (2016), Sea ice melt onset associated with lead opening during the spring/summer transition near the North Pole, *J. Geophys. Res. Oceans*, **121**.

Worster, M.G. (2004). Time-dependent fluxes across double-diffusive interfaces. *Journal of Fluid Mechanics*, **505**, 287-307.

Zhang, J. L., and M. Steele (2007), Effect of vertical mixing on the Atlantic Water layer circulation in the Arctic Ocean, *Journal of Geophysical Research-Oceans*, ***112*****(C4)**.